Year : 2022

Radiological characterisation of materials from accelerators

Bonvin Valentin

UNIL | Université de Lausanne

Faculté de biologie et de médecine

Lausanne University Hospital
Institute of Radiation Physics (IRA)

Radiological characterisation of materials from accelerators

Thèse de doctorat ès sciences de la vie (PhD)

présentée à la

Faculté de biologie et de médecine
de l'Université de Lausanne

par

Valentin BONVIN

Master Ingénierie de la Santé et du Médicament, spécialité Radioprotection
Université de Grenoble

Jury

Prof. Claudio Sartori, Président
Prof. François Bochud, Directeur de thèse
Dr. Reiner Geyer, Co-directeur de thèse
Prof. Dr. Saverio Braccini, Expert
Prof. Dr. Andreas Pautz, Expert

Lausanne
(2022)

UNIL | Université de Lausanne

Faculté de biologie
et de médecine

**Lausanne University Hospital
Institute of Radiation Physics (IRA)**

Radiological characterisation of materials from accelerators

Thèse de doctorat ès sciences de la vie (PhD)

présentée à la

Faculté de biologie et de médecine
de l'Université de Lausanne

par

Valentin BONVIN

Master Ingénierie de la Santé et du Médicament, spécialité Radioprotection
Université de Grenoble

Jury

Prof. Claudio Sartori, Président
Prof. François Bochud, Directeur de thèse
Dr. Reiner Geyer, Co-directeur de thèse
Prof. Dr. Saverio Braccini, Expert
Prof. Dr. Andreas Pautz, Expert

Lausanne
(2022)

Imprimatur

Vu le rapport présenté par le jury d'examen, composé de

Président·e	Monsieur	Prof.	Claudio	**Sartori**
Directeur·trice de thèse	Monsieur	Prof.	François	**Bochud**
Co-directeur·trice	Monsieur	Dr	Reiner	**Geyer**
Expert·e·s	Monsieur	Prof.	Saverio	**Braccini**
	Monsieur	Prof.	Andreas	**Pautz**

le Conseil de Faculté autorise l'impression de la thèse de

Monsieur Valentin Eloi André Bonvin

Master 2 Radioprotection, Université Grenoble Alpes, France

intitulée

Radiological characterisation
of materials from accelerators

Lausanne, le 25 janvier 2022

pour le Doyen
de la Faculté de biologie et de médecine

Prof. Claudio Sartori

Remerciements

Ce travail de doctorat a été effectué au sein d'une collaboration entre l'Organisation européenne pour la recherche nucléaire (CERN) et l'institut de radio physique (IRA) de Lausanne. De plus, mon travail s'est focalisé sur la caractérisation du cyclotron des Hôpitaux Universitaires de Genève (HUG), c'est pourquoi je souhaiterais remercier toutes les personnes qui ont contribué de près ou de loin à ce projet que ce soit au CERN, à l'IRA ou aux HUG.

Je voudrais remercier plus particulièrement quelques personnes qui ont été directement impliquées dans ce projet.

Merci à mon directeur de thèse, le Pr. François Bochud, qui a toujours été là pour écouter, suivre et diriger le travail. Il a su m'apporter de très bons conseils tout au long de ce doctorat. Merci François.

Un grand merci à mon co-directeur de thèse, le Dr. Reiner Geyer qui m'a suivi tout au long de ce projet depuis mon stage de fin de master. Il a toujours été disponible, de très bons conseils et a su m'aider dans les moments difficiles. Les nombreux échanges que nous avons eu durant ces quelques années et plus particulièrement durant la période COVID ont été à la fois enrichissants mais aussi indispensables pour mener à bien le projet. Encore une fois merci pour tout.

Merci au Dr. Jérôme Damet de m'avoir accueilli à l'IRA au sein du groupe de radioprotection dès mon stage de fin de master. Ce fut un plaisir de rejoindre ce groupe où le travail et la bonne humeur sont au rendez-vous. Merci d'avoir toujours suivi le travail de près et merci pour tes nombreux conseils.

Merci au Dr. Helmut Vincke, mon superviseur CERN, et le Dr. Chris Theis pour leur accueil au sein du groupe de radioprotection au CERN. Merci également pour l'aide et les conseils lors de l'utilisation des outils de caractérisation (FLUKA, ActiWiz).

Merci à Florian Degueldre pour les réponses à mes nombreuses questions et demandes concernant le cyclotron. Merci de m'avoir fourni tous les documents nécessaires à la réussite du projet.

Merci à Jean-Michel Geets, de l'entreprise IBA, pour toutes les informations et les dessins techniques du cyclotron. Ils ont été d'une grande utilité lors de l'implémentation du modèle de simulation.

Je voudrais remercier Laurent, Camille, Andreas, Nicolas et Fréderic pour leur aide et leur bonne humeur. Sans oublier les doctorants avec qui j'ai pu partager de sympathiques moments. Merci à vous Siria, Marie, Josh, Patrick, Damien, Anaïs, Alexandre et Flore.

Je remercie ma famille de m'avoir toujours encouragé et soutenu dans ce projet.

Pour finir je souhaiterais remercier ma compagne, Alexandra, pour le soutien et l'aide qu'elle a su m'apporter tout au long de ce doctorat. Merci encore.

Abstract

Materials inside and around accelerators can get activated by the irradiation fields caused by the primary beam particles and their interactions with matter. This is the case for accelerators from both fields, fundamental research and medical applications. The activation of materials poses a radiological risk for people who work near the facilities and for the waste management during the dismantling phase. The materials at the accelerators must therefore be radiologically characterized. The radiological characterisation represents the determination of the location and concentration of the artificially produced radionuclides inside the different components.

The European Organization for Nuclear Research (CERN) has the largest accelerator complex in the world with a total network of almost 50km. Therefore, CERN has implemented some efficient methods for the characterisation of materials leaving irradiation zones. They are based on both, Monte-Carlo simulations and analytical calculations.

The aim of this work was to transfer and evaluate some of them in a medical environment. They were applied for the characterisation of materials from a PET-cyclotron facility, which is used for the production of radiopharmaceuticals within the University Hospitals of Geneva (HUG).

In a first step of this work, the mechanisms for the creation of the irradiation fields caused by the primary beam particles and their interactions with matter had to be analysed for this cyclotron and implemented in a Monte Carlo simulation. Based on these irradiation fields of secondary particles, the activities of radio nuclides could be calculated analytically using ActiWiz, a software tool recently developed by CERN.

In a first example, our model was applied to the magnetic coils of the cyclotron. The aim was to determine the three-dimensional distribution of activation products inside these components after 15 years of operation. The results were compared with measurements for validation.
In a second exercise, the same model was extended to materials situated inside the bunker. Again, for validation, the simulation results were compared to measurement results by using activated samples.

We have shown that these methods and tools can be applied for the characterisation of materials from accelerators used in the medical field. Despite the limited precision, clear conclusions concerning the management of radioactive waste and the associated risks could be formulated for the radiation protection expert. Detailed studies about the limitations of the approach were performed and were presented.

Résumé

L'interaction du faisceau de particules primaires avec la matière environnante peut causer l'activation des matériaux composant les accélérateurs de particules et leurs environnements. Ce phénomène d'activation a lieu dans les accélérateurs quels que soient leurs domaines d'applications, comme par exemple, la recherche fondamentale ou les applications médicales. L'activation de la matière engendre un risque radiologique pour les personnes travaillant à proximité de ces installations et complexifie la gestion de déchets rendus radioactifs lors d'une phase de démantèlement. Afin de pouvoir protéger les travailleurs étant au contact de matériaux activés, l'estimation du risque radiologique est essentielle. Pour ce faire, les matériaux potentiellement activés provenant des accélérateurs et leurs environnements doivent être caractérisés radiologiquement. La caractérisation radiologique représente la détermination de la localisation et de la concentration des radionucléides produits artificiellement à l'intérieur des différents composants.

L'Organisation européenne pour la recherche nucléaire (CERN) possède le plus grand complexe d'accélérateurs au monde, avec un réseau total de près de 50 km. Par conséquent, le CERN a développé des méthodes efficaces pour la caractérisation des matériaux sortant des zones d'irradiation. Ces méthodes sont basées à la fois sur l'utilisation d'outil de simulations Monte-Carlo pour le calcul de champs de radiation de particules et d'outil permettant la réalisation de calculs des activités à partir des champs de radiation.

Le but de ce travail a été de transférer et d'évaluer ces outils et méthodes dans un environnement médical. Ils ont été appliqués au sein des Hôpitaux Universitaires de Genève (HUG) pour la caractérisation des matériaux de leur cyclotron utilisé pour la production de radio pharmaceutiques.

Durant la première partie de ce travail, les mécanismes de création des champs de radiation secondaires causés par l'interaction du faisceau et leurs interactions avec la matière étant responsables de l'activation ont été étudiés en détail et implémentés dans une simulation Monte Carlo. Sur la base de ces champs d'irradiation de particules secondaires calculés, les activités des radionucléides ont pu être calculées analytiquement à l'aide d'ActiWiz, un outil logiciel récemment développé par le CERN.

Par la suite, nous avons appliqué ce modèle pour la caractérisation des bobines du cyclotron dans l'objectif de déterminer la distribution tridimensionnelle des produits d'activation et de leurs activités après 15 ans d'utilisation. Les résultats de simulations ont été comparés à des mesures expérimentales pour validation. Dans un second temps, ce même modèle a été étendu pour la caractérisation de matériaux situés à l'extérieur de la machine, tout autour de son bunker. Dans le but de valider nos expériences, les résultats de simulation ont été comparés aux résultats expérimentaux en utilisant des échantillons activés.

Ce travail a permis de montrer que ces méthodes et outils peuvent être appliqués pour la caractérisation de matériaux issus d'accélérateurs utilisés dans le domaine médical. Malgré une précision limitée, des conclusions claires concernant la gestion des déchets radioactifs et les risques associés ont pu être formulés pour l'expert en radioprotection. Des études détaillées sur les limites de l'approche ont été réalisées et sont présentées dans cette thèse.

Table of contents

1 Introduction

This PhD project took place within the framework of a collaboration between the Radiation Protection Group of the HSE Unit (HSE-RP) at the European Laboratory for Particle Physics (CERN) and the Institute of Radiation Physics (IRA) at the Lausanne University Hospital (CHUV). The Radiation Protection Group at CERN ensures Host State compliance of the accelerator laboratory with radiation protection legislation. The host states are both Switzerland and France. The main objective of the collaboration between CERN and IRA was to develop new techniques for characterizing potentially radioactive materials in the environment of accelerators. I was enrolled in the CERN Doctoral Student Program. The project was funded by CERN-HSE-RP.

At CERN, accelerators are mainly used for research conducted at the forefront of fundamental particle physics. Experiments profit here from the highest beam energies, which can be delivered nowadays by human build machines. The energies exceed the one TeV scale. In the medical environment instead, accelerators find mainly their applications in radionuclide production and radiation therapy. The required beam energies are here in the range between one MeV and one GeV. Although the energies used for the research in particle physics are much higher and the objectives are different, CERN has contributed to the domain of medical accelerators by its technology and know-how. Recent prominent examples are MedAustron [1] and ADAM [2]. Both accelerator concepts for hadron therapy are based on developments and design studies, which were originally led by CERN. With Medicis [3], CERN contributes to the research on the production of radionuclides and their application in medicine.

Beside the knowledge transfer related to accelerator technologies, also techniques relevant for operational radiation protection have been developed at CERN. During my stay at CERN, I had the opportunity to learn about the tools and methods applied for the radiological characterisation of potentially radioactive material from radiation zones and to transfer them to the environment of a Positron Emission Tomography-cyclotron (PET-cyclotron), which is used for producing radiopharmaceuticals at the University Hospital of Geneva (HUG). In the following, I will give a short introduction to the accelerator complex at CERN and an overview of the usage of accelerators in medicine. This will be followed by the outline of my thesis.

1.1 The accelerator complex at CERN

CERN is the largest laboratory worldwide for particle physics research. The complex of accelerators, which is shown Figure 1, produces primary particle beams of protons, antiprotons, heavy ions, electrons and positrons with an energy range between 100 keV for antiprotons from the Extra Low Energy Antiproton ring (ELENA) and up to several TeV for protons from the Large Hadron Collider (LHC).

Presently, the most prominent project at CERN is the LHC with two proton beams with an energy of 6.5 TeV. The LHC consists of a 27-kilometer ring of superconducting magnets with several accelerating structures to boost the energy of the particles along the way. The beams inside the LHC are made to collide at four locations around the accelerator ring, corresponding to the positions of the experiments ATLAS, CMS, ALICE and LHC-b. The main objective of the LHC experiments is to test the "standard model" of particle physics and to search for phenomena beyond. Most of the other machines at CERN are used as pre-accelerators for the LHC. Additionally, the proton synchrotron (PS) and the super proton synchrotron (SPS) have their own experimental halls where beams are used for experiments at lower energies.

The accelerator complex at CERN provides unique opportunities in experimental particle physics research. However, during the operation of these machines, primary and secondary particles interact with the materials inside and outside the accelerators. Consequently, all materials close to the particle beams can get irradiated and activated. For example, the LHC consists of 1232 dipole magnets with a length of 15 meters each and 392 quadrupoles magnets with lengths between 5-7 meters [4]. This corresponds to tens of thousands of tons of material. From a radiation protection point of view, two aspects have to be taken into account:

- The activation leads to residual dose rates, which requires dedicated measures during maintenance work.
- Any kind of material leaving the radiation zones might have become radioactive by activation. All materials must be radiologically characterised and treated as required by the rules of radiation protection.

The irradiation fields responsible for activating materials at CERN are complex and include a mixture of hadrons, photons and leptons. Energies around meV (thermal energies in the case of neutrons) up to TeV deliver significant contributions to the activation processes. Because of

this complexity, in most cases it is impossible to directly measure the radiation fields throughout CERN. The radiation protection group at CERN therefore applies a method which is based on a Monte Carlo simulation used for calculating radiation fields at any position near the accelerators, and an analytical code (ActiWiz). ActiWiz uses the simulated irradiation fields and calculates the activation products inside any arbitrary material. ActiWiz has been recently developed at CERN in order to simplify and speed up the characterisation process for material from irradiation zones compared to a pure Monte Carlo approach [5]. This method has been developed and is routinely used at CERN for the characterization of materials coming from these accelerators. This approach will be explained in more detail in Section 1.3 and will be transferred and applied in the context of this thesis for the materials being activated at a PET-cyclotron, which is used for the production of radio pharmaceuticals at HUG. At the PET-Cyclotron, the activation of material is dominated by secondary neutrons with energies between thermal up to a few MeV. Although the CERN accelerators operate at much higher energies, low energetic neutrons play an important role for the activation of material here as well [6]. The neutrons are produced during the thermalization process of hadronic showers within materials. The large cross-sections of low energetic neutrons with certain nuclides result in high production yields of radioactive isotopes. The activation processes via low energetic neutrons are similar and important for both, hadron accelerators at CERN and in medicine.
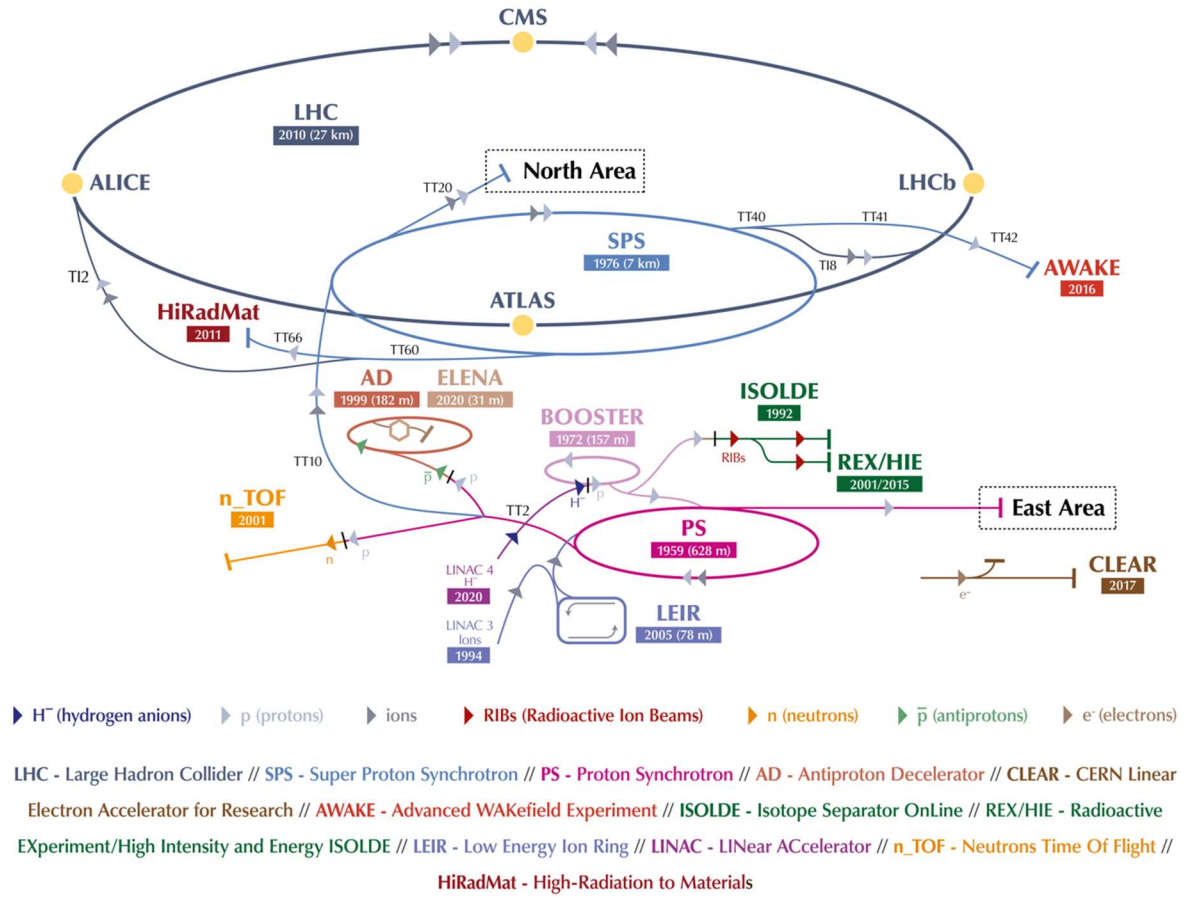
Figure 1. The CERN accelerator complex [7].

1.2 Historical overview of accelerators in medicine

For more than 100 years, discoveries and inventions in the field of the acceleration of particles have frequently resulted in new developments in medicine. One of the most prominent examples is the discovery of X-rays by Wilhelm Conrad Roentgen at the end of the 19th century. Just a few weeks later, X-rays were applied for medical imaging. Only one year later, they were used to successfully cure a skin tumour in a five-year-old girl [8].

In 1929, Ernest Orlando Lawrence invented the cyclotron in Berkeley [9]. The first cyclotron, which is shown in Figure 2, had a diameter of 4 inches (about 10 cm), and was able to accelerate protons up to 80 keV. A few years later, a 27-inch machine ($\approx$ 69 cm) was already delivering proton energies of 4.8 MeV. The invention of the cyclotron was a milestone for both nuclear physics and medicine. In 1936, the artificially produced phosphorus-32 nuclide was used to treat leukaemia [10]. Nowadays, artificially produced radionuclides are used for radio tracing in biology, diagnosis in medicine, brachytherapy or theranostic applications. The theranostic principle in nuclear medicine involves combining diagnostic imaging and therapy with the same molecule, which is radiolabeled differently, or administered in other dosages [11].

The first circular electron accelerator, named the betatron, was built in 1940 by Donald Kerst and Robert Seber. Originally designed for research in atomic physics in the United States, the betatron was soon adopted for clinical use. Its first clinical application was by Konrad Gund in 1942 in Germany during World War II [12].

In 1946, the physicist Dr. Robert Rathbun Wilson proposed the use of proton beams for treating cancer in a paper entitled "Radiological Use of Fast Protons". In 1954, the year when CERN was founded, protons from a cyclotron in Berkeley were used for the first time for the treatment of humans [8].
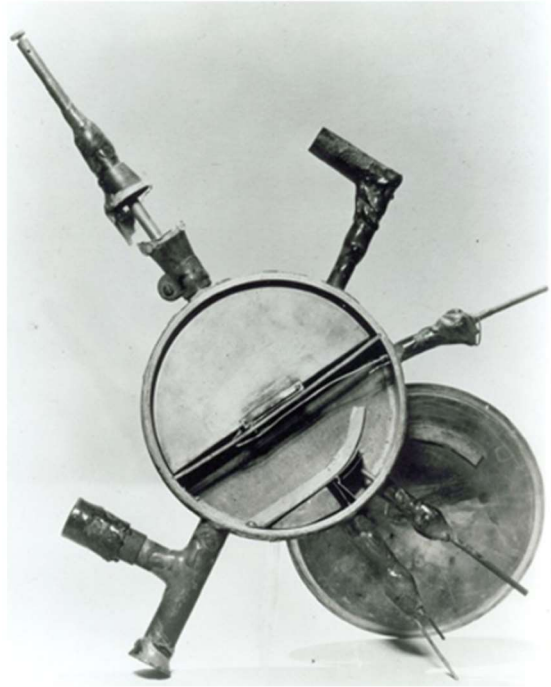
Figure 2. First 4" cyclotron developed by E. Lawrence in 1930 [13].

In 1952, the first electron linear accelerator (LINAC) for medical applications was installed in at the Hammersmith Hospital in London. The first patient was treated on 7 September 1953 [11]. Since then, LINACs have become the horsepower of radiotherapy worldwide and have progressively replaced betatrons and ^{60}Co sources [15]. As an illustrative example, in 2018, 744 LINACs were available in France for cancer treatments [16], while in comparison only four installations for proton therapy exist [17].

In terms of size, contemporary therapy centres for protons and heavy ions use much larger installations compared to the LINACs, since higher particle energies are required for the same penetration into the body. Nevertheless, more than 45 centres dedicated to delivering therapeutic beams of protons and carbon ions are currently in operation worldwide [8]. Some of them are still hosted in physics laboratories, but all the new centres have dedicated clinical facilities, often well integrated with close-by hospitals. Also decades after the initial discoveries and inventions in the field of accelerators in medicine, the field is still open for innovations and optimizations.

Although the energies of accelerators in medicine are much lower than those used at CERN, they pose the same radiological risks of emitting ionizing radiation:
- During operation because of the interaction of the beam particles with matter.

- After operation because of the activation of the accelerator's materials and its surroundings. The activations are caused by the primary and secondary particles emitted during the operation.

They fall within the legislation of radiation protection.

In the context of this thesis, the activation of some components of a modern PET-cyclotron and its surroundings has been reviewed in detail. The cyclotron under consideration is installed at the HUG and is used for producing radiopharmaceuticals. In the following, the installation will be described in detail.

1.3   The PET-Cyclotron at HUG

Radionuclides are widely used in nuclear medicine today. Fluorodeoxyglucose (FDG) with ^{18}F ($[^{18}$F]FDG), which is mainly used in PET for cancer diagnoses is a prominent example [18]. To a lesser extent, $[^{18}$F]FDG is also used for the diagnosis of cardiovascular and neurodegenerative diseases similar to $[^{13}$N]NH3. The proportion of use of the radiopharmaceuticals as well as the typical dose injected to the patients per examination at HUG are given in Table 1 for the year 2021. Due to its short half-life the use of $[^{13}$N]NH3 can only be achieved in hospitals where a cyclotron is available on site.

Table 1. Number of examinations using PET-radiopharmaceuticals produced by the cyclotron at the nuclear medicine service for the year 2021.

Radiopharmaceutical	Type of examination	Number of examinations	Mean dose per examination [MBq]
$[^{18}$F]FDG	Cancer diagnosis	1654 (63%)	270
	Cardiovascular disease	97 (4%)	
	Neurodegenerative disease	160 (6%)	
$[^{13}$N]NH3	Cardiovascular disease	709 (27%)	205
Total		2620 (100%)	

With the establishment of national cyclotron networks, the development of diagnostic procedures in nuclear medicine and the increasing demands for PET scans, the number of biomedical cyclotrons has increased substantially over the past two to three decades. Presently, about 1200 cyclotrons are operated worldwide [19].

The cyclotron under consideration in this work is a Cyclone® 18/9. It has been installed at HUG for the production of PET radioisotopes by the IBA company (Ion Beam Applications, SA, Belgium) in 2000. The cyclotron is a compact accelerator with a diameter of two meters. It is

located inside a bunker with two-meter shielding walls in order to protect people and the environment from ionizing radiation as shown in Figure 3. The main components of the cyclotron are the yoke, the magnet coils with poles, the vacuum chamber, the ion sources, and the dees for acceleration. The cyclotron delivers proton beams of 18 MeV with a maximum intensity of 150 μA or deuteron beams of 9 MeV per nucleon with a maximum intensity of 40 μA. The beams are directed after acceleration towards one (or two) of the eight different target ports, which are used to produce the different radioisotopes. A maximum of two ports can be operated at a time simultaneously. Target assemblies for the production of the different radionuclides are installed at each of these ports. The main characteristics of the accelerator are summarized in Table 2.

The typical irradiation time for a production run of ^{18}F at HUG is about two hours. After irradiation, the activated material is then extracted for the synthesis of radiopharmaceuticals from the target via capillaries to the synthesis module. The activities produced in one production cycle are of the order of 350 GBq of ^{18}F. The synthesis yield is about 50 to 60 %, which correspond to a final activity of about 200 GBq of [^{18}F]FDG at the end of synthesis. The typical irradiation times at HUG for a production run of ^{18}F, ^{13}N and ^{11}C, the applied beam currents and the achieved activities for each target are given in Table 3. The beam currents of accelerators, which are used for isotope production, are relatively high. As a side effect, the fluxes of secondary neutrons, which are produced by the interactions of the beam particles with the target and other materials, are also high. This again leads to the activation of materials inside the machine and its surroundings, as illustrated in the next chapter in more detail.

Figure 3. HUG cyclotron inside its bunker.

Table 2. Main characteristics of the Cyclone 18/9 Cyclotron used at HUG (IBA, 2009).

Energy [MeV]	proton	18
	deuteron	9
Intensity [µA]	proton	150 (9.36×10^{14} p/s)
	deuteron	40 (2.50×10^{14} d/s)
Particles sources	2 separate Penning Ion Gauge ion sources	
Number of target ports	8	
Simultaneous target beams (Dual beams)	2	
Mean field [T]	1.35	
Weight [kg]	25000	

Table 3. Characteristics of the different target ports of the cyclotron used at HUG.

Source	Isotope produced	Half Life [min]	Vacuum windows	Target window	Target material	Target body	Beam current [µA]	Typical production time [min]	Typical activity produced [GBq]
T1	^{18}F	109.7	12.5 μm Ti	50 μm Havar®	H$_2$^{18}O	Niobium	70	120	350
T2	^{18}F	109.7	12.5 μm Ti	50 μm Havar®	H$_2$^{18}O	Niobium	35	120	175
T3	Not used	-			-		-	-	-
T4	^{11}C	20.4	12.5 μm Ti	500 μm Al	N$_2$ gas at 20 bars	Al	20	30	45
T5	^{18}F	109.7	12.5 μm Ti	50 μm Havar®	H$_2$^{18}O	Niobium	35	120	175
T6	^{18}F	109.7	12.5 μm Ti	50 μm Havar®	H$_2$^{18}O	Niobium	35	120	175
T7	^{13}N	9.97	12.5 μm Ti	25 μm Havar®	H$_2$O	Niobium	16	17	15
T8	Not used	-			-		-	-	-

1.4 Mechanisms of activation at the PET-cyclotron facility

Nuclear reactions of particles with the nuclei of the chemical elements of a component may cause an initially non-radioactive component to become radioactive. This kind of mechanisms are used to produce radionuclides for radiopharmaceuticals like ^{18}F via the following nuclear reaction channel:

$$^{18}O(p, n)^{18}F \tag{1}$$

Unfortunately, the activation processes are not limited to isotopes that are useful for PET examinations. Similar reactions take place inside most materials of the components of the cyclotron and its environment. To calculate the activation, the chemical composition of the material and the isotopic composition of the element must be known.

Let us have a second look at the nuclear reaction shown in Equation (1). It is a proton-induced reaction where ^{18}F is produced. At the same time a neutron is emitted, which can have an energy well above 1 MeV. Contrary to protons, neutrons, which do not carry an electric charge, can travel large distances in dense matter. They may traverse tenths of centimetres of steel or concrete, for example. During their passage through matter, they undergo frequent elastic and inelastic interactions with other nuclides, until they are absorbed or just decay (still unlikely, a free neutron has a half-life of about 10 min). At each interaction point, they change their direction and lose energy in a process known as "thermalization". Neutrons contribute via nuclear reactions to the activation of the biggest part of the materials inside and around the cyclotron because of their large penetration within matter. A few examples for neutron-induced nuclear reactions are listed in Table 4 below. For each of these processes, the cross section is a measure of the probability of occurrence. The cross sections for the ^{59}Co(n, γ) ^{60}Co and ^{63}Cu$(n, \alpha)^{60}$Co as a function of the neutron energy are given, as an example, in Figure 4.

Table 4. Examples of neutron-induced nuclear reactions.

Nuclear reactions
^{63}Cu$(n, \gamma)^{64}$Cu
^{63}Cu$(n, \alpha)^{60}$Co
^{63}Cu$(n, p)^{63}$Ni
^{63}Cu$(n, 2n)^{64}$Cu
^{59}Co(n, γ) ^{60}Co
^{58}Ni$(n, np)^{57}$Co
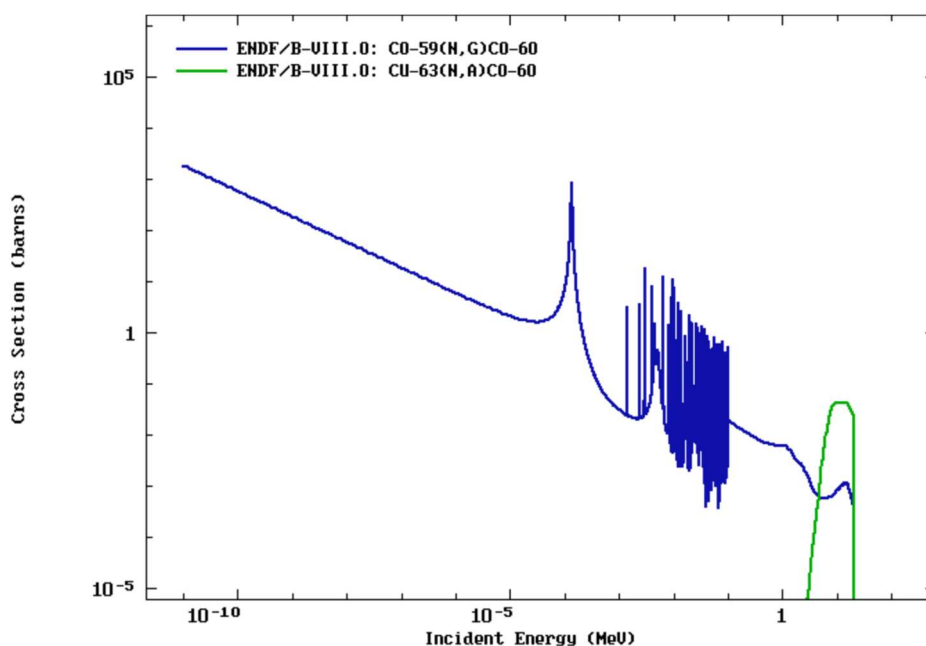
Figure 4. Cross section for ^{59}Co(n, γ) ^{60}Co (blue line) and ^{63}Cu$(n, \alpha)^{60}$Co (green line) nuclear reactions.

The 18 MeV protons produced by the cyclotron have a range of 2 mm and 4 mm in aluminium and water, respectively. The short range of these protons in matter is due to the low energies and the electromagnetic interactions, which protons underlie due to their positive charge. The full acceleration system of the cyclotron is hermetically surrounded by a vacuum chamber made from aluminium cylinder with a thickness of 25 mm in radial direction, which is closed by the main poles of the magnet towards the top and the bottom. Obviously, protons cannot traverse this barrier. But they can contribute to the activation of components of the accelerator, which are inside the vacuum chamber (including the chamber), within a penetration depth of a few mm or less. All other materials are exclusively activated by secondary neutrons, which originate from the interactions of the protons with matter inside the vacuum chamber.

The activity concentration inside a material increases with the time of irradiation until it reaches its equilibrium between production and decay, which is called 'saturation'. Not uncommonly, the produced isotopes may have long half-lives of months or even years. In such cases, the material accumulates activities over years and may need to eventually be declared as radioactive waste.

The task of modelling the activation of materials and components of the cyclotron facility requires a good description of the production of secondary neutrons inside the vacuum chamber followed by the transport calculations of the neutrons all over the installation taking into account nuclear interactions. As will be shown next, these calculations can be carried out using Monte Carlo simulations. Once the flux of neutrons at a given location is known for a material, its activation can be calculated analytically.

1.5 Calculation of the activation of materials at the facility

As mentioned just before, calculating the activation of a material at a given location **A** inside the machine or inside the bunker requires three elements:

1. Calculation of the production of secondary neutrons by the interaction of the beam particles with matter inside the vacuum chamber during acceleration.

2. Transport of each individual neutron within the cyclotron and the facility, followed by the scoring of the fluence at the location **A**.

3. Calculation of the activation products inside a material location **A**. For this step, the chemical composition of the material must be precisely known.

In the following three sections, my approach for these calculation steps will be explained in more detail.

1.5.1 Production of secondary neutrons by beam particles

The only way in which beam particles ("H⁻") produce neutrons is by their interaction with materials during the acceleration phase along their path from the ion source towards the stripper foils or during the extraction phase (now as protons) along their path from the stripper foils towards the production targets for radionuclides. H⁻ ions are delivered by the source for acceleration instead of positively charge protons because of two main advantages:

1. This enables the beam extraction process to be highly efficient by stripping off the two electrons within very thin carbon foils (stripping efficiency > 99.9%[20]).

2. The extraction of multiple beams is accomplished by inserting the extraction foil(s) so that they only intercept part of the beam, allowing the remainder to continue its acceleration to the next extraction foil.

After stripping, the now positively charged protons are bent by the magnetic field to head in the other direction and are guided towards the target assemblies. Inside the target assemblies the trajectories of the beam particles come to an end because either nuclear reactions take place, or the protons are stopped by electromagnetic interactions inside the target material. The number of protons arriving at the target assemblies is recorded by the accelerator's control system by the precise measurement of the delivered currents at each target port. As an example, the average current over one day and the average current over the year for the target T1 are shown in Figure 5, respectively in blue and red.
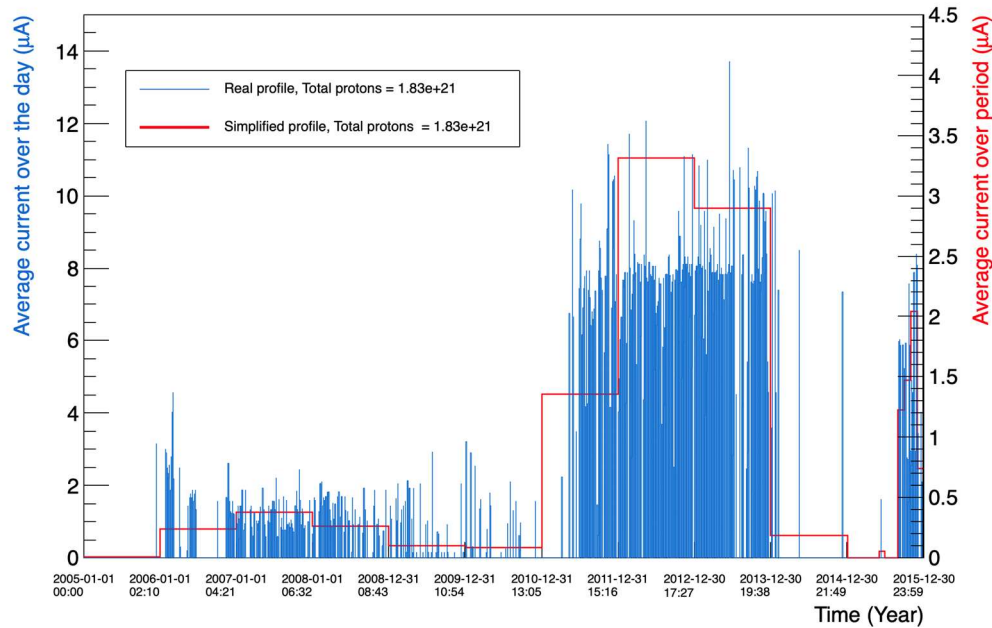
Figure 5. Beam currents on the target T1 during the last 10 years. Blue: mean current per day. Red: Simplified profile.

The activation mechanisms previously described have been classified into two separate mechanisms for calculating secondary neutrons in this work.

The first mechanism corresponds to nuclear reactions arising from the interaction of the proton beam inside the target assemblies after extraction. The proton beam passes through the collimator, the vacuum window, and the target window before reaching the material used to produce the radioisotopes of interest. The current of the incident protons is well known by measurements. The interaction of the proton beam with these materials causes direct activation of the target components and the production of secondary neutrons. Each of the eight target ports can be understood as individual sources of neutrons.

The second mechanism corresponds to beam losses inside the machine during proton acceleration. These losses are mainly caused by single ionizations of the H$^-$ ions by the residual gas of the vacuum system. The neutral H atoms are not guided anymore by the magnetic field and impact most likely on the vacuum chamber of the cyclotron. Consequently, the vacuum chamber gets activated and neutrons are emitted. The vacuum chamber acts therefore as another source for secondary neutrons. The beam losses during acceleration are on the order of 40-50 % [21].

To calculate the phase space distribution of the neutrons as they are produced by the proton interactions, Monte Carlo simulation techniques were applied for each of the sources (eight targets plus vacuum chamber). FLUKA, which is a fully integrated particle physics simulation package and widely used at accelerator laboratories, was used [22], [23].

More details about the implementation can be found inside my two articles attached to this document.

1.5.2 Transport calculations of neutrons and scoring of the neutron fluences

As already mentioned, the secondary neutrons created by the mechanisms presented above can travel relatively large distances in dense materials (the mean free path of an 18 MeV neutron in copper is about 6 cm). During their passage, they undergo frequent elastic and inelastic interactions with other nuclides until they are absorbed or simply decay. Because the neutrons are neutral, they dominantly interact via the strong nuclear force. At each interaction point, they change their directions and energies. They can create additional neutrons by interaction with nuclides (through (n,2n) reactions, for example). In order to score the fluence of neutrons at a location **A** of the facility, these processes should be considered for each individual neutron – obviously a difficult task. Fortunately, the task of neutron transport calculations including the scoring of the differential energy distributions can be fully automized within the FLUKA simulation tool as well. The only prerequisite is to have a sufficiently precise geometrical description of all relevant components of the cyclotron, the auxiliary devices inside the bunker and the bunker walls. Also, the information about the chemical compositions must be made available to the simulation program in order to calculate the proper probabilities for the different physical processes in each simulation step. The geometrical model of the facility at HUG, as used for the FLUKA calculations of this study, is illustrated in Figure 6. It is worth noting that the FLUKA radiation transport capabilities are not only limited to neutrons. The FLUKA code is a general-purpose Monte Carlo code simulating the interaction and transport of hadrons, heavy ions, and leptons. This will become important when applied, for example, to facilities with higher beam energies.
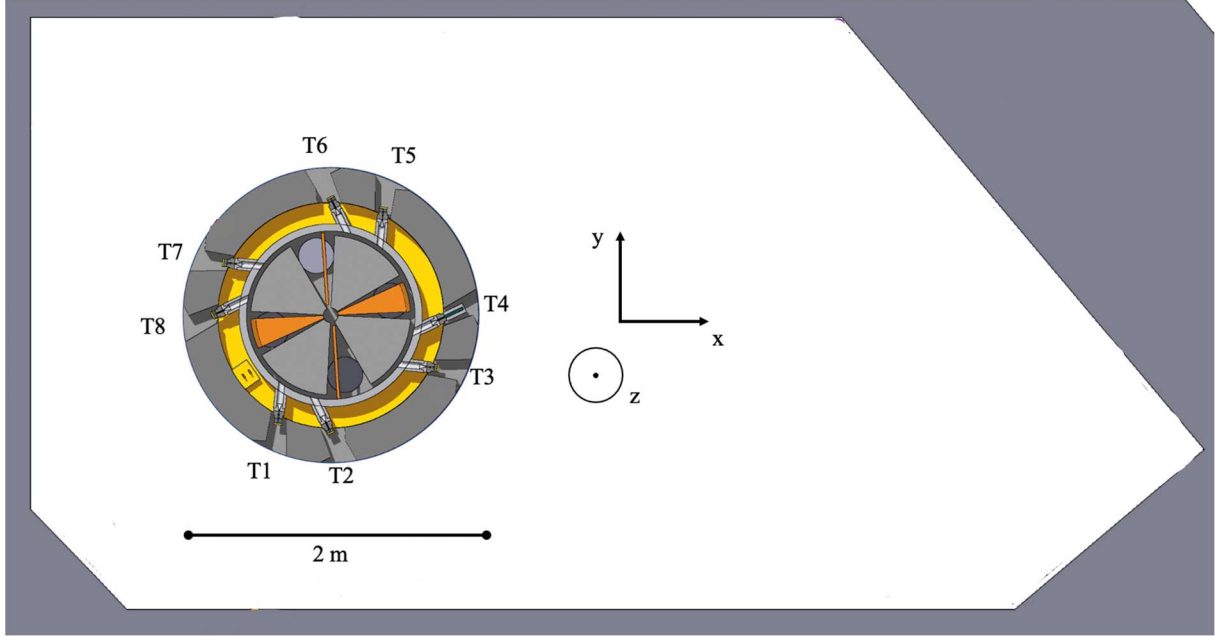
Figure 6. Geometrical model of the HUG cyclotron used for the simulation calculations in FLUKA.

1.5.3 Calculation of the activation of radionuclides for known particle fluxes

If the fluence of neutrons in a location is known, the activities of the artificially produced radionuclides inside a material can be calculated analytically by the formalism below. Since the formalism is also valid for other particle fields like protons, pions or gammas, we will talk about the particle type p_s.

The production rates $P_{e_k \to n_n}^{p_s}$ for radionuclides n_n produced in a chemical element e_k by the irradiation with primary or secondary particles of type p_s can be calculated by the convolution of the fluence spectra at the location of irradiation with the cross sections of all possible reactions involved. The production rates are expressed by the following equation:

$$P_{e_k \to n_n}^{p_s} = \frac{N_A}{M(e_k)} \int \sigma_{\sigma_{e_k \to n_n}}^{p_s}(E) \cdot \dot{\Phi}_{ps}(E) \, dE \qquad (2)$$

Here, $\sigma_{e_k \to n_n}(E)$ is the energy dependent cross section of $p_s + e_k \to n_n + X$, $\dot{\Phi}_{p_s}(E)$ is the time and energy differential fluence (flux) of primary and secondary particles p_s, N_A the Avogadro constant and $M(e_k)$ the molar mass of the element/isotope.

The number of radionuclides in a given location and for a given time t of irradiation can be calculated by solving the Bateman equation [24]:

$$Q_n^{p_s,e_k}(t) = \sum_{i=1}^{n} \left[\prod_{j=i}^{n-1} k_{j,j+1} \right.$$

$$\left. \times \sum_{j=i}^{n} \left(\frac{Q_i(0)e^{-k_j t}}{\prod_{\substack{p=i \\ p \neq j}}^{n}(k_p - k_j)} + \frac{S_i\left(1 - e^{-k_j t}\right)}{k_j \prod_{\substack{p=i \\ p \neq j}}^{n}(k_p - k_j)} \right) \right]$$

(3)

Here, Q_n is the number of atoms of species n present after a time t, k_n is the decay constant for species n ($k_n = \ln(2)/T_n$ with T_n being the half-life of the radionuclide n), $k_{n,n+1}$ is the partial decay constant (partial removal constant) and is related to the branching ratio $BR_{n,n+1}$ through the relation $k_{n,n+1} = BR_{n,n+1} \times k_n$. As source terms, $S_i = P_{e_k \rightarrow n_n}^{p_s}$ are used in the equation.

The transmutation of nuclei is not taken into account in Equation (3). This approximation is sufficient in cases with relatively low neutron flux, where the initial nuclide composition of the material stays almost unchanged. This is normally the case at CERN and at accelerators for isotope production.

The total number of radionuclides of species n of a material sample composed by K different elements/isotopes and being irradiated by the irradiation fields composed of S different particle types p_s can be determined with equation:

$$Q_n(t) = \sum_{s=1}^{S} \sum_{k=1}^{K} w_k Q_n^{p_s,e_k}(t)$$

(4)

The variable w_k denotes the weight fraction of the element/isotope inside the material. The activity is obtained by:

$$a_n(t) = k_n Q_n(t)$$

(5)

The variable k_n denotes the radioactive decay constant of radionuclide n. In case the irradiation field within a scoring volume is constant, $a_n(t)$ corresponds exactly to the specific activity within the volume. Otherwise $a_n(t)$ denotes the mean specific activity within the volume, which is the total activity divided by its mass.

Just as a final remark: Equation (3) gives the correct solution for irradiation fields with constant flux. Irradiation fields, which vary in time, can be approximated by sequential calculations of periods of time with virtually constant rates (so called irradiation patterns). Cooling periods can be considered by setting the source terms S_i in Equation (3) to zero.

1.5.4 The software packages ActiWiz

When the irradiation fields are known at a given location in terms of fluence spectra, the activation products and their activities can then be calculated in a very efficient way using the software package ActiWiz 3.3 developed at CERN. With the fluence spectra, the chemical composition of the material, the irradiation and cooling times as an input, the activities of all radionuclides inside the material are delivered in a few seconds or minutes by applying the formalism illustrated above, which can handle irradiation fields of neutrons, protons, charged pions and photons. The production rates for 85 different chemical elements and their isotopes can be treated in an energy range from thermal neutrons to 100 TeV [25]. The nuclide content of compound materials can be determined easily from these chemical elements. One of the main advantages of ActiWiz is that it gives fast access to the artificially produced radionuclides of materials of arbitrary chemical compositions when irradiated with known irradiation fields. Another essential benefit of ActiWiz is that the activities are calculated analytically. This is a significant difference to FLUKA where the scoring of residual nuclides is Monte-Carlo based and frequently suffers from poor statistics. The fast determination of production rates (Equation (2) and the subsequent calculation of activities of composite materials for irradiation fields (Equation (3), (4) and (5)) with complex time patterns is definitely one of the prime advantages of the 'ActiWiz 3.3' software package. Figure 7 summarizes the necessary steps for calculating the activation products and their activities.

RAW, a software which is constructed on top of ActiWiz, is used to automatize the different steps of the ActiWiz calculations. More details can be found in [26].
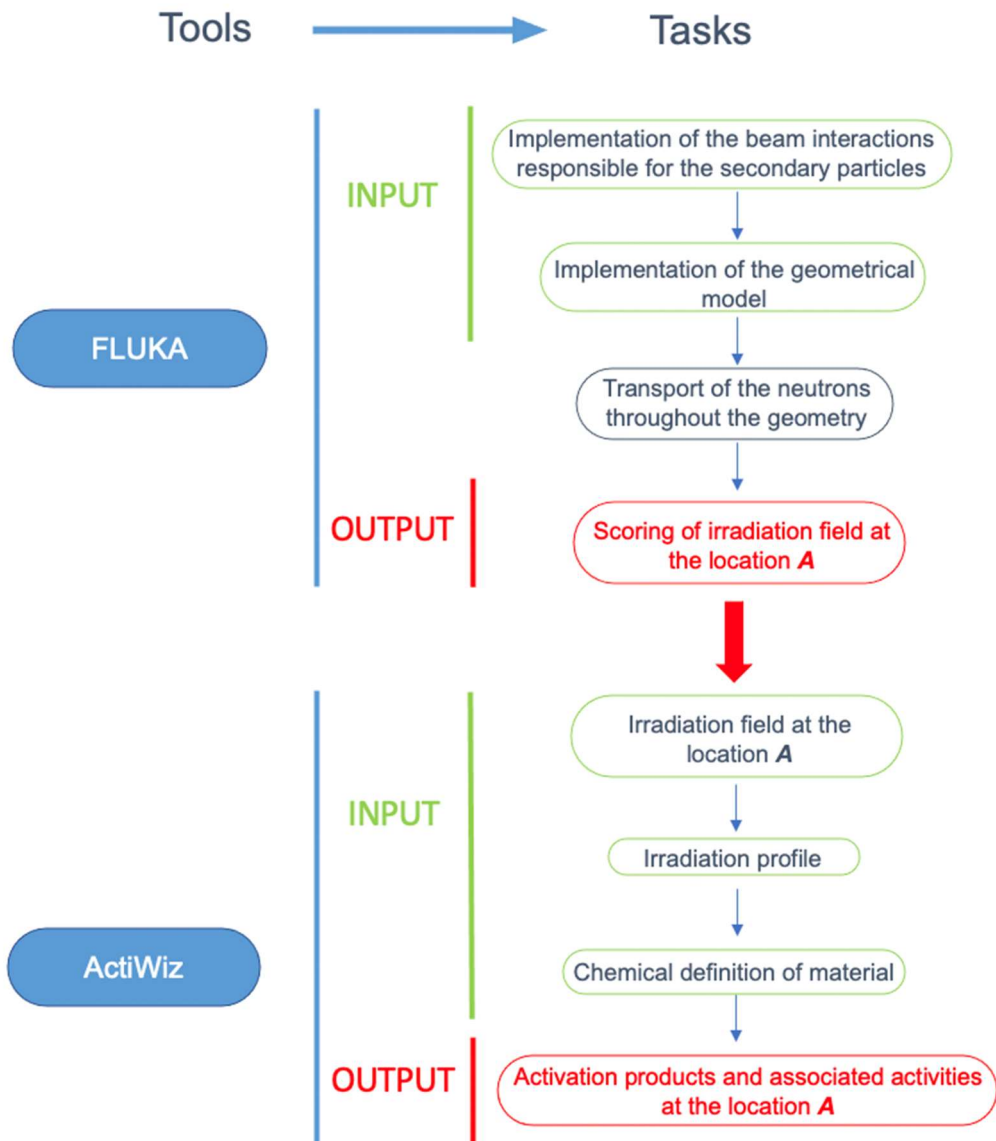
Figure 7. Schematic representation of the tools and associated tasks.

1.6   Outline of the PhD project

This PhD project was divided into three parts:

The first part focused on understanding the operation of the cyclotron in detail: from the proton beam production and its acceleration in the vacuum chamber to the production of radionuclides in the target assembly. This step is essential to understand the origins of the radiation fields, which will be at the origin of the activation of materials. To complete this stage, a Monte Carlo simulation model of the facility including the relevant secondary neutron sources was developed.

The second part of the project aimed to apply the method and the associated tools for the characterisation of the magnet coils of the cyclotron for the validation of the approach. These two coils were replaced by new ones because they have become leaky. They had to be characterized as radioactive waste. These defect coils allowed us to extract materials samples and to perform spectroscopy measurements for the validation of our simulation model. They allowed us to study the activation originating from the different neutron sources, here the targets and their components as well as the beam losses, inside a large volume surrounding the vacuum chamber of the cyclotron. The calculation results were compared with experimental measurements and made it possible to carry out, for the first time, a complete and transparent three-dimensional characterisation of the magnetic coils of a biomedical cyclotron for an irradiation period of 15 years. These results validated the proof of concept and confirmed the potential of the methods developed at CERN for the characterization of materials at low energy accelerators used in a medical environment.

The third part focused on extending the method to the surroundings of the cyclotron. The simulation model was evaluated using a non-destructive method by placing samples with known chemical composition during periods where the proton load was well documented. The comparison of the results made it possible to validate the use of the method for materials around the cyclotron.

The results of the second and third part of my thesis studies are described in detail in two scientific publications. The first one with the title 'Radiological characterisation of the magnet coils of a biomedical cyclotron' has been published. The second with the title 'Activation

studies within the bunker of a biomedical cyclotron' was submitted to 'Applied Radiation and Isotopes' and is presently reviewed. A short summary of these publications is given in the chapter 2 below.

2 Summary of the results of my publications

2.1 Radiological characterisation of the magnet coils of a biomedical cyclotron

The magnet coils of the cyclotron at HUG had to be replaced after 15 years of operation because of leaks inside the water-cooling system. The coils are mainly made of copper and weigh 2.4 tons. The leaky coils were placed in the radioactive waste area for their radiological characterisation, a necessary step in order to identify the most appropriate disposal path of these radioactive objects. In this case, the characterisation is equivalent to determining the three-dimensional distribution of activities of the activation products, which are relevant to determine the hazardousness of the material. To obtain the distributions, I combined the results of γ-ray measurements of material samples of the coils with the results of calculations as described in Section 1.5 for the different neutron sources. To implement a suitable model for the production of secondary neutrons to the Monte Carlo program, the beam interactions with matter inside the machine had to be analysed in detail. A geometrical model of the entire facility has been added to the code for the neutron transport calculations. The analysis and the implementation of the beam interactions and geometry to FLUKA were all carried out by me. The development of the Monte Carlo model was guided by the measured activities of material samples of the coils. They were essential for validating and optimising the model assumptions.

The magnet coils are ideal objects for testing the calculation methodology since they surround entirely the vacuum chamber of the cyclotron at the height of the plane of acceleration. They make it possible to probe the emission of neutrons originating from inside.

The main results of the full radiological characterisation of the magnet coils were documented in my first publication. Since the results are largely based on my personal work, I acted as the main and corresponding author. The main findings are briefly summarised below.

2.1.1 Summary of the results

As already mentioned, secondary neutrons are produced either by the interactions of the beam particles after extraction inside the different target assemblies to produce radioisotopes or by

the beam losses during acceleration. In a first step, the components of the target assemblies as neutron sources were characterised by simulations. The components are the stripper foils, the target and vacuum windows, the collimators, the target body[1] and, finally, the target materials for the radionuclide production. The integrated neutron yields per incoming 18 MeV proton hitting the target have been evaluated for each component of the target assemblies. The results are summarized in the Table 5.

The target assembly for the production of ^{18}F is the strongest emitter of neutrons followed by the assembly for ^{13}N and ^{11}C target. In the case of ^{18}F, the neutron production is dominated by the target material. On the contrary, in the case of ^{13}N, neutrons are mainly coming from the target body, the collimator and the target windows, while the contribution from the target material is relatively small.

In order to estimate the impact of each target assembly on the activation of components of the facility, the integrated beam currents must be taken into account. Table 6 summarizes, the total number of delivered protons and the neutron yield for each of the neutron sources for the operation of the cyclotron during the period from 2005 to 2015. The number of neutrons produced is in first approximation a good indicator for the activation and allows to evaluate the strongest sources of activation. T1, T2, T5 and T6 are the strongest emitters of neutrons, which are simultaneously the main contributors for the hotspots seen inside the coils. The target assemblies T1 to T8 act here like quasi-isotropic neutron sources while the beam losses on the vacuum chamber (BL) causes neutron emissions from a cylindrical surface. Beam losses cause an activation inside the magnetic coils, which is uniformly distributed in φ.

Table 5. Neutron yield per proton for the target assemblies. The contribution of each component is shown separately.

Neutron yield (n/p)	Target type		
Components	^{18}F	^{11}C	^{13}N
Stripper foil	1.7×10^{-7} (< 0.1 %)	1.7×10^{-7} (< 0.1 %)	1.6×10^{-7} (< 0.1 %)
Target window	4.2×10^{-4} (7 %)	4.3×10^{-4} (39 %)	2.1×10^{-4} (7 %)
Vacuum window	6.2×10^{-5} (1 %)	6.2×10^{-5} (6 %)	6.2×10^{-5} (2 %)
Target material[2]	2.7×10^{-3} (46 %)	4.6×10^{-4} (41 %)	1.4×10^{-5} (< 0.1 %)
Collimator (20 % of losses)	1.6×10^{-4} (3 %)	1.6×10^{-4} (14 %)	1.6×10^{-4} (5 %)
Target body[2]	2.5×10^{-3} (43 %)	-	2.5×10^{-3} (85 %)
Total	5.8×10^{-3} (100 %)	1.1×10^{-3} (100 %)	2.9×10^{-3} (100 %)

---

[1] In my first publication, the interactions of the proton beam with the target body have not been considered. It has been shown in my second publication that a part of the proton beam probably interacts with the target body in the case of the liquid targets. Table 5 has been updated accordingly.

[2] I assumed here that the proton beam interacts equally with the target material (50 %) and the target body (50%) for the ^{18}F and ^{13}N liquid targets.

Table 6. Neutron yield as a function of target T1 to T8 for the 2005-2015 irradiation period.

Source	Radionuclide produced	Integrated current [protons]	Neutron yield
T1	^{18}F	1.8×10^{21}	1.1×10^{19}
T2	^{18}F	8.3×10^{20}	4.8×10^{18}
T3	-	0	0
T4	^{11}C	8.1×10^{19}	9.0×10^{16}
T5	^{18}F	9.8×10^{19}	5.7×10^{17}
T6	^{18}F	8.0×10^{20}	4.7×10^{18}
T7	^{13}N	1.2×10^{20}	3.5×10^{17}
T8	-	0	0
BL	-	3.7×10^{21}	7.0×10^{17}

In a second step, the inhomogeneous distribution of the artificially produced radionuclides within the copper coils was determined. For this purpose, the coils were divided into 216 sub-volumes for the scoring of the differential neutron fluences. A cylindrical coordinate system (r, φ, z) was defined for the mathematical description of each of these sub-volumes.

The analysis of the beam interactions inside the cyclotron showed that the differential neutron flux inside a volume can be estimated reasonably well by the superposition of the neutron fields emitted by each individual target assembly plus the neutron field emitted by beam losses during the acceleration phase. Accordingly, independent simulations were performed for each of these neutron sources. The corresponding neutron fluences were scored within the 216 sub-volumes.

To calculate the activation products of a source in each sub-volume by ActiWiz, realistic beam currents, measured by the control system of the cyclotron over the last 15 years, were applied. The total activity of a radionuclide inside a sub-volume was obtained by summing over the contributions from all sources.

The results from my studies indicated that only two radionuclides are relevant for the waste management after a cooling period of 2.5 years, the moment the coils were investigated for the first time. These are ^{60}Co, which is a gamma emitter, and ^{63}Ni which is a "difficult to measure", low energy β^- emitter. A strong inhomogeneity was observed for the activity distributions. The concentration of ^{60}Co and ^{63}Ni varied by about three to four orders of magnitude from 10^{-2} to 10^2 Bq/g and from 10^{-1} to $2 \cdot 10^2$ Bq/g, respectively. The results from the simulation also showed that contributions from beam losses are only relevant at locations with low activation.

The simulation results on the activities of ^{60}Co were compared with the measurement results of material samples, which were taken from 58 different locations on one of the coils.

The comparison showed a good qualitative agreement of the three-dimensional distribution of the activities, which varies by order of magnitudes. It seems, however, that the simulation systematically underestimates the values for ^{60}Co by roughly a factor of 2.5. By investigating systematic uncertainties, I could exclude the precision of the geometrical model used in FLUKA as a possible reason. I also validated the correctness of the analytical approach of ActiWiz. The origin of the normalisation factor was not yet fully understood at this stage of my thesis and triggered additional investigations. They are discussed in more detail in my second publication.

In order to improve the predictive power of the simulation, an empirical and conservative correction factor of 2.5 was applied to the results for the radiological characterisation of the coils. Although the uncertainties of the simulation calculations are not negligible, clear conclusions can be drawn from the results. After 2.5 years of cooling, the biggest part of the coils must be classified as radioactive. However, after 30 years, more than 85% of the material could be cleared. After homogenisation, all material could be recycled.

2.1.2 **Addendum to the published results**

^{63}Ni is a pure β^- emitter, therefore its activity cannot be measured directly by HPGe-spectrometry. A few months after my first publication, the results of a radiochemical analysis of five material samples of the coils performed by an external company (JACOBS, Warrington, UK) became available. The applied procedure has been as follows:

- Dissolving the copper samples.
- Separation of nickel by anion-exchange chromatography.
- Measurement of the Ni-63 activity by liquid scintillation counting.
- Cross calibration of the result with a Ni-63 reference solution.

The samples were strategically selected from locations with different activities and different ratios of ^{60}Co/^{63}Ni. The selection of the samples was guided by the simulation results. These samples allowed us for an experimental validation of the simulation results of ^{63}Ni.

Figure 8 compares the measured and simulated activities for ^{63}Ni. The activities are plotted here as a function of the azimuthal angle φ for the positions P1, P3, P7 and P9. Figure 9 defines the coordinate system, which is used. The results of the comparison between measurement and simulation for the five selected samples for ^{63}Ni and ^{60}Co are shown in Table 7. The mean ratio between the measured and simulated activities of ^{63}Ni is 1.1 ± 0.3 for these samples. Both are in good agreement. For comparison: the same samples deliver a mean ratio

of 2.7 ± 0.5 for ^{60}Co. The origin of the difference between ^{63}Ni and ^{60}Co is not fully understood. Possible explanations are related to uncertainties of the production cross-sections of the nuclides or uncertainties in the energy dependency of the neutron fluence scored by FLUKA. This problematic was also revisited in my second publication, which will be summarised next.
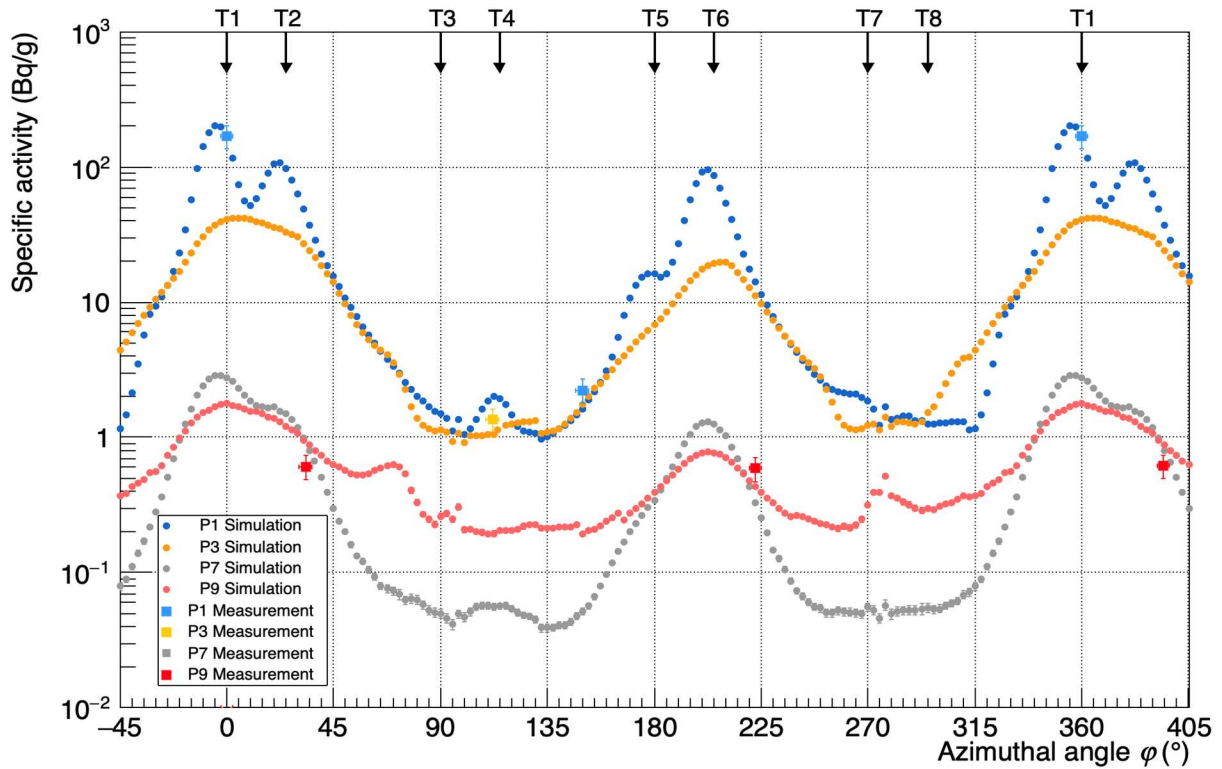

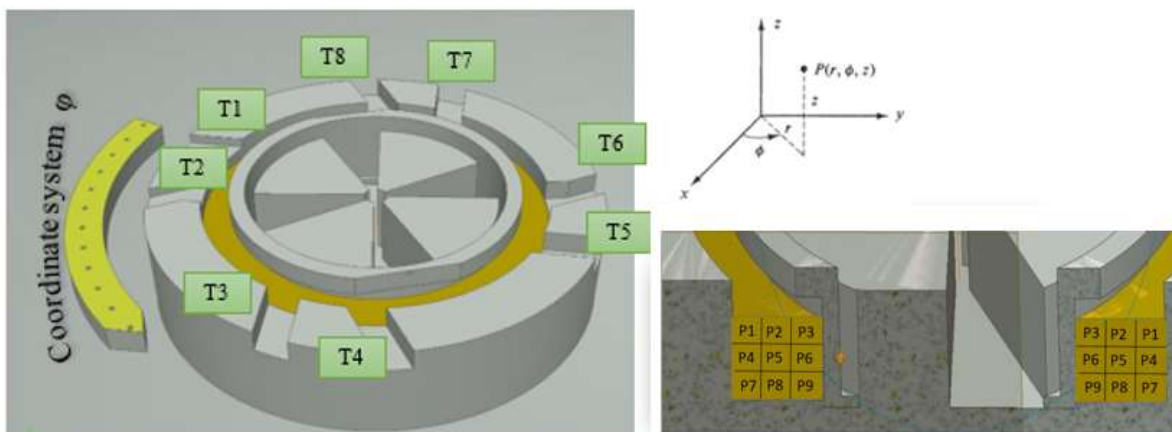Figure 8. Simulated azimuthal distribution of ^{63}Ni in comparison with the measurements.

Figure 9. Schematic view of the cyclotron showing the cylinder coordinates defined for the coils. The target positions are defined as T1 to T8. The positions P1 to P9 are shown on the right. $\varphi = 0$ is defined by the location of T1, which is next to the hotspot of the coil.

Table 7. Comparison between measurement and simulation for the five selected samples. The results are shown for ^{63}Ni and ^{60}Co. The uncertainties of measurement are given for 1 sigma. The statistical uncertainties for simulation values are below 1 %.

Position	φ (°)	^{63}Ni			^{60}Co		
		Measurement [Bq.g^{-1}]	Simulation [Bq.g^{-1}]	Ratio Meas./Sim.	Measurement [Bq.g^{-1}]	Simulation [Bq.g^{-1}]	Ratio Meas./Sim.
P1	0	169 ± 33	171	1.0 ± 0.2	106 ± 15.9	42.3	2.5 ± 0.4
P1	150	2.2 ± 0.4	1.6	1.4 ± 0.3	0.73 ± 0.11	0.25	3.0 ± 0.5
P3	112.5	1.3 ± 0.3	1.0	1.2 ± 0.3	0.39± 0.06	0.12	3.2 ± 0.5
P9	222.8	0.6 ± 0.1	0.4	1.4 ± 0.2	0.16 ± 0.02	0.082	2.0 ± 0.3
P9	34.5	0.6 ± 0.1	0.9	0.6 ± 0.1	0.09 ± 0.01	0.032	2.7 ± 0.3

2.2 Activation studies within the bunker of a biomedical cyclotron

I applied the same simulation model, which was already used for the magnet coils, for the radiological characterisation of materials inside the bunker of the cyclotron. There were no modifications on the model except the irradiation profiles (beam currents on target). They were adjusted to the new irradiation periods. I tested the simulation by comparing the results to two measurement campaigns with material samples that had been irradiated inside the bunker. There were obvious reasons for this project. First, extending the applied methodology to other parts of the facility can show the universality of this approach and its limitations. Certainly, it would be beneficial to have only a single tool, which can predict the activation levels of many components of such a facility. Second, measurements at other locations could give new insights to the origin of some uncertainties, which were observed in my first project. Finally, this study could also deliver valuable results for the radiological classification of material from the bunker, which could then be used for future decommissioning procedures.

The results linked to this study were submitted for publication in 'Applied Radiation and Isotopes'. The main results are summarised below.

2.2.1 Summary of the results

Selected samples made of different materials were placed in key positions inside the bunker. The precise chemical compositions of these samples were measured by an external laboratory beforehand. Those samples had been irradiated over two separate periods for which the beam currents and the production of the medical radionuclides were well documented. The first campaign corresponds to the simplest situation possible, where only one target (T1) was used to produce ^{18}F during one week. This target is the strongest source of secondary neutrons of the

cyclotron. Three samples were located on the wall directly in front of the target at a distance of about 1 meter. The samples were made from copper (CuOFE), stainless steel (ST304L), and an aluminium alloy (Al-6082). These are typical materials, frequently used for technical constructions - also in the environment of accelerators. The second campaign corresponds to a more realistic scenario, where eight sample-bags, each filled with the materials mentioned above, were placed throughout the bunker. They were irradiated for almost one year. During that time, four different target ports (T1, T2, T5 and T7) were used to produce ^{18}F and ^{13}N. The number of protons interacting with the target material of each target used during the two irradiation campaigns are given in the Table 8. The cooling times between the end of irradiation and the spectrometry measurements were about 4 days and between 7 and 11 days for the campaign C1 and C2, respectively.

Table 8. Total proton hitting each target for the two irradiation campaigns

Target	Total proton	
	C1	C2
T1	9.70×10^{18}	3.14×10^{20}
T2		5.63×10^{19}
T5		6.42×10^{19}
T7		1.81×10^{19}

The material samples of the first campaign were analysed using gamma spectrometry. Eleven different radionuclides were identified inside the three materials (nuclides with half-lives shorter than 5 days were omitted from this study). The activities of the identified radionuclides were then compared to the corresponding simulation results. All nuclides, which were predicted by the simulation as detectable, were indeed seen by the measurements. The simulation overestimated the activities of all the radionuclides except for ^{57}Co. The ratios between the activities (measurement/simulation) varied along an order of magnitude between 0.1 and 2.

The simple irradiation scenario made it possible to identify some of the limitations of the simulation model. My analysis of the systematic uncertainties provides some initial ideas regarding its shortcoming:

- The geometrical modelling of the target was simplified and did not take into account some geometrical details of the cooling system.
- The chemical composition and the density of the concrete of the walls influenced the flux of thermal neutrons.
- The phase state inside the cell is a mix between liquid and vapor and difficult to model.

- The FLUKA result for the neutron fluence emitted by $H_2^{18}O$ differs from those from experimental measurements.

The value of these uncertainties as function of the energy range of production of the radionuclide are summarized in the Table 9.

Table 9. The different sources of uncertainties as function of the energy range of production of the radionuclides.

Uncertainty source	Energy range of production	
	< 1MeV	> 1 MeV
	Uncertainty value	
Target geometry	< 5 %	About 30 %
Target phase	< 5 %	About 20 %
Concrete composition	Up to a factor 2.5	< 5 %
Neutron double differential emission from $H_2^{18}0$ target	Up to a factor of 3 depending on the emission angle and energy	

Especially the last point of the table above deserves some attention. A recent publication [27] has compared the double differential neutron yield as a function of energy and emission angle for a $H_2^{18}O$ target measured by [28] with the results of the simulation codes FLUKA, MCNP and PHITS. They show that these simulation tools differ significantly from the measured values. I therefore implemented into my simulation a neutron event generator using the experimental data for the neutron yield for target T1. In fact, most ratios between measured and simulated activities improved significantly for the first campaign. Additionally, a dedicated test demonstrated that this event generator also delivers more realistic activities for ^{60}Co at the hotspot of the magnet coils.

Some of the implications of the analysis of the uncertainties will be discussed in the final discussion of my thesis in Section 3.

In the second campaign, four different targets were operated for almost one year, a situation which corresponds to a more complex and realistic irradiation scenario. Several sample bags were distributed randomly all around the bunker. For these samples, I also found very similar systematic discrepancies between FLUKA and the measurements: the simulation overestimates the specific activity for most of the radionuclides. Although the irradiation scenario was more complex and the irradiation locations were distributed all over the bunker, the results agreed nevertheless with a precision similar to the first campaign.

By combining the results from both campaigns, I empirically extracted a confidence interval for the uncertainties of the activities by the simulation independent of the locations and

the reaction channels. All ratios between measured and simulated activities were within the interval [0.1, 2]. Although this interval is large, it still allows for meaningful simulation results.

In the following, I investigated the spatial distribution of the activation of aluminium, stainless steel, and copper along the walls of the cyclotron at the height of the beam for an irradiation period of ten years. At the end of this period all three materials would be radioactive at all these locations in terms of the liberation limits valid in Switzerland. About ten radionuclides have to be taken into account for the radiological characterisation of these materials. The spatial distribution of the activity of a radionuclide inside the bunker depends strongly on the energy range of the neutrons, which dominates its production. Activities produced at low energies have quite small variations all over the bunker. Radionuclides produced by neutrons above 1 MeV are mainly seen in front of the target ports. Their activities vary by at least two orders of magnitudes. After 30 years of cooling, two materials remain a concern. Stainless steel would be classified as radioactive at all positions along the walls with a concentration of ^{60}Co that is produced at low energies. Copper would exceed the clearance limits only at positions in front of the target ports for ^{18}F production, where ^{60}Co and ^{63}Ni are produced at energies larger than 1 MeV. Aluminium became non-radioactive at all locations. Although the uncertainties of the simulation are quite significant, clear conclusions can nevertheless be drawn for the radiological characterisation of materials inside the bunker based on my results. In cases where results are not conclusive, the simulations should ideally be complemented by direct measurements of material samples.

3 Discussion of the results

Compared to the large number of cyclotrons operated to produce radionuclides worldwide, the number of studies examining the characterisation of their activated materials is surprisingly small. A review of the literature shows that several studies have been performed on the characterisation of the materials of parts of the cyclotron itself [29]–[31] or walls of the bunker [32]–[34]. In all cases, the investigations have been limited to some spot tests. None of them gave a complete picture of the spatial distribution of the activations within larger components of the cyclotron or within the bunker. As this study shows, the strong gradients of the activity distributions make it hard to interpolate between two spots. The activities may change by two orders of magnitude within a distance of 10-20 cm, as I observed, for example, inside the magnet coils of the cyclotron at HUG. Without a doubt, tools which are able to predict the spatial distributions of activities within the components of a cyclotron facility would be of great help for the characterisation of materials.

Currently, the standard approach for calculating activations in accelerators are simulation programs like MCNP or FLUKA. They all have features implemented for the transport of the beam particles, the interaction of the beam particles with matter and the subsequent production of secondary particles, the transport of secondary particles and, finally, for calculating the activation products in matter including their decays. In principle it is possible to calculate the distributions of the activations using a pure Monte Carlo approach. But this proposition is hard to implement in practical terms because of the necessary computing time and the complexity of the requirements:

- During the operation of a PET-cyclotron, the beam conditions change frequently on an hourly basis. For each production cycle, different production targets may be used. The complete history of the beam conditions must be taken into account for the simulation. With the ongoing operation of the facility, its history must be updated. The full simulation would have to be repeated accordingly, which means days or weeks of computing time for each modification.
- If the activation process is calculated by the simulation program, the chemical composition of all components and objects has to be described correctly inside the program at the moment of calculation. If a small object is added (even just a screw) or the assumptions about a chemical composition change, the full simulation has to be repeated.

- The calculation of the artificially produced activities by simulation is expensive in terms of computing time. Even if the scoring of secondary particles, which are responsible for the activation processes at a given location, would deliver fluences with good precision, the statistics for a precise determination of the activities of artificially produced radionuclides may suffer from poor statistics. The number of required events for such a simulation run has to be increased significantly.

This approach has its limitations in terms of the available computing power and time. In the framework of my thesis, I developed a method for determining the spatial distributions of radionuclides within components of the cyclotron facility at HUG. The new approach, which was originally proposed by CERN, is based on the idea to split the calculations into two steps. The first step focuses on calculating the differential neutron fluences using traditional simulation techniques at the required locations with FLUKA. The second step calculates the activation products at that location analytically by using the software tool ActiWiz, a new software tool developed by CERN. It was the first time that ActiWiz was applied for a cyclotron in a medical environment.

My analysis of the beam interactions inside the cyclotron demonstrated that the differential neutron flux inside a volume, which is located outside the vacuum chamber, can be estimated reasonably well by the superposition of the neutron fields emitted by each individual target assembly plus the neutron field emitted by beam losses during the acceleration phase. Independent simulations can be performed for each of these neutron sources. This assumption, together with the two-step method described above, resulted in an approach (called hereafter 'two-step model'), which has obvious and essential advantages:

- The simulation of the secondary irradiation fields at a given location can be done independently for each of the sources. The results for the differential neutron fluences are expressed per incoming beam particle. It is not necessary to consider the time dependency of beam currents or the usage of other targets at the simulation stage.

- The activation products at a given location are calculated by ActiWiz analytically, which significantly reduces the required statistic of the simulation runs. The time dependency of the beam currents is used as an input to the ActiWiz calculations. In case of a modified irradiation history, it is unnecessary to repeat the full simulation.

- The modification of the chemical composition and the addition of smaller objects can be handled on the level of ActiWiz without repeating the full simulation, if the modifications don't have a significant influence on the neutron fluences themselves.

In a first project, I applied my 'two-step model' for determining the distribution of all activation products inside the magnet coils of the cyclotron after 15 years of irradiation. The analysis resulted in a detailed three-dimensional radiological characterisation of the coils. That project found that the only two radiologically relevant radio nuclides were ^{60}Co and ^{63}Ni.

The concentration of ^{60}Co and ^{63}Ni varied by more than three orders of magnitude from 10^{-2} to 10^{2} Bq/g and from 10^{-1} to $2\cdot10^{2}$ Bq/g, respectively. The highest activity values were linked to the target ports for ^{18}F production, which are the strongest sources for secondary neutrons. The results from the simulation also showed that contributions from beam losses were only relevant at locations with low activation. The simulation results were compared with the measured activities of ^{60}Co for material samples from 58 different locations and with the measured activities of ^{63}Ni from 5 different locations. Qualitatively, the simulated and measured distributions agreed well over the full dynamic range of activation. The quantitative analysis showed, however, that the ^{60}Co activations were on average underestimated by the simulation by a factor 2.5 - more or less independent of the location of the samples. For ^{63}Ni, in contrast, the simulation and measurement results agreed nearly perfectly within a factor 1.1 in average.

Before discussing possible reasons for the uncertainties of ^{60}Co, I want to recapitulate the main findings of the first measurement campaign of the second project. Samples, made from copper (CuOFE), stainless steel (ST304L), and an aluminium alloy (Al6082) were placed straight in front of the target T1 at the wall of the bunker for one week of irradiation. Only this target was used during that period, making it the simplest irradiation scenario possible. Nonetheless, the ratios between the activities (measurement/simulation) varied over an order of magnitude between 0.1 and 2. Ten radio nuclides were included for the comparison. While the activity of ^{60}Co was generally underestimated inside the magnetic coils by my model (also at the hotspot, which is next to target T1), all the activities of the samples next to the wall were overestimated.

A thorough analysis of the systematic uncertainties identified the four points already described in paragraph 2.2.1 as possible explanations (for a more detailed discussion please refer to my publications in section 6.1 and 6.2).

While the full model of the cyclotron includes 25 tons of material, a few missing grams at certain locations may already have a visible impact. This should be taken into account when the geometry is designed in FLUKA - something that should be improved in my model.

The kind of concrete used for the bunker walls has a significant impact on the fluence of thermal neutrons. The traceability of such information should be guaranteed during the life cycle of an installation until its removal. This uncertainty contributes with almost a factor of two to the uncertainties of nuclides produced at low energies, like ^{60}Co in stainless-steel. Also, for new installations, the choice of concrete should be made with prevision and care.

It seems that a part of the proton beam does not interact with H$_2$^{18}O directly, but with the target body instead. More than 1 kW of power is dissipated by the beam inside the cell within a very small volume of 3 cm^3, heating up the liquid and pressurising the cell to roughly 30 bars. While the cells are filled to only 60 % of their volume, the distribution H$_2$^{18}O inside the cell and its phase is not very well known. Also, after discussing with the producer of the cyclotron, I did not receive the necessary information for a more detailed implementation of the target material to my FLUKA model.

Possibly, the phase space distribution of the neutrons emitted by the H$_2$^{18}O-targets is not perfectly described by our Monte Carlo tool as it has been reported by [27]. The results in this publication indicate a discrepancy of a factor of two or more, when comparing the double differential neutron yield obtained by FLUKA simulations with measurements [28] for certain emission angles and energies (see Figure 10).

I implemented an event generator for the neutrons emitted by the H$_2$^{18}O-target T1 based on these experimental results. Indeed, the agreement between simulation and measurement improved significantly. This is not only the case for the samples next to the wall downstream of target T1 at zero degrees relative to the beam. Also, the simulated activity for ^{60}Co inside the magnet coils next to T1 improved (emission angle > 115 degrees). My data is in favour of the event generator. The results agreed within a factor of three with the measured activities.

Since no experimental data were available below 1.75 MeV, I used the FLUKA data normalized to the experimental data for this part of the spectrum. However, I observed using FLUKA that the missing part of the spectrum contributes to a non-negligible part (40 %) of the overall thermal neutron spectrum at the sample location. The situation needs further clarification, including experimental results for neutrons below 1.75 MeV.

In a publication from Konheiser et al. from 2019 [35], the activation of material samples next to a H$_2$^{18}O-target was measured and compared to simulation calculations with FLUKA. They found good agreement between simulations and experimental results, with calculation to experiment (C/E) ratios well between 0.6 and 1.4 for most of the radio nuclides. For three

reactions C/E values as low as 0.12 were nevertheless observed. However, they stated in their publication that their observations seem to contradict the experimental results in [28], [36]. Their samples were positioned at the surface of the target housing. Because of the different locations, a direct comparison with my results is therefore not possible. In addition, they had not taken into account proton reactions within the target body – they assumed a filling level of the target cell of 100 %, which seems to be unrealistic. But we agree fully with the conclusion of Konheiser that further experimental clarification is required in order to provide validated absolute neutron fluence spectra emitted from $H_2{}^{18}O$-targets.

Although there are doubts about the correctness of the double differential neutron yield, FLUKA seems to deliver the right amount of ^{18}F nuclides produced inside the target cell, which is in good agreement with literature (see Table 10).

When simulating the production of secondary neutrons inside the targets T4 and T7, I observed a significant difference between FLUKA and the production yields of ^{13}N and ^{11}C published by IAEA [37]. The differences, shown in Table 10, are on the order of 20% and 40%, respectively. Also here, the underlying models in FLUKA should be revisited.

Table 10. Comparison of the activities expected by FLUKA with those expected by IAEA [37]. The activities are given after one hour of irradiation with a beam current of 1 μA.

Radionuclides	Activity FLUKA (GBq)	Activity IAEA (GBq)	FLUKA/IAEA
^{18}F	4.15	4.29	0.97
^{13}N	1.97	1.64	1.20
^{11}C	7.98	5.51	1.45
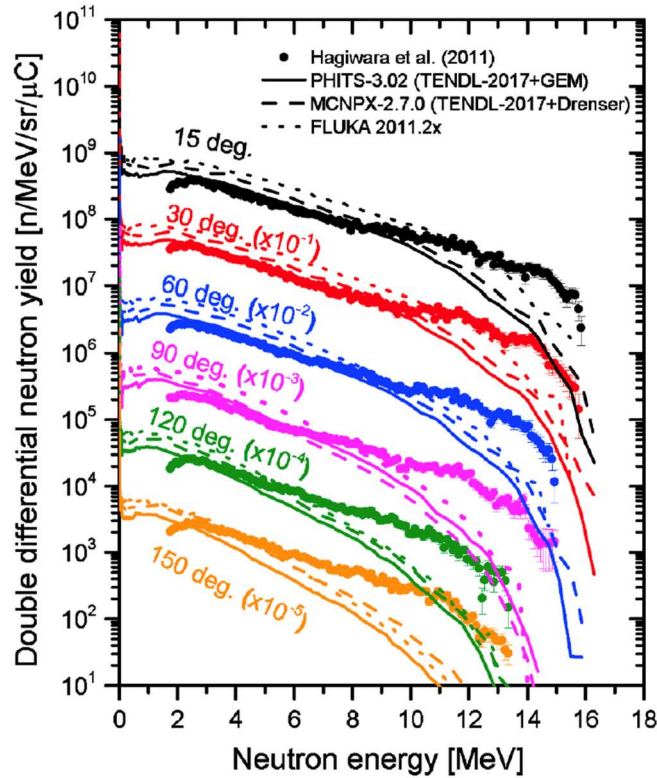
Figure 10. Double differential neutron emission for the target producing ^{18}F. Experimental values are shown with the simulated values [27].

I demonstrated that the cross sections responsible for the production of secondary neutrons inside the targets are not necessarily well described by FLUKA. The related uncertainties should be taken into account. Also, the cross sections of the nuclear reactions which are responsible for the activation of materials have uncertainties, which can be significant. Because of the relatively large uncertainties of the neutron fluences at the location of the samples, my studies did not allow to conclude on the uncertainties of these cross sections used in ActiWiz and FLUKA. It would be preferable to have dedicated experiments in an environment with well-known neutron fluences and to provide a clearer picture on this topic.

Despite the relatively large uncertainties of the activation calculations, I have shown that clear conclusions can be drawn for the radiological characterisation of materials from the cyclotron facility at HUG. This was the case for the three-dimensional activity distribution inside the magnet coils of the cyclotron. This was also the case for the activity distribution along the walls of the bunker of the facility. Uncertainties can be partially compensated by choosing conservative cooling down periods before activated material is released. In cases where results are not conclusive, the simulations should ideally be complemented by additional measurements of activities via material samples. This should not hide the fact that the

uncertainties of the simulation calculations should be further reduced. My analysis of the uncertainties provides some initial indications for possible improvements regarding the Monte Carlo calculations of PET-cyclotrons.

It is worth referring to a recent IAEA report [38] which stated that simulations when compared to measurements show a typical agreement within a factor of ten. Hopefully, this factor can be reduced significantly in the near future.

4 Conclusion

The activation of components of particle accelerators and of materials in their surroundings have to be radiologically characterised for a comprehensive risk assessment and for the definition of a radioactive waste strategy.

In this context, I developed an efficient method which enables the seamless determination of the distributions of activities of the artificially produced radionuclides inside the components of a PET cyclotron facility at HUG. The approach, which was originally proposed by CERN, is based on a calculation of the activities using two steps. The fluences of secondary particles are scored inside the objects in a first step using the simulation tool FLUKA. This is followed by an analytical calculation of the activities by using these fluences in a second step as an input to ActiWiz, a new software tool recently developed at CERN for the characterization of activated material. It has been the first time that this approach was applied to a low energy PET-cyclotron in a medical environment. A detailed analysis of the mechanisms, which lead to the production of secondary neutrons at the PET cyclotron facility was necessary and had to be integrated into the FLUKA model.

I demonstrated the feasibility of using this method in two studies. One involved the three-dimensional distribution of activities inside the magnet coils of the cyclotron. The second concerned the distribution of activities along the wall of the bunker of the facility. These distributions were qualitatively well described. The agreement between the predicted activities and measurements were roughly within a factor three. A detailed analysis of the uncertainties showed some shortcomings of the geometrical model I applied in FLUKA. No detailed information was available, for example, about the chemical composition of the bunker walls of the facility. These walls play an important role in the creation of thermal neutrons. Thermal neutrons for their part are responsible for a large part of the activation within the bunker. The composition of the walls should be a posteriori analysed and the model updated accordingly.

35

Of general interest for the simulation of PET facilities are the reaction mechanisms inside the target materials for the production of radionuclides. A recent study suggests that the double differential (emission angle and energy) neutron yield of the targets producing ^{18}F may not be well described in several Monte Carlo tools, including FLUKA. This may be one of the main limitations to the uncertainties reported here. I also observed discrepancies for the production yields of ^{13}N and ^{11}C of 20% and 40 %, respectively, when comparing simulation results with values taken from the literature. It is in the interest of the entire community that the implementations of the most important reaction channels inside the Monte-Carlo tools are revisited and validated. This is a key element for more precise simulation tools in future.

My methodology and studies can also be extended to the yoke of the cyclotron and the walls of the bunker. Based on the results presented here, the calculation of the three-dimensional distributions of activities inside these components seems to be feasible. The calculations should be accompanied again by the measurements of a sufficiently large number of material samples in order to validate the calculations, to determine the uncertainties, and to guide any necessary modifications of the simulation model. With these two additional components, a large fraction of the activated materials inside the facility would be radiologically characterized.

In conclusion, I would like to summarize the lessons learned from these studies. We have shown that activation of parts of the facility can be described by the superposition of only a few sources of secondary neutrons, namely the target assemblies and the beam losses during acceleration.

The calculation time for the activities of radionuclides inside materials was reduced significantly compared to a pure simulation approach by using the software tools ActiWiz and RAW. I have also shown that both, ActiWiz and FLUKA, give the same results in terms of activities.

I would like to make an important remark about both, the ActiWiz and FLUKA calculations: Only the statistical uncertainties based on the number of simulated events are propagated. Uncertainties related to the reaction cross-sections or to the limited precision of the geometrical model are not considered automatically. These systematic uncertainties can be limiting and must be considered in detail.

For the evaluation of the uncertainties, simulation calculations should be complemented

by control measurements whenever feasible. When this is not possible, for example when building up a new facility, the systematic uncertainties should be estimated in a conservative way and added to the simulation results.

There are about 200 cyclotrons of type IBA 18/9 Cyclone operated worldwide [19]. Therefore, the optimization of the software tools, which would facilitate the characterization of waste at the end of their life cycles would be beneficial for the community. The validation of the nuclear cross sections and its implementation with the associated uncertainty into the software tools would be for sure beneficial in this field.

I hope that the conceptional studies presented here inspire other groups to improve and optimize such tools for the characterisation of PET-cyclotron facilities in the future.

5 References

[1]   "MedAustron." https://www.medaustron.at

[2]   "ADAM." https://www.avoplc.com/en-gb/

[3]   "Medicis CERN." https://home.cern/science/experiments/medicis

[4]   CERN, *The High-Energy Network*, Jun. 05, 2019. https://alumni.cern/news/196593

[5]   H. Vincke and C. Theis, "ActiWiz 3 – an overview of the latest developments and their application," *J. Phys.: Conf. Ser.*, vol. 1046, p. 012007, Jun. 2018, doi: 10.1088/1742-6596/1046/1/012007.

[6]   P. Aarnio, "Decay and Transmutation of Nuclides," CMS NOTE 1998/086, Dec. 1998.

[7]   E. Mobs, *The CERN accelerator complex - 2019. Complexe des accélérateurs du CERN - 2019*. 2019. [Online]. Available: https://cds.cern.ch/record/2684277

[8]   A. Degiovanni and U. Amaldi, "History of hadron therapy accelerators," *Physica Medica*, vol. 31, no. 4, pp. 322–332, Jun. 2015, doi: 10.1016/j.ejmp.2015.03.002.

[9]   S. Livingston, "History of the cyclotron," presented at the Proceedings of the 7th International Conference on Cyclotrons and their Applications, Zurich, Switzerland, Aug. 1975. [Online]. Available: https://inspirehep.net/files/48b18c3bfd6d532d453cece9dfcf8245

[10]   SNMMI, "Important Moments in the History of Nuclear Medicine." http://www.snmmi.org/AboutSNMMI/Content.aspx?ItemNumber=4175

[11]   A. Yordanova *et al.*, "Theranostics in nuclear medicine practice," *OTT*, vol. Volume 10, pp. 4821–4828, Oct. 2017, doi: 10.2147/OTT.S140671.

[12]   "Encyclopedia of 20th-Century Technology." http://cw.routledge.com/ref/20ctech/cancer.html

[13]   A. Giulietti, "Laser-driven particle acceleration for radiobiology and radiotherapy: where we are and where we are going," Prague, Czech Republic, May 2017, p. 1023904. doi: 10.1117/12.2270945.

[14]   D. I. Thwaites and J. B. Tuohy, "Back to the future: the history and development of the clinical linear accelerator," *Phys. Med. Biol.*, vol. 51, no. 13, pp. R343–R362, Jul. 2006, doi: 10.1088/0031-9155/51/13/R20.

[15]   IAEA, "Radiological Safety Aspects of the Operation of Electron Linear Accelerators," Vienna, Technical Reports Series 188.

[16]   Eurostats, "Radiation therapy equipment in the EU." http://appsso.eurostat.ec.europa.eu/nui/submitViewTableAction.do

[17]   J. Weinbach, "Clinical relevance and cost-effectiveness of proton therapy," 2018. [Online]. Available: https://ec.europa.eu/health/sites/default/files/non_communicable_diseases/docs/ev_20181022_co08_en.pdf

[18]   A. Keresztes, B. Attila, and T. Csaba, "Therapeutic and diagnostic radiopharmaceuticals," Oct. 2015, [Online]. Available: http://real.mtak.hu/41305/1/225_247_BRC_2015_Vol_2.pdf

[19]   IAEA, "Cyclotrons used for Radionuclide Production," 2019. https://nucleus.iaea.org/sites/accelerators/Pages/Cyclotron.aspx#InplviewHashd5afe566-18ad-4ac0-8aeb-ccf833dbc282= (accessed Jan. 31, 2020).

[20]   IBA, "Decommissioning of an IBA Cyclone® 18 PET cyclotron facility," Apr. 2009.

[21]   A. I. Papash and Yu. G. Alenitsky, "On beam intensity upgrade in the commercial cyclotrons of negative hydrogen ions," *Phys. Part. Nuclei Lett.*, vol. 5, no. 5, pp. 469–472, Sep. 2008, doi: 10.1134/S1547477108050117.

[22]   A. Ferrari, P. R. Sala, A. Fasso, and J. Ranft, "FLUKA: A Multi-Particle Transport

Code," SLAC-R-773, 877507, Dec. 2005. doi: 10.2172/877507.

[23]   T. T. Böhlen *et al.*, "The FLUKA Code: Developments and Challenges for High Energy and Medical Applications," *Nuclear Data Sheets*, vol. 120, pp. 211–214, Jun. 2014, doi: 10.1016/j.nds.2014.07.049.

[24]   H. Bateman, "Solution of a system of differential equations occurring in the theory of radioactive transformations," Cambridge, 1910, pp. 423–427.

[25]   H. Vincke and C. Theis, "Mass production of nuclide production data used in the ActiWiz3 code."

[26]   R. Geyer, J. Damet, C. Theis, H. Vincke, M. Sotiropoulou, and V. Bonvin, "Radiological characterization of activated material at accelerators," The Hague, Netherlands, May 2019, pp. 6–13. [Online]. Available: https://irpa2018europe.com/wp-content/uploads/2019/08/IRPA2018-Proceedings-v2sec.pdf

[27]   M. Bakhtiari, L. Mokhtari Oranj, N.-S. Jung, A. Lee, and H.-S. Lee, "Estimation of neutron production yields from H218O as the 18F-production target bombarded by 18-MeV protons," *Radiation Physics and Chemistry*, vol. 177, p. 109120, Dec. 2020, doi: 10.1016/j.radphyschem.2020.109120.

[28]   M. Hagiwara *et al.*, "Spectrum Measurement of Neutrons and Gamma-Rays from Thick H182O Target Bombarded with 18 MeV Protons," *J. Korean Phy. Soc.*, vol. 59, no. 2(3), pp. 2035–2038, Aug. 2011, doi: 10.3938/jkps.59.2035.

[29]   A. Toyoda *et al.*, "Evaluation of induced activity in various components of a PET-cyclotron," *J. Phys.: Conf. Ser.*, vol. 1046, p. 012017, Jun. 2018, doi: 10.1088/1742-6596/1046/1/012017.

[30]   T. Fujibuchi *et al.*, "Evaluation of the distribution of activation inside a compact medical cyclotron," *Applied Radiation and Isotopes*, vol. 124, pp. 27–31, Jun. 2017, doi: 10.1016/j.apradiso.2017.02.045.

[31]   P. Guarino, S. Rizzo, and E. Tomarchio, "GAMMA-RAY SPECTROMETRIC CHARACTERIZATION OF WASTE ACTIVATED TARGET COMPONENTS IN A PET CYCLOTRON," presented at the Cyclotrons and Their Applications 2007, Eighteenth International Conference, CERN, 2007.

[32]   S. Vichi *et al.*, "Activation studies for the decommissioning of PET cyclotron bunkers by means of Monte Carlo simulations," *Radiation Physics and Chemistry*, vol. 174, p. 108966, Sep. 2020, doi: 10.1016/j.radphyschem.2020.108966.

[33]   S. Vichi *et al.*, "Activation studies of a PET cyclotron bunker," *Radiation Physics and Chemistry*, vol. 161, pp. 48–54, Aug. 2019, doi: 10.1016/j.radphyschem.2019.04.001.

[34]   J. J. Martínez-Serrano and A. Díez de los Ríos, "Prediction of neutron induced radioactivity in the concrete walls of a PET cyclotron vault room with MCNPX: Predicting neutron induced radioactivity in a PET cyclotron room walls," *Med. Phys.*, vol. 37, no. 11, pp. 6015–6021, Oct. 2010, doi: 10.1118/1.3505919.

[35]   J. Konheiser, S. E. Müller, A. Magin, B. Naumann, and A. Ferrari, "Source term calculation and validation for ^{18}F-production with a cyclotron for medical applications at HZDR," *J. Radiol. Prot.*, vol. 39, no. 3, pp. 906–919, Sep. 2019, doi: 10.1088/1361-6498/ab2ae8.

[36]   R. Méndez, M. P. Iñiguez, J. M. Martí-Climent, I. Peñuelas, H. R. Vega-Carrillo, and R. Barquero, "Study of the neutron field in the vicinity of an unshielded PET cyclotron," *Phys. Med. Biol.*, vol. 50, no. 21, pp. 5141–5152, Nov. 2005, doi: 10.1088/0031-9155/50/21/013.

[37]   IAEA, "Charged-particle cross section database for medical radioisotopes production," 2018. https://www-nds.iaea.org/medical/positron_emitters.html (accessed Jan. 31, 2020).

[38]   IAEA, "Decommissioning of Particle Accelerators," Vienna, Technical Reports NW-T-2.9, 2020.

6   Scientific articles

6.1   Detailed study of the activation of the magnet coils of a biomedical cyclotron

Detailed study of the distribution of activation inside the magnet coils of a compact PET cyclotron

V. Bonvin [a,b,*], F. Bochud [b], J. Damet [b,d], C. Theis [a], H. Vincke [a,c], R. Geyer [a,b]

[a] European Council for Nuclear Research (CERN), Esplanade des Particules, CH-1211, Meyrin, Switzerland
[b] Institute for Radiation Physics, Lausanne University Hospital, Rue du Grand-Pré, CH-1007, Lausanne, Switzerland
[c] University of Technology, Rechbauerstraße 12, 8010, Graz, Austria
[d] University of Otago, 2 Riccarton Ave, Christchurch, New Zealand

ABSTRACT

We determined the distribution of activation products inside the magnet coils of a medical cyclotron that has been operational for fifteen years. Besides FLUKA, we based our approach on new software tools (RAW and ActiWiz) developed for high-energy accelerators at CERN. A combined analysis of measurements on the coils with Monte-Carlo simulations resulted in a detailed three-dimensional radiological characterisation of the coils. Our results provide the required information for the radiation protection expert to identify the appropriate waste elimination scheme.

1. Introduction

Recently published data from the statistical office of the European Union (Eurostat, 2019a) shows a clear trend of increasing Positron Emission Tomography (PET) examinations in Europe for the 2012–2017 period. This trend is also confirmed by the fact that the number of PET scanners in France has almost doubled within the same period (Eurostat, 2019b). The fast development of nuclear medicine over the last few decades has involved the construction of production centres for short-lived radioisotopes using medical cyclotrons. More than 1200 of such centres have been registered worldwide by the IAEA (IAEA, 2019). Half of these cyclotrons are operating with energies between 16 and 19 MeV. The radioisotopes, which are typically used for PET examinations, are ^{18}F, ^{11}C and ^{13}N (IAEA, 2009), with half-lives of 109.7 min, 20.38 min and 9.97 min, respectively.

Alongside the obvious medical benefits, the use of particle accelerators also raises radiation protection issues. The components of the accelerator and its environment (bunker) may become radiologically activated during the operation phase. When cyclotron facilities are decommissioned, all their components must be radiologically characterised. The components shall be treated according to the local regulations (IAEA, 2003). The radiological characterisation represents the determination of the nature, location and concentration of radionuclides at a nuclear installation (NEA, 2013). This definition is also valid for accelerator facilities, where the radioactivity is artificially induced. A good understanding of the activation processes taking place inside and near the cyclotron is essential for an efficient characterisation. This is essential in order to establish the appropriate decommissioning procedure.

For this study, we conducted a detailed examination of a type IBA-Cyclone 18/9 cyclotron. After fifteen years of operation, the magnet coils were replaced during a technical service. The operation of the machine was continued after repair. The radiological characterisation of these coils became necessary in order to identify the most appropriate disposal path. In this case, the characterisation is equivalent to the determination of the three-dimensional distribution of activities of the activation products, which are relevant to determine the hazardousness of the material. To obtain the distributions, we combined results of γ-ray measurements of material samples of the coils with the results from Monte-Carlo simulations.

Several studies have already been published about the activation products inside materials of different medical cyclotrons (Calandrino et al., 2006) (Sunderland et al., 2012). They have estimated the total activities of the most important radionuclides produced inside several

components at these facilities. However, details about the distribution of the specific activities within these materials were not presented, which could deliver additional information for the characterisation and an optimised decommissioning procedure.

A recent article (Toyoda et al., 2018) about the induced activity in various components of PET-cyclotrons has examined the radionuclides that were induced in the metal components. The cyclotrons were of type IBA-Cyclone 10/5 and JSW-BC1710. They determined the depth distribution of the activation by extracting core samples on several components. Gamma-spectroscopy results are available for several locations of the yokes and the sector magnets. Only dose rate measurements are presented for the samples of the magnet coils. Detailed information on the distribution of activation inside the magnet coils is not given.

Here we give, for the first time, a complete and seamless picture regarding the distribution of the activation products over the full volume of the magnet coils of a medical cyclotron.

Because of its low energy (18 MeV), the proton beam is stopped after a few millimetres in matter (e.g. 3.5 mm in water). The target assemblies for the production of isotopes are integrated into the vacuum chamber. This means that beam protons cannot contribute directly to the activation of the magnet coils or any other element outside of the vacuum chamber. The activation of the coils is induced by secondary neutrons, which originate from interactions of the beam particles with the different target assemblies or with materials inside the vacuum chamber of the cyclotron. A good understanding of these neutron fields is essential for the successful characterisation of materials in and around the cyclotron. For this work, we implemented a consistent description of all relevant sources of secondary neutrons into a Monte-Carlo model for the cyclotron using FLUKA. Following FLUKA, ActiWiz and RAW were then applied in order to reduce the required computing time and to automate the analysis. The latter two are software tools developed at CERN for the characterisation of activated material at accelerators. This is the first time they are being applied for medical cyclotrons. We then compared the simulation results with those from γ-ray spectrometry. The following sections summarise the radiological characterisation of

the coils. The methodology described here can also be applied to other components of cyclotron facilities in order to obtain detailed information about the distribution of activations.

2. Materials and methods

2.1. Description of the biomedical cyclotron IBA cyclone 18/9

We studied a Cyclone 18/9 cyclotron from IBA that has been in operation since 2000 for the routine production of radioisotopes in a hospital unit. It is a compact accelerator with an energy of 18 MeV and a nominal beam intensity of 150 μA, which corresponds to 9.36×10^{14} protons/s. Furthermore, the accelerator can be operated with both protons and deuterons. However, for this study, the second option was used for the production of ^{15}O for two days only. The cyclotron has eight target ports used for the production of radioisotopes. Fig. 1 shows the most important components of the cyclotron: the deep valley magnet with yoke, poles and coils, the dual ion source, the dees for the acceleration of particles, the vacuum chamber and the targets. The cyclotron is mainly used for the production of ^{18}F, ^{13}N, and ^{11}C by using different target materials (liquid or gas). The key parameters of the machine and

Table 1
Main characteristics of the Cyclone 18/9 Cyclotron (IBA, 2009).

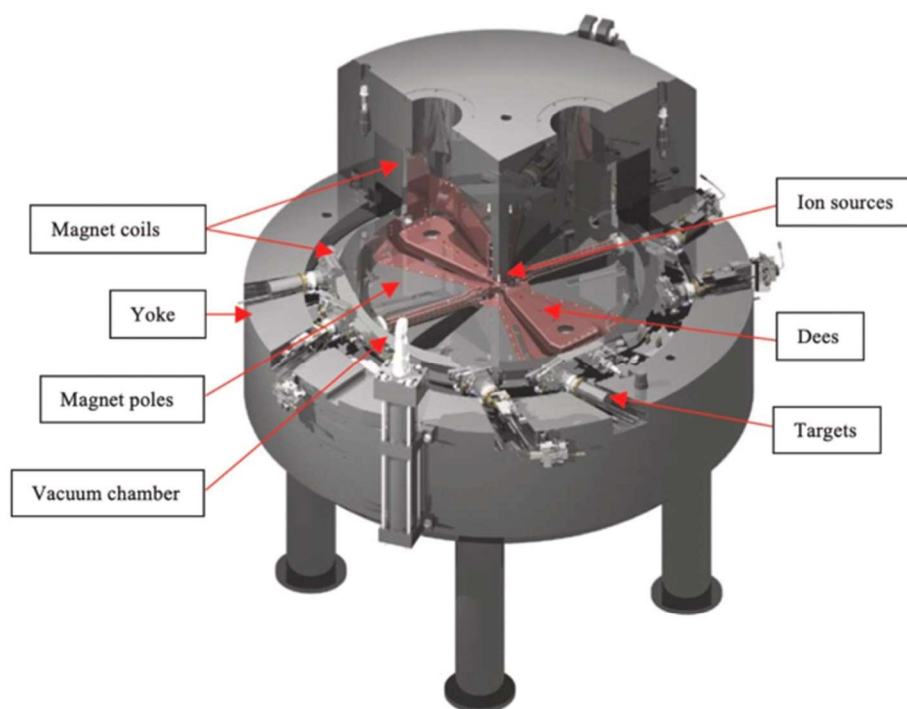| Energy (MeV)	proton	18
	deuteron	9
Intensity (μA)	proton	150 (9.36×10^{14} p/s)
	deuteron	40 (2.50×10^{14} d/s)
Particles sources		2 separate Penning Ion Gauge ion sources
Number of target ports		8
Simultaneous target beams		2
Mean field (T)		1.35
Weight (kg)		25,000

Fig. 1. Sketch of the Cyclone 18/9 cyclotron (IBA, 2009). (For interpretation of the references to color in this figure legend, the reader is referred to the Web version of this article.)

the characteristics of the different targets are summarized in Table 1 and Table 2, respectively. The main characteristics of the coils are given in Table 3. The copper of the coils follows the standard OFCu (oxygen free copper) type C1020 with a high purity better than 99.96%. Further details about this cyclotron can be found in the documents provided by the company (IBA, 2009).

The machine operators provided us with the required information about the operation of the cyclotron. In the years between 2005 and the end of 2015, the date when the coils were replaced, the cyclotron was mainly used for the production of ^{18}F and ^{13}N with the occasional production of small batches of ^{11}C. A typical example: a total activity of 26 TBq of ^{18}F and 1 TBq of ^{13}N were produced in 2017. Unfortunately, we did not receive any data for operations conducted before 2005.

2.2. Estimation of the activation of the magnet coils by simulation

The activation of the coils is caused by the secondary neutrons produced by the interactions of the beam protons with components of the accelerator within the vacuum chamber. Two mechanisms for the production of secondary neutrons can be distinguished.

The first mechanism corresponds to the interactions of the nominal beam with materials on its trajectory, *i.e.* the stripper foils composed of few microns of carbon (Braccini, 2016) and the target ports. Each target port includes the collimator, the vacuum window, the target window and the target material, which is used to produce the radioisotopes of interest.

The second mechanism corresponds to "unwanted" beam losses. One reason for this is due to the dissociation of H$^-$ ions by the residual gas inside the vacuum chamber (Papash and Alenitsky, 2008). The resulting H atoms are no longer guided by the magnetic field. They will continue tangentially from the point of ionization until they hit a material - most likely the vacuum chamber. The losses are in the order of 50% of the accelerated beam (Papash and Alenitsky, 2008). Other beam losses except from ionization are not taken into account here.

Two analysis steps are needed to determine the three-dimensional distribution of activation produced inside the coils:

1. Estimation of the fluence of the secondary neutrons inside the coils with the help of the Monte Carlo tool FLUKA version 3.0 (Böhlen et al., 2014; Ferrari et al., 2005).

2. Estimation of the activation products and their activities with the help of the software tools ActiWiz version 1.3.168 (Vincke and Theis, 2018) and RAW version 4.1.2 (Geyer et al., 2019).

2.2.1. Estimation of the fluence of secondary neutrons

The present study seeks to evaluate the fluence of secondary neutrons inside the coils by implementing a simplified geometrical model of the cyclotron in FLUKA. FLUKA is a Monte Carlo simulation package for the interaction and transport of particles and nuclei in matter. It is widely used in the environment of accelerators.

As a first working hypothesis, we assumed that only interactions of the nominal beam particles with the eight target ports had to be taken

Table 2
Characteristics of the different target types (IBA, 2009).

Isotope produced	Chemical form	Target reaction	Target material	Vacuum window	Target window
^{11}C	CO_2	^{14}N (p,α)^{11}C	N_2+ 0.5–1% O_2	12 µm Titanium	500 µm Aluminium
^{13}N	NH_3	^{16}O (p,α)^{13}N	H_2O (natural) +5 mMol Ethanol	12 µm Titanium	25 µm Havar®
^{15}O	O_2	^{14}N(d, n)^{15}O	N_2+ 0.5% O_2	12 µm Titanium	50 µm Havar®
^{18}F	F$^-$	^{18}O(p, n)^{18}F	$H_2^{18}O$ (98%)	12 µm Titanium	50 µm Havar®

Table 3
Characteristics of the coils (given for one coil).

Inner diameter (cm)	Outer diameter (cm)	Height (cm)	Material	Weight (kg)
120	152.8	22	Copper, Epoxy	1218

into account as sources for secondary neutrons (target material plus windows). Each of these ports can be considered as individual "point-like" sources of secondary neutrons. Two types of target assemblies can be distinguished: those using liquid target materials, like for the production of ^{18}F and ^{13}N, and those using gaseous target materials, like for the production of ^{11}C. The related schematics, as modelled in FLUKA, are shown in Fig. 2 and Fig. 3, respectively. The two target assemblies vary significantly by their geometry and the materials being used.

The 18 MeV proton beam was assumed to be pencil like. The interaction of the beam with the collimators was not taken into account because no detailed information on the beam emittance was available at these locations.

As described above, beam losses during acceleration are expected as an additional source for secondary neutrons. A simplified model for the beam loss mechanism was implemented in FLUKA for the calculation of the related neutron fluence. It is assumed here that 50% of the accelerated H$^-$ beam particles are ionized by the residual gas inside the vacuum system. The stripping process in our simulation is uniformly distributed over the region of acceleration. The resulting H-atoms (ionization of H$^-$) will tangentially continue their trajectories with a momentum $p = qBr$, where r is the radius of the trajectory at the stripping location, q the elementary charge and B the magnetic field. They will interact with the vacuum chamber, where neutrons are produced. Although the acceleration and stripping process was not simulated in detail, this simplified model reproduces the correct interaction rate of lost beam particles with the vacuum chamber. However, the real spatial distribution of the ionization processes could be different. Consequently, the energy spectrum of interacting particles may therefore deviate from what is assumed here as a first approximation. The properties of the target ports T1-T8 as secondary neutron sources are summarized in Table 4. The beam losses (BL) were added also to this list. For each of the nine sources, independent simulations were carried out in FLUKA taking into account the full geometry of the cyclotron.

A cylindrical coordinate system was defined for the scoring of the differential neutron fluence $\Phi_i^s(E)$ from the sources s inside the sub volumes V_i of the magnetic coils as a function of the energy E in 260 bins (see Fig. 4). A scoring volume V_i can be identified by its coordinate (r, ϕ, z). In order to calculate the 3D-distribution, the volume of the coils was subdivided into 216 sub volumes with 24 different values in ϕ and 3 different values in both r and z. For simplicity reasons, the pairs of discrete coordinates (r, z) were combined to positions P, as illustrated in Fig. 4. For each of the volumes V_i, $\Phi_i^s(E)$ originating from each of the sources s was recorded by FLUKA. The scoring volumes have sizes equivalent to 4–7 kg of copper. The azimuthal coordinate $\phi = 0$ is defined by the centre of target T1. FLUKA also provides the statistical uncertainties of these calculations.

2.2.2. Estimation of the activation products and their activities

We calculated the activation products within the volumes V_i inside the magnet coils and their associated activities using ActiWiz 3.3, a software tool developed at CERN. The software makes it possible to quickly determine production rates and then calculate the activities of elementary or composite materials by using radiation fields with complex irradiation patterns. This two steps calculation is done analytically. An irradiation pattern is defined here as a sequence of consecutive periods of constant beam currents with periods without beam between (if required) and a cooling down period at the end. Thus, realistic irradiation scenarios with production cycles and variable beam currents can be
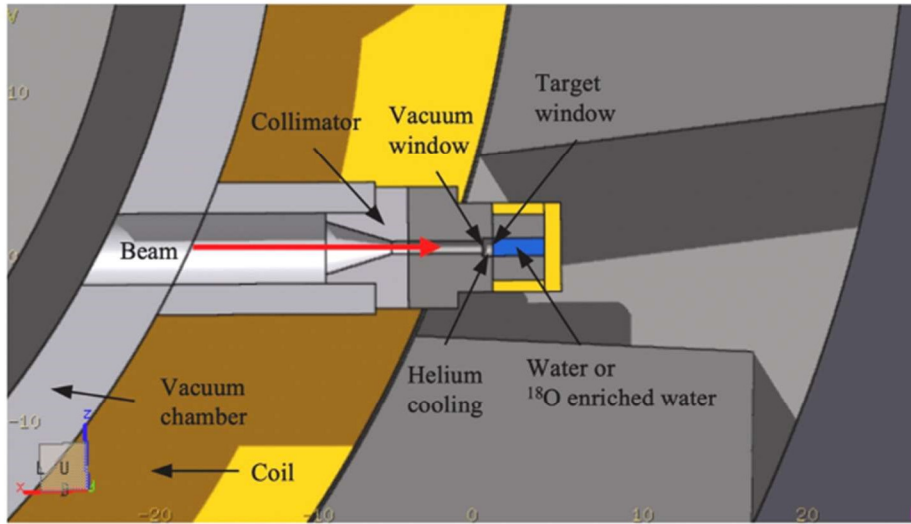
Fig. 2. Target assembly for the production of ^{18}F or ^{13}N. (For interpretation of the references to color in this figure legend, the reader is referred to the Web version of this article.)
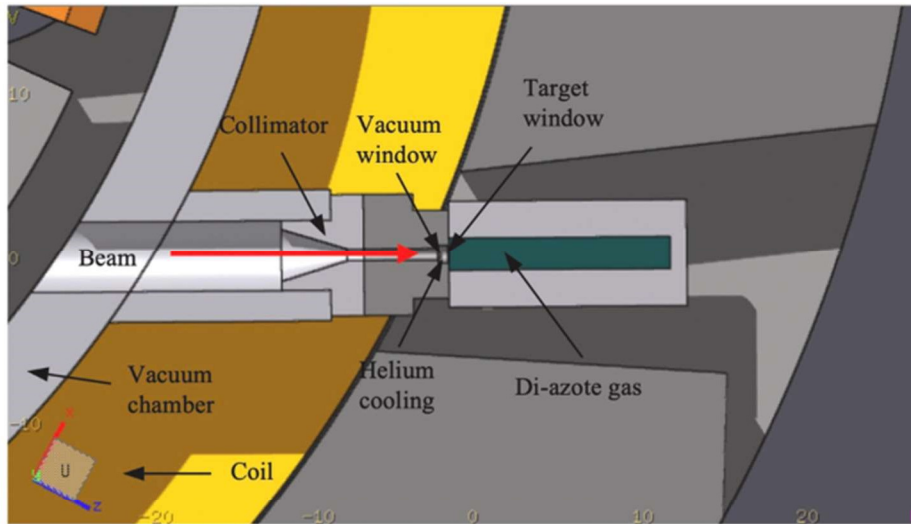
Fig. 3. Target assembly for the production of ^{11}C. (For interpretation of the references to color in this figure legend, the reader is referred to the Web version of this article.)

Table 4
List of neutron sources taken into account for the simulation.

Source	Isotope	Target material used in FLUKA	Total protons
T1	^{18}F	$H_2^{18}O$	1.83×10^{21}
T2	^{18}F	$H_2^{18}O$	8.29×10^{20}
T3	Not used	–	0
T4	^{11}C	N_2 gas at 20 bars	8.09×10^{19}
T5	^{18}F	$H_2^{18}O$	9.81×10^{19}
T6	^{18}F	$H_2^{18}O$	7.99×10^{20}
T7	^{13}N	H_2O	1.16×10^{20}
T8	Not used	–	0
BL	–	Vacuum Chamber	3.75×10^{21}

described. As an example, the irradiation pattern of target T1, as it was assumed for the calculation of the activation of the coils is given in Fig. 5. For a given volume V_i and a differential neutron fluence $\Phi_i^s(E)$ from the source s, the ActiWiz calculations will return a list of the activated nuclides $\{n_{i,j}^s\}$ with $j \, \varepsilon \, [1, m_i^s]$ together with their corresponding specific activities $a_{i,j}^s$ and uncertainties $\Delta a_{i,j}^s$. m_i^s is the number

of nuclides produced in the volume V_i by the source s. The result can be grouped together into activation tuples N_i^s containing m_i^s triplets with the information about the produced nuclides, their activities and uncertainties.

$$N_i^s = \left\{ \left(n_{i,1}^s, a_{i,1}^s, \Delta a_{i,1}^s \right), \ldots, \left(n_j^s, a_{i,j}^s, \Delta a_{i,j}^s \right), \ldots, \left(n_{m_i^s}^s, a_{i,m_i^s}^s, \Delta a_{i,m_i^s}^s \right) \right\} \quad (1)$$

The result for the total specific activities of the nuclides inside the volume V_i is obtained by summing over all sources:

$$N_i = \sum_s N_i^s = \left\{ \left(n_{i,1}, a_{i,1}, \Delta a_{i,1} \right), \ldots, \left(n_{i,k}, a_{i,k}, \Delta a_{i,k} \right), \ldots, \left(n_{i,m_i}, a_{i,m_i}, \Delta a_{i,m_i} \right) \right\}$$

$$(2)$$

, where $\{n_{i,k}\} = \cup_s \{n_{i,j}^s\}$ is the union set of the nuclides produced by the different sources s in the volume V_i with $k \, \varepsilon \, [1, m_i]$ and m_i is the corresponding number of nuclides. The activities and uncertainties simply result from:

$$a_{i,k} = \sum_s a_i^s (n_{i,k}) \quad (3)$$
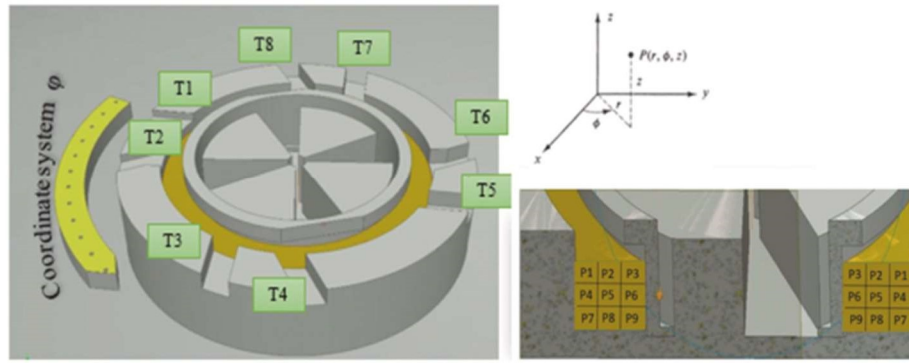
Fig. 4. Schematic view of the cyclotron showing the cylinder coordinates defined for the coils. The positions P1 to P9 are shown on the right. (For interpretation of the references to color in this figure legend, the reader is referred to the Web version of this article.)

Fig. 5. Blue curve: beam current as a function of time. Red curve: average beam current per time interval (period). The period was set to one year for the years 2004–2014 and to one month for the year 2015. (For interpretation of the references to color in this figure legend, the reader is referred to the Web version of this article.)
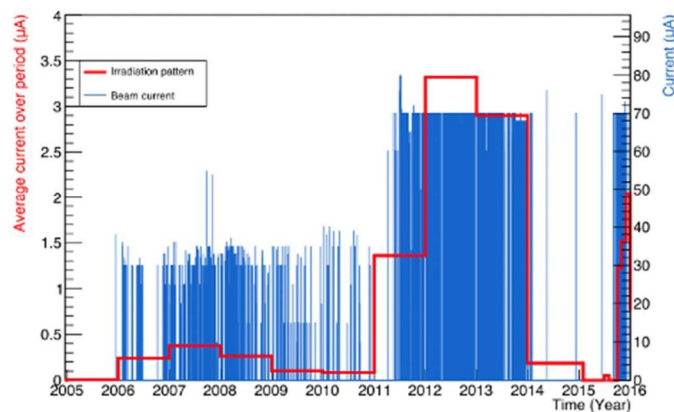
$$\Delta a_{i,k} = \sqrt{\sum_s \left(\Delta a_i^s(n_{i,k}) \right)^2} \qquad (4)$$

The functions $a_i^s(n_{i,k})$ and $\Delta a_i^s(n_{i,k})$ return the activity and uncertainty of a nuclide $n_{i,k}$ from N_i^s.

In order to facilitate the calculations, the software tool RAW was used, which permits to determine N_i in an automated way. In this study, both ActiWiz and RAW were applied for the first time for a low energy medical accelerator.

In summary, $\Phi_i^s(E)$ are calculated with FLUKA, N_i^s are calculated in an automated way with RAW using ActiWiz, and finally N_i are calculated with RAW according to equation (2). RAW takes care of the handling of the input, intermediate and final data (fluence spectra, irradiation profiles and nuclide vectors) in a database. More information about RAW can be found in (Geyer et al., 2019).

2.3. Sampling and measurements of the coils

After removal from the cyclotron, the activated coils were placed in a secured waste storage area. Here, the distribution of count rates at the surface of the coils was measured with a bismuth germinate oxide detector (FHZ-512, Thermo Fisher). The measurements were taken every 7.5° in position P1 with a measurement time of 10 s each. The measurements were carried out at contact of the coils. The goal here is to make a qualitative comparison of the count rates at different locations. The resulting distribution indicates a strongly heterogeneous distribution of the activities inside the coils and shows two maxima around

0° close to T1 and T2 and around 200° close to T5 and T6. The corresponding azimuthal distribution is shown in Fig. 6. Due to the qualitative nature of this study, uncertainties are not discussed here. The background varied strongly with the position of measurement and originated to some extend from the coils themselves. A background correction has therefore not been applied.

Guided by this result, a set of 58 copper samples were extracted from the coil at different locations in ϕ for the positions P1, P3, P7 and P9. The weights of the samples were in the range of 10–20 g each. The locations of the samples on the coil were determined with a precision of 1–2 cm. The samples were measured with a high purity germanium detector (HPGe). The measurement time was 1 h for all the samples with a dead time between 0.03% and 0.63%.

All samples showed a clear signal of the two gamma lines (1173 keV and 1332 keV) of ^{60}Co in the spectrum. In addition, ^{110m}Ag was identified in three samples. Most likely, the second signal comes from silver being an impurity in copper. A neutron activation analysis (NAA) estimated the weight fraction of silver in the copper coils to be 2.2×10^{-4}. In addition to the statistical uncertainties, the systematic uncertainties of the spectroscopy results were estimated as 15%. The precision is limited by the geometrical model for the calculation of the detection efficiencies. The detection efficiencies were estimated with the help of LabSOCS, a calibration software from Mirion Technologies, Inc. (MIRION, 2017). The drilling chips of the samples have been collected in plastic bags. The bags have been measured in a distance of a few millimetres to the detector, in order to get a low MDA (minimum detectable activity) in a reasonable measurement time. The samples were described as simplified rectangular boxes as an approximation of the bags filled with these chips. Cascade summing corrections were applied for ^{60}Co.

3. Results

We characterised the magnet coils of the cyclotron by applying the materials and methods described above. Our first step involved studying the properties of the target assemblies as sources for secondary neutrons. The results are summarized below. We then discuss the activation process of the hotspot of the coils close to T1 based on the simulation results and we give the azimuthal distribution of the relevant activation products for the position P1. Next, we compare the simulation results to those of spectrometry measurements and follow with a discussion of uncertainties. Finally, we present the results of the characterisation of the coils for all 216 scoring volumes defined above. Unless otherwise stated, in the following we provide the uncertainties for one standard deviation.

3.1. Characterisation of the target assembly components as neutron sources

Using FLUKA, we first studied the number of emitted neutrons as a function of energy by the components, which are hit by the full beam
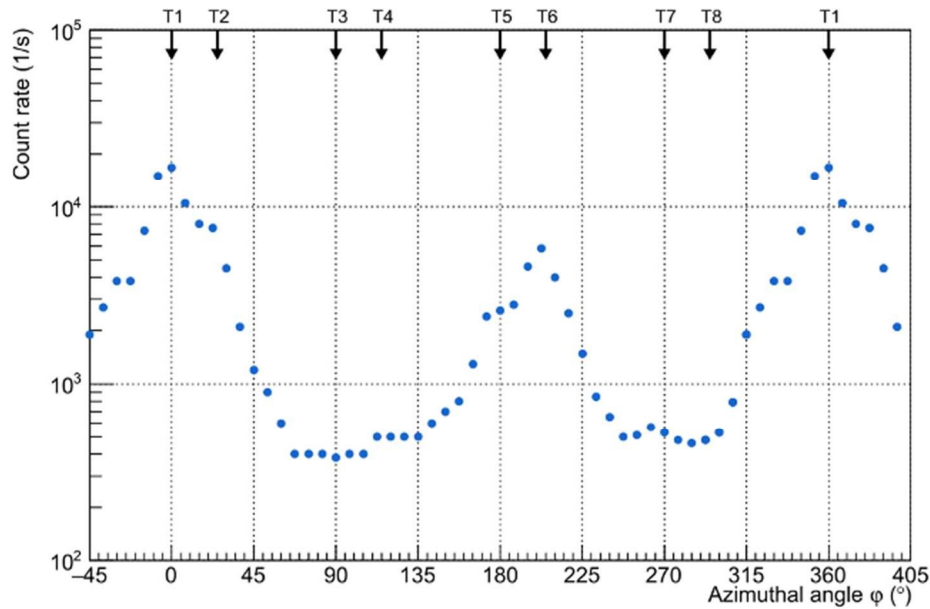
Fig. 6. Azimuthal distribution of the BGO count rates measured at position P1. T1-T8 denotes for the target positions. The hotspot of the coils is at zero degrees next to the target T1. In order to illustrate the distribution around the hotspot, the distribution has been cyclically expanded below 0 and above 360°.

intensity. These are the three different production-materials ($H_2^{18}O$, H_2O and N_2) used for the production of ^{18}F, ^{13}N and ^{11}C, the target windows, the vacuum windows and the stripper foils. The simulations assume an 18 MeV pencil like proton beam. The individual components listed above are simulated with their real dimensions. Other components of the target assembly or cyclotron were omitted from the simulation in order to avoid secondary processes. The results are shown in Fig. 7. The strongest emitter of neutrons is the material for the ^{18}F production. The neutrons mainly come from the reaction $^{18}O(p,n)^{18}F$. The target material for ^{11}C produces around ten times less neutrons, followed by the target and vacuum windows. The target material for the production of ^{13}N creates one thousand times less neutrons compared to the target material for ^{18}F production over the entire energy range. The production of neutrons in that target assembly is dominated by the windows. Thermal neutrons are not necessarily produced by the primary

interactions of the proton beam. Like in the example of the target material $H_2^{18}O$ for the production of ^{18}F, they are generated by secondary interactions of neutrons within the production material.

The yield of secondary neutrons can then be classified from highest to lowest as follows:

1. $H_2^{18}O$ for the production of ^{18}F;
2. N_2 for the production of ^{11}C;
3. The target window of the ^{11}C target assembly (500 μm Al);
4. The target window of the ^{18}F target assembly (50 μm Havar);
5. The target window of the ^{13}N target assembly (25 μm Havar);
6. The vacuum window (12.5 μm Ti);
7. H_2O for the production of ^{13}N;
8. The stripper foils (5 μm C).
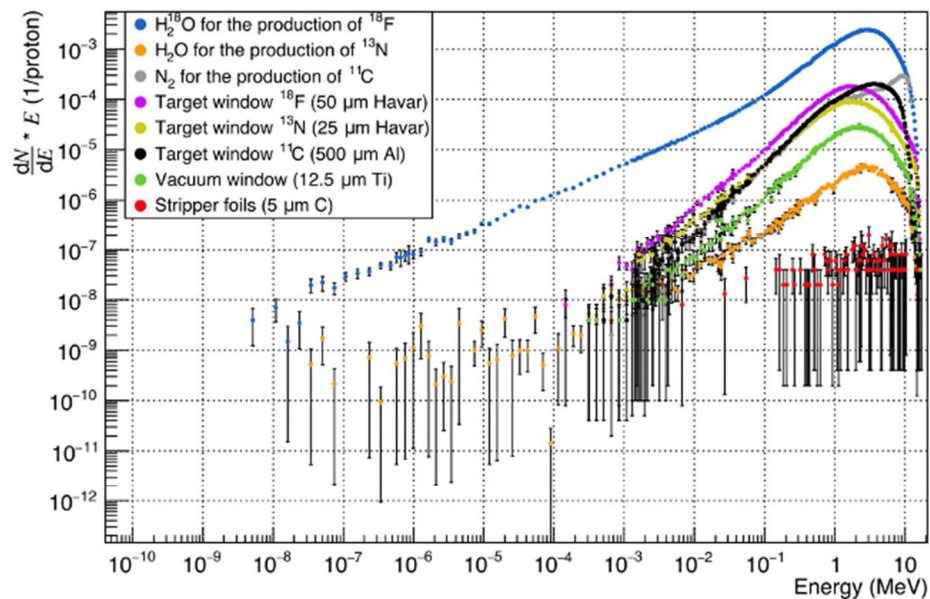
Fig. 7. Neutron energy spectra per primary proton emitted by the different components. The error bars represent the statistical uncertainties of the FLUKA calculations. (For interpretation of the references to color in this figure legend, the reader is referred to the Web version of this article.)

6

46

In order to crosscheck the correctness of the FLUKA calculations, we compared the production yields for ^{18}F, ^{13}N and ^{11}C with values from the IAEA database for medical radioisotope production (IAEA, 2018). The results are given in Table 5. The values agree within a few percent for ^{18}F and the ratio FLUKA/IAEA is compatible with the results from the study of (Infantino et al., 2015). Larger deviations were observed for ^{13}N and ^{11}C. This gives a first idea on the uncertainties of the FLUKA calculations.

3.2. Characterisation of the hotspot of the coils by simulation

As already mentioned, the hotspot of the coil is next to the target T1, the target assembly for the ^{18}F production with the highest integrated beam current. The corresponding scoring volume for the FLUKA calculations is denoted by V_1 (see also 2.2.1) and has the coordinates ($\phi = 0$, $P = P1$). Fig. 8 shows the differential neutron fluence $\Phi_1^s(E)$ at this location for the different neutron sources s. Obviously, the main contribution comes from target T1, which is the closest.

The nuclide content N_1 of the hotspot V_1 was then calculated using Equation (2) with the appropriate irradiation profiles and differential neutron fluence spectra as input for ActiWiz. We assumed that the coils are made from pure copper with an impurity of 0.022% silver. The results are given in Table 6 for cooling times after irradiation of 1 day and 2.5 years, respectively. The statistical uncertainties of the ActiWiz calculations were below 1% for all the radionuclides.

Following the example above, we then determined the nuclide contents N_i for all the 216 sub volumes V_i, where the differential neutron fluence was recorded as described in section 2.2.1. In Fig. 9, the specific activities caused by the neutron fluence from target T1 are compared with the total specific activities obtained by Equation (2) as a function of ϕ. The results are given for the position P1 for a cooling time of 2.5 years. The only radiologically relevant radionuclides were ^{60}Co, ^{63}Ni and ^{110m}Ag.

The specific activities of ^{63}Ni vary between 0.5 Bq/g and 100 Bq/g and those of ^{60}Co between 0.1 Bq/g and 20 Bq/g. The specific activities of ^{110m}Ag, which were omitted from the plot for clarity reasons, are in the range of 5.10^{-3} Bq/g and 0.2 Bq/g. The activation distributions are strongly modulated by the targets. As can be seen in Fig. 9, the activation of the coil close to target T1 is dominated by this target. In larger distances, the contribution of other targets becomes clearly relevant. They must be taken into account following Equation (2).

3.3. 3-D distribution of activation and comparison with measurements

To compare the measured results with the simulations, we defined scoring volumes at 144 different equidistant azimuth angles ϕ and at four different positions (P1, P3, P7 and P9). The sizes of the scoring volumes were around 10 cm^3 and were comparable to those of the spectroscopy samples. We compared the measurements with the simulation for a cooling time of 2.5 years. This time corresponds to the moment when the characterisation started.

The expectations for the specific activity of ^{60}Co from the simulation are shown in Fig. 10. The summed contributions from the targets T1 - T8 are plotted separately from those from beam losses BL inside the machine. As already mentioned, we assumed 50% losses during acceleration, a typical value quoted for this type of accelerator (Papash and

Alenitsky, 2008). The plot clearly shows that the activation of the coils is dominated by the production targets. Beam losses contributed only in parts of lowest activation of the coils. Fig. 10 also shows the spectroscopy results of the material samples. The measured specific activities inside the coils varied by more than four orders of magnitudes between 0.03 Bq/g and 100 Bq/g. A first comparison between measurements and simulation shows that the latter systematically underestimates the activation of the coils by about a factor 2.5. This underestimation seems to be uniform and relatively independent of the position inside the coils in both ϕ and P. In order to improve the precision of the simulation predictions, we then multiplied the beam currents used for the irradiation profiles by a correction factor of 2.5.

After normalisation by this factor, the simulation showed a good agreement with measurements, as can be seen in Fig. 11. Fig. 12 shows the distribution of $(a^{meas} - a^{sim})/a^{sim}$. Under the assumption that the uncertainties of the spectrometry measurements are small compared to those of the simulation, this distribution directly reflects the (experimentally determined) uncertainties of the simulation results, including those listed in Table 7. The 58 samples, which were used for the comparison, cover a large part of the surface of the coils. Based on this histogram, the uncertainties on the activity of ^{60}Co were estimated to [-60% + 100%] at a confidence level of 95% over the full volume of the coils. For the characterisation of the coils, which is described in the next section, we assumed the same uncertainty for the radionuclides ^{63}Ni and ^{110m}Ag.

In order to explain the correction factor, we conducted several systematic studies for the hotspot. As shown in section 3.1, the production of ^{18}F is correctly described by the simulation. This reaction channel ^{18}O (p,n)^{18}F was the main source of secondary neutrons next to the hotspot. Although the total production seems to be right, the anisotropy of emitted neutrons could still be different between simulation and reality. The activation of the hotspot is dominated by neutrons emitted in backward direction of the target cell. In a publication from (Hagiwara et al., 2011), the experimental data on the energy spectra and angular distributions for neutrons is compared with Monte-Carlo calculations (MCNPX (Pelowitz, 2011) and PHITS (Sato et al., 2018)) for proton energies of 18 MeV. Significant discrepancies have been observed between experimental data and simulation results, depending on the neutron energy and emission angle. A very recent article (Bakhtiari et al., 2020) compares the same experimental data with FLUKA simulations. According to their results, the emission of neutrons in backward direction (150°) is underestimated by a factor of two or more in the energy range between 6 and 11 MeV by the simulation. This range is absolutely relevant for the production of ^{60}Co in copper. It could explain at least a part of the correction factor.

Beside the targets, also the collimators may be hit by the beam. Twenty percent of the beam interactions inside the collimator of the target T1 would contribute only to an additional three percent in activity of ^{60}Co. The uncertainties of other sources are summarized in Table 7.

For the calculation of the activation of the copper of the coils, we assumed the average density of 7.87 g/cm^3 of the material, while the density of pure copper is 8.94 g/cm^3. The difference comes mainly from epoxide and a cooling flask inside the coils. These materials were not explicitly included in our geometrical description in FLUKA. The necessary technical details were not available. In order to estimate an impact of different density assumptions on the activation in the surrounding of the hotspot, we compared the simulation results for ^{60}Co for both densities. They differ by 10% and cannot explain the necessary correction factor here.

The position of the target assembly T1 relative to the coils is known with a precision of about 1 cm. When varying this position in the simulation by that quantity, the ^{60}Co activity changed by 10% for the hotspot and even less for locations further away from T1.

The coordinates of the samples have an uncertainty of 1–2 cm. Because of the large gradients of the activity distribution, this had the biggest impact on the uncertainties, which may become 40% in certain

Table 5
Comparison of the activities expected by FLUKA with those expected by IAEA. The activities are given after 1 h of irradiation with a beam current of 1 µA.

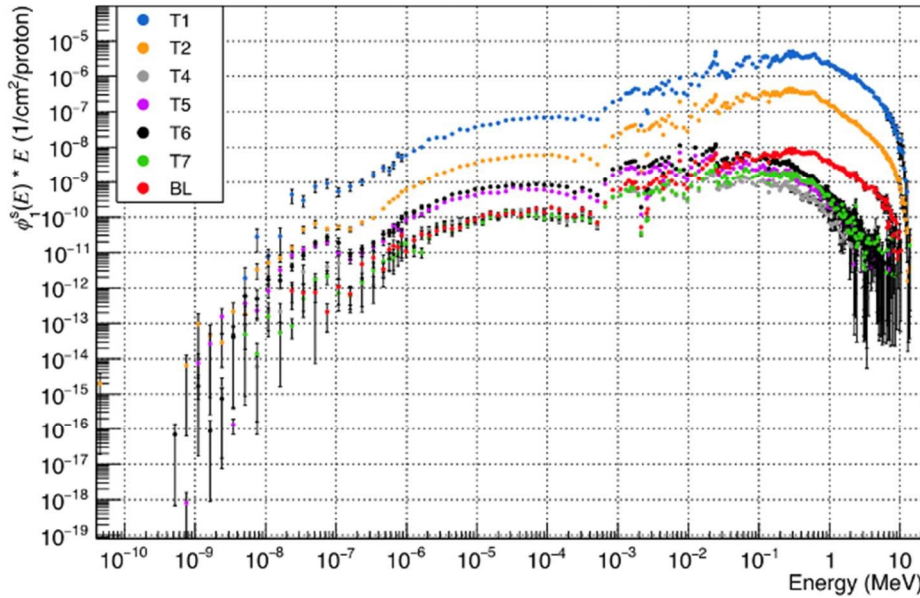| Radionuclides	Activity FLUKA (GBq)	Activity IAEA (GBq)	FLUKA/IAEA
^{18}F	4.15	4.29	0.97
^{13}N	1.97	1.64	1.20
^{11}C	7.98	5.51	1.45

Fig. 8. Neutron fluence at the location of the hotspot of the coils. The contributions from each source are shown separately. The error bars represent the statistical uncertainties of the FLUKA calculations. (For interpretation of the references to color in this figure legend, the reader is referred to the Web version of this article.)

Table 6
Radionuclides and corresponding activities for 1 day and 2.5 years of cooling. Only nuclides with specific activities larger 10^{-3} Bq/g are listed.

1 day of cooling		
Isotope	$T_{1/2}$ (y)	a_1 (Bq/g)
^{64}Cu	1.45×10^{-3}	7.1×10^3
^{63}Ni	1.01×10^2	8.5×10^1
^{60}Co	5.27	1.9×10^1
^{110m}Ag	6.84×10^{-1}	2.4
^{110}Ag	7.78×10^{-7}	3.3×10^{-2}
^{65}Ni	2.87×10^{-4}	1.2×10^{-2}
^{108m}Ag	4.18×10^2	8.5×10^{-3}

2.5 years of cooling		
Isotope	$T_{1/2}$ (y)	a_1 (Bq/g)
^{63}Ni	1.01×10^2	8.4×10^1
^{60}Co	5.27	1.4×10^1
^{110m}Ag	6.84×10^{-1}	1.9×10^{-1}
^{108m}Ag	4.18×10^2	8.5×10^{-3}

regions of the coil.

Unfortunately, we have no reliable information about the uncertainties of the beam currents.

^{60}Co is produced inside the coils via the reaction ^{63}Cu(n,α)^{60}Co. Both software tools, FLUKA and ActiWiz, rely on the same cross section data. In order to validate the correctness of the ActiWiz calculations at low energies, a direct comparison between FLUKA and ActiWiz has been made. The comparison is based on the calculation of the activation products inside three volumes V_1, V_4 and V_{17} from source T1. The irradiation pattern from Fig. 5 and a cooling time of 2.5 years were assumed. The results are summarized in Table 8. For ^{60}Co and ^{63}Ni, the results agree within uncertainties. The values for ^{110m}Ag differ significantly between ActiWiz and FLUKA. While the calculation of ActiWiz is based on the ^{109}Ag(n,γ)^{110m}Ag cross section taken from the JEFF-3.1 nuclear data library, FLUKA (version3.0) assumes an arbitrary production rate of 50% relative to all produced ^{110}Ag states.

In general, the uncertainties of ActiWiz are an order of magnitude lower compared to FLUKA. This advantage results from the analytical calculation of the activities from the fluence spectra compared to the pure Monte-Carlo approach in FLUKA.

The operation between 2000 and 2005 was not taken into account in our calculations because no operational data has been available. Assuming working conditions similar to the last years, the ^{60}Co activities would increase by about 15% and the ^{63}Ni about 30%.

An unambiguous explanation for the correction factor is still missing. Further investigations would be necessary. However, what counts for the characterisation is a reasonable agreement between the measurements and the simulation. This was the case after we applied the correction factor.

3.4. Radiological characterisation of the coils

According to Art.106 of the Swiss radiation protection ordinance (ORaP) (The Swiss federal council, 2019), a material is classified as radioactive if one the following criteria is fulfilled:

1. The surface contamination exceeds the surface contamination limits CS.
2. The dose rate after background suppression exceeds 0.1 μSv/h at 10 cm of distance.
3. The specific and absolute activity of the radionuclide exceeds the clearance limits LL.

Contamination is rarely an issue with this type of accelerator. Our study confirmed this by negative wipe tests on the coils. Accordingly, this work focused on determining the activation products within the irradiated material (criterion 3). The values of LL are specified in Annex 3 Column 9 of the ORaP. If a material contains more than one radionuclide, the following summation rule has to be applied for the criterion 3:

$$S_{LL} = \sum_{l=1}^{m} \frac{a_l}{LL_l} \qquad (5)$$

Here, a_l denotes the specific activity and LL_l denotes the clearance limits for each radionuclide l.

In case of homogenisation of the coil by melting, equation (5) becomes:

$$S_{LL,h} = \sum_{l=1}^{m} \frac{\bar{a}_l}{LL_l} = \sum_{l=1}^{m} \frac{A_l/M}{LL_l} \qquad (6)$$
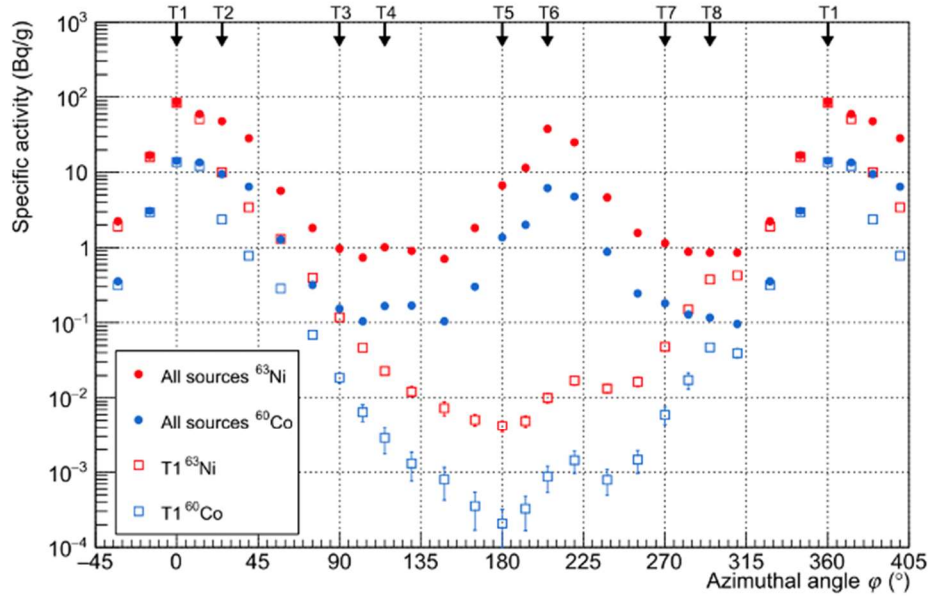
Fig. 9. Azimuthal distribution of the specific activities of ^{60}Co and ^{63}Ni for position P1 for a cooling time of 2.5 years. The error bars represent the statistical uncertainties of the ActiWiz calculations. (For interpretation of the references to color in this figure legend, the reader is referred to the Web version of this article.)
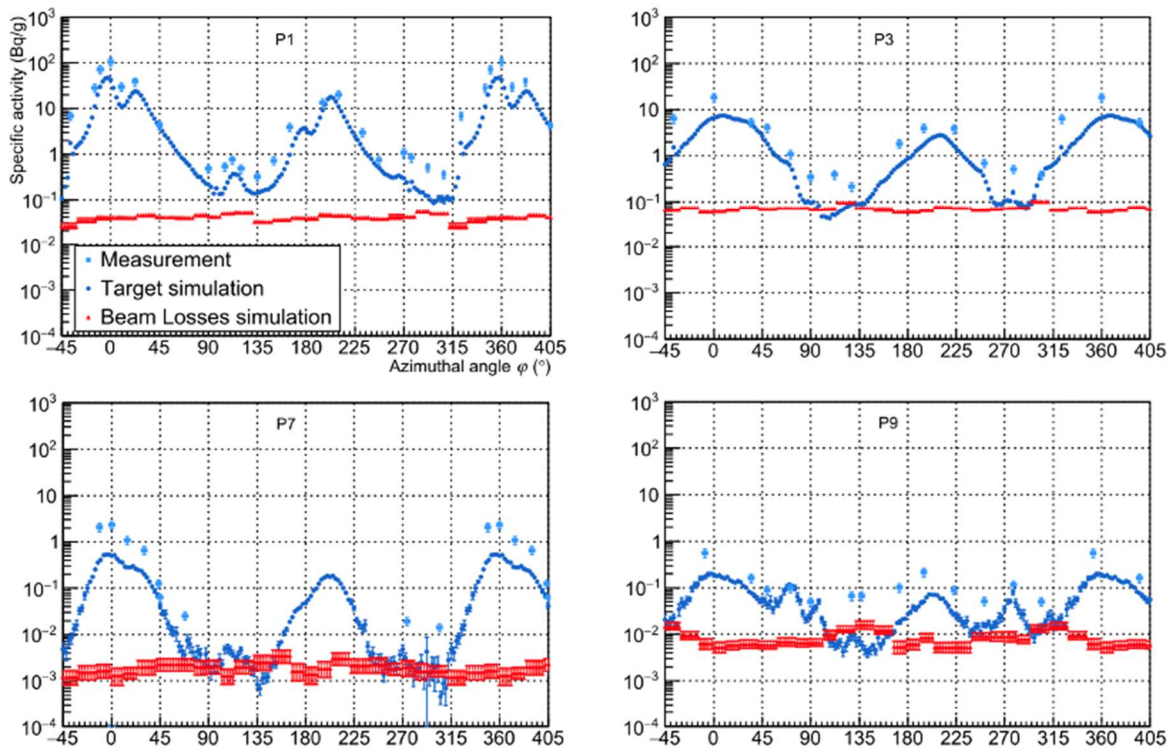
Fig. 10. Azimuthal distribution of the specific activities of ^{60}Co for the positions P1, P3, P7, and P9. Simulation results are compared to measurements. The contributions from targets and beam losses are plotted separately for the simulation. (For interpretation of the references to color in this figure legend, the reader is referred to the Web version of this article.)

, where $\bar{a}_l$ are the specific activities of the activation products after homogenisation and A_l are the absolute activities and M the total mass of the coils.

The list of radionuclides $\{n_l\}$ with $l \varepsilon [1, m]$, which have been produced inside the coils, can simply be extracted from the activation tuple N_i (see also equation (2)) as the union set of nuclides from each volume $V_i : \{n_l\} = \cup_i \{n_{i,k}\}$. The total activity A_l is then calculated with the equation:

$$A_l = \sum_{i=1}^{216} a_i(n_l)^* \, w_i \qquad (7)$$

, where the function $a_i(n_l)$ extracts the specific activity of the nuclide n_l inside the volume V_i from N_i and w_i denotes the mass of the volume V_i.

In order to determine which part of the copper coils satisfies the clearance criterion, we plotted the three-dimensional distribution of S_{LL},

9
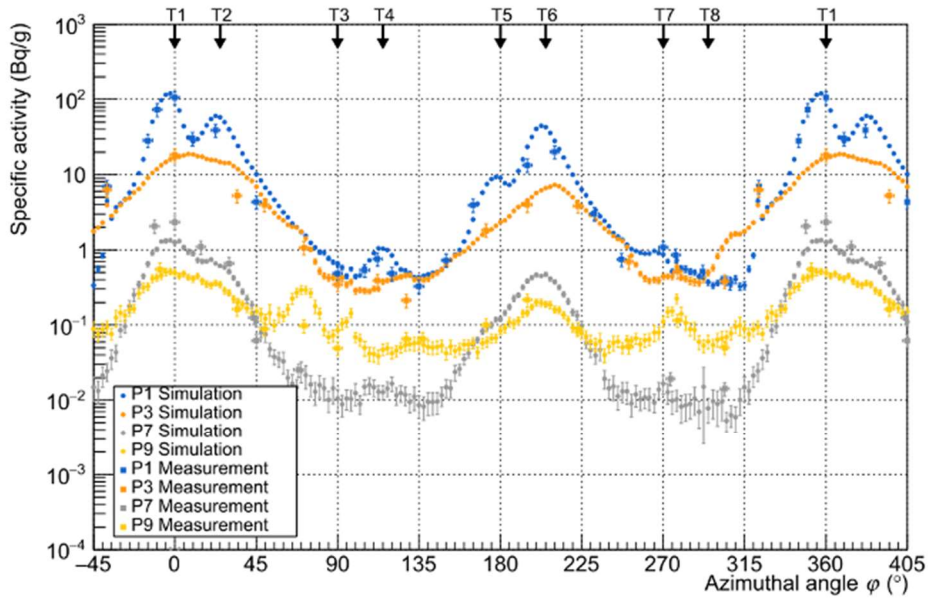
Fig. 11. Simulated azimuthal distribution of the specific activities of ^{60}Co after normalisation in comparison with measurements. (For interpretation of the references to color in this figure legend, the reader is referred to the Web version of this article.)
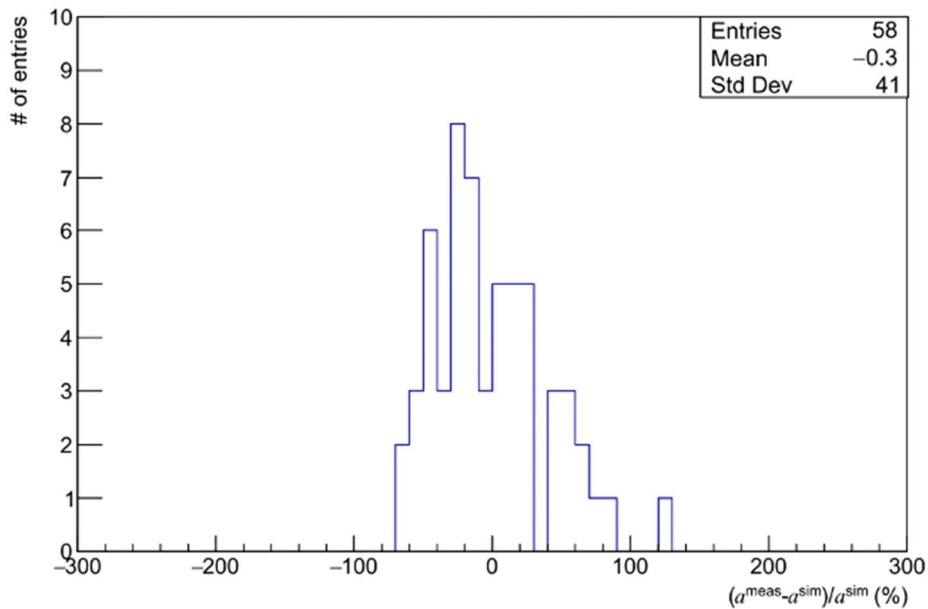
Fig. 12. Distribution of $(a^{meas} - a^{sim})/a^{sim}$ for ^{60}Co after normalisation.

Table 7

Sources of uncertainties for the simulated and measured activities of ^{60}Co.

Source	Uncertainty (max)
Spectrometry	15%
Magnet density FLUKA	10%
Position of the target assemblies relative to the coils	10%
Coordinates of samples	40%

as calculated from N_i (see Equation (2)) after normalisation, for a cooling time of two and a half years in Fig. 13. In Switzerland, a cooling time of 30 years is required if the material can be cleared afterwards (see Art.117 of the ORaP). The result for a cooling time of 30 years is given in Fig. 14. The size of the volumes used for these calculations corresponds to those defined in section 2.2.1. After two and a half years of cooling,

72^{+18}_{-20} % of the coil volume is considered radioactive in terms of $S_{LL} > 1$ (Fig. 13).

If the activity distribution of the coils were homogenised by melting, the activity of the copper would result to $S_{LL,h} = 20^{+9}_{-6}$. The material could therefore not be cleared.

After 30 years of cooling, only 15^{+8}_{-11}% of the volumes are still considered radioactive and 85^{+11}_{-8}% of the volumes could be released. After homogenisation, $S_{LL,h}$ would decrease approximately to $S_{LL} = 0.6^{+0.3}_{-0.2}$. In that case, the entire material could be recycled.

Here, the values of S_{LL} are given at a confidence level of 95%. The uncertainties defined in the previous section were quadratically propagated. The uncertainties of the spectroscopy measurements were taken into account.

The total activities A, the mean specific activities $\bar{a}$ and $S_{LL,h}$ after homogenisation are summarized in Table 9 for the relevant

10

50

Table 8

Comparison of specific activities calculated by FLUKA and ActiWiz for the irradiation pattern shown in Fig. 5 and a cooling time of 2.5 years (the uncertainties are given for one standard deviation).

Volume	Radionuclide	Activity (Bq/g) FLUKA	Activity (Bq/g) ActiWiz
V_1	^{60}Co	$3.69 \times 10^1 \pm 6.35$	$4.09 \times 10^1 \pm 3.2 \times 10^{-1}$
	^{63}Ni	$1.65 \times 10^2 \pm 3.30$	$1.63 \times 10^2 \pm 3.6 \times 10^{-1}$
	^{110m}Ag	$1.45 \pm 3.12 \times 10^{-1}$	$5.78 \times 10^{-2} \pm 2.05 \times 10^{-3}$
V_4	^{60}Co	$1 \times 10^1 \pm 3.07$	$9.04 \pm 1.42 \times 10^{-1}$
	^{63}Ni	$3.87 \times 10^1 \pm 1.78$	$3.71 \times 10^1 \pm 1.5 \times 10^{-1}$
	^{110m}Ag	$1.36 \pm 2.89 \times 10^{-1}$	$3.99 \times 10^{-2} \pm 1.66 \times 10^{-3}$
V_{17}	^{60}Co	1.63 ± 1.12	$1.22 \pm 5.64 \times 10^{-2}$
	^{63}Ni	$3.97 \pm 6.04 \times 10^{-1}$	$4.64 \pm 5.9 \times 10^{-2}$
	^{110m}Ag	$2.82 \times 10^{-1} \pm 1.22 \times 10^{-1}$	$1.41 \times 10^{-2} \pm 1.02 \times 10^{-3}$

radionuclides and for cooling times of 2.5 years and 30 years.

These results can be used by the local radiation protection officer and the authorities to identify the appropriate waste management procedure for the coils.

4. Conclusion

We radiologically characterised a major component (here the magnet coils) of a biomedical cyclotron by determining the three-dimensional distribution of activities of all relevant activation products. In order to obtain a complete picture of these distributions, we combined the results of γ-ray measurements of material samples of the coils with the expectations from a Monte-Carlo simulation. FLUKA, ActiWiz and RAW were used for the simulation calculations. The latter two are new software tools developed at CERN. They were used here for the first time in a medical environment for low energy accelerators in the range of MeV. These tools were essential in that they enabled us to obtain detailed results with reasonable computing time and in an efficient way. ActiWiz calculates the activities of activation products analytically, which helps to keep the uncertainties small compared to a pure Monte-Carlo approach like FLUKA. In addition, ActiWiz uses the corresponding production cross-section for ^{110m}Ag, which is another advantage when compared with FLUKA (version 3.0). We then used the spectroscopy measurements of samples to identify the relevant sources

of secondary neutrons and to validate the assumptions made by the simulation model. This study determined that the strongest sources of secondary neutrons are the production targets for ^{18}F. Nevertheless, in regions with low activation of the coils, we were able to determine the contributions from other sources, like beam losses or target windows, in order to make a complete description of the activity distributions by the model.

It was necessary to apply a correction factor on the simulation data to obtain a good agreement between simulation and measurements results. This factor seems to be uniform and relatively independent of the location inside the coils. Once applied, both measurement and simulation results showed a good agreement considering that the activities vary by more than four orders of magnitude within the coils. Presently, the reasons for the required correction are not fully understood. They should be further investigated. In a recent article (Bakhtiari et al., 2020), a comparison of the FLUKA results for the angular distribution of emitted neutrons from the ^{18}O(p,n)^{18}F reaction with experimental data suggests that the neutron fluence inside the coils by our simulation could be underestimated. If confirmed, an improvement of the underlying simulation models would of course be desirable.

We assumed that the coils are made from pure copper with some silver as impurity. Because of the high purity of the material (>99.96%) and our observations, we presently have no evidence for additional relevant impurities. Nevertheless, a detailed chemical analysis of the copper material would be preferable to remove any doubts.

Our results made it possible to characterise the coils radiologically. After 2.5 years of cooling, the biggest part of the coils must be classified as radioactive. However, after 30 years, more than 85% of the material could be cleared. After homogenisation, all material could be recycled. Based on these results, the local radiation protection officer and the authorities can identify the appropriate way of waste management for the coils.

The methods applied here are well suited for providing similar detailed information about the activity distributions of other components of the accelerator or its environment.

CRediT authorship contribution statement

V. Bonvin: Writing - original draft, Visualization, Methodology, Software, Investigation. **F. Bochud:** Resources, Supervision, Investigation. **J. Damet:** Resources, Project administration, Conceptualization. **C.**

Fig. 13. Azimuthal distribution of S_{LL} after 2.5 years of cooling. Volumes with S_{LL} larger than one count as radioactive (points above the red line). Error bars are given at a confidence level of 95%. (For interpretation of the references to color in this figure legend, the reader is referred to the Web version of this article.)

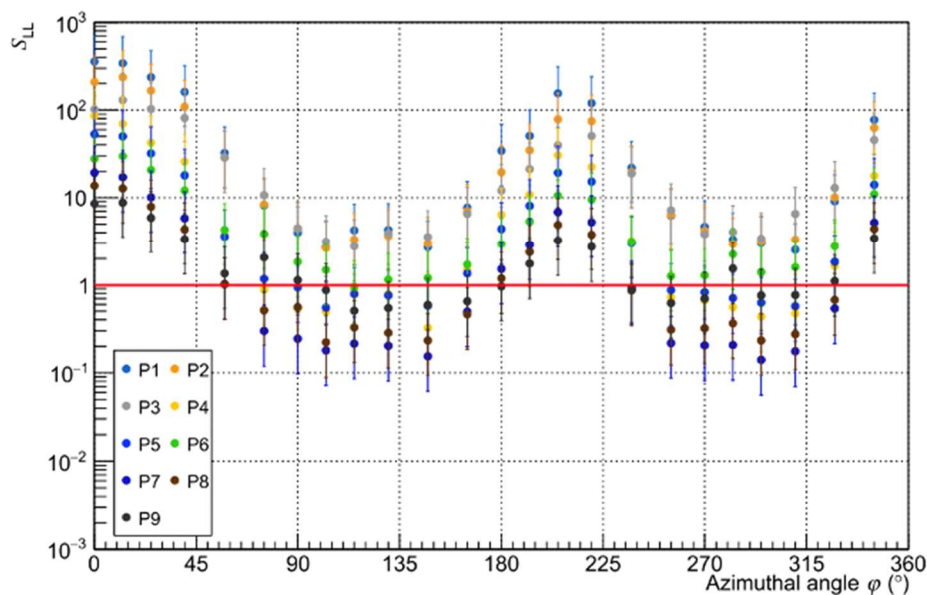**Fig. 14.** Azimuthal distribution of S_{LL} after 30 years of cooling. Volumes with S_{LL} larger than one count as radioactive (points above the red line). Error bars are given at a confidence level of 95%. (For interpretation of the references to color in this figure legend, the reader is referred to the Web version of this article.)
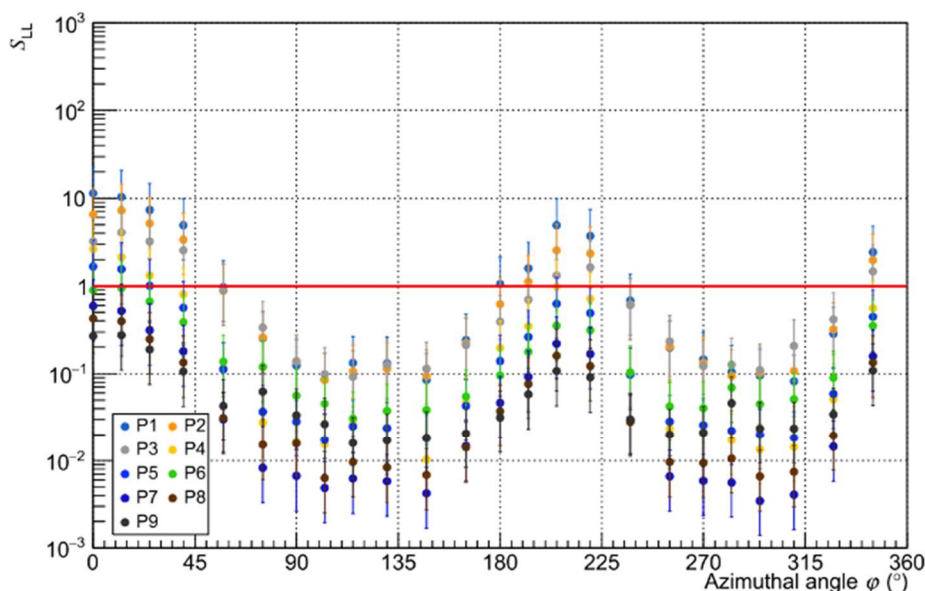
Table 9
Total activities, mean specific activities and summation values after homogenisation for each of the coils.

2.5 years of cooling				
Radionuclides	A (MBq)	$\bar{a}$ (Bq/g)	LL (Bq/g)	$S_{LL,h}$
^{63}Ni	13.4	11.0	100	20^{+9}_{-6}
^{60}Co	2.3	1.9	0.1	
^{110m}Ag	1.5×10^{-2}	1.2×10^{-2}	0.1	

30 years of cooling				
Radionuclides	A (MBq)	$\bar{a}$ (Bq/g)	LL (Bq/g)	$S_{LL,h}$
^{63}Ni	11.1	9.1	100	$0.6^{+0.3}_{-0.2}$
^{60}Co	6.3×10^{-2}	5.1×10^{-2}	0.1	
^{110m}Ag	1.2×10^{-14}	1.0×10^{-14}	0.1	

Declaration of competing interest

The authors declare that they have no known competing financial interests or personal relationships that could have appeared to influence the work reported in this paper.

Acknowledgements

References

Bakhtiari, M., Mokhtari Oranj, L., Jung, N.-S., Lee, A., Lee, H.-S., 2020. Estimation of neutron production yields from H218O as the 18F-production target bombarded by 18-MeV protons. Radiat. Phys. Chem. 177, 109120. https://doi.org/10.1016/j.radphyschem.2020.109120.

Böhlen, T.T., Cerutti, F., Chin, M.P.W., Fassò, A., Ferrari, A., Ortega, P.G., Mairani, A., Sala, P.R., Smirnov, G., Vlachoudis, V., 2014. The FLUKA code: developments and challenges for high energy and medical applications. Nucl. Data Sheets 120, 211–214. https://doi.org/10.1016/j.nds.2014.07.049.

Braccini, S., 2016. Compact medical cyclotrons and their use for radioisotope production and multi-disciplinary research. In: Proceedings of Cyclotron 2016. Zurich, Switzerland, p. 232.

Calandrino, R., del Vecchio, A., Savi, A., Todde, S., Griffoni, V., Brambilla, S., Parisi, R., Simone, G., Fazio, F., 2006. Decommissioning procedures for an 11 MEV self-shielded medical cyclotron after 16 years OF working time. Health Phys. 90, 588–596. https://doi.org/10.1097/01.HP.0000190161.96172.ae.

Eurostat, 2019. Healthcare Resource Statistics - Technical Ressources and Medical Technology. Statistics Explained.

Ferrari, A., Sala, P.R., Fasso, A., Ranft, J., 2005. Fluka : a multi-particle transport code (No. SLAC-R-773, 877507). https://doi.org/10.2172/877507.

Geyer, R., Damet, J., Theis, C., Vincke, H., Sotiropoulou, M., Bonvin, V., 2019. Radiological Characterization of Activated Material at Accelerators. Presented at the IRPA 2018, The Hague, Netherlands, pp. 6–13.

Hagiwara, M., Sanami, T., Masumoto, K., Iwamoto, Y., Matsuda, N., Sakamoto, Y., Nakane, Y., Nakashima, H., Uwamino, Y., 2011. Spectrum measurement of neutrons and gamma-rays from thick H18O target bombarded with 18 MeV protons. J. Kor. Phys. Soc. 59, 2035–2038. https://doi.org/10.3938/jkps.59.2035.

IAEA, 2019. Cyclotrons used for radionuclide production. https://nucleus.iaea.org/sites/accelerators/Pages/Cyclotron.aspx accessed 01 January 2020.

IAEA, 2018. Charged-particle cross section database for medical radioisotopes production. https://www-nds.iaea.org/medical/positron_emitters.html accessed 31 January 2020.

IAEA, 2009. Cyclotron Produced Radionuclides: Principles and Practice Technical.

IAEA, 2003. Decommissioning of Small Medical, Industrial and Research Facilities.

IBA, 2009. Cyclone 18/9.

Infantino, A., Marengo, M., Baschetti, S., Cicoria, G., Longo Vaschetto, V., Lucconi, G., Massucci, P., Vichi, S., Zagni, F., Mostacci, D., 2015. Accurate Monte Carlo modeling of cyclotrons for optimization of shielding and activation calculations in the biomedical field. Radiation Physics and Chemistry, Proceedings of the 9th International Topical Meeting on Industrial Radiation and Radioisotope Measurement Applications 116, 231–236. https://doi.org/10.1016/j.radphyschem.2015.01.001.

MIRION, 2017. LabSOCS calibration software. https://www.mirion.com/products/labsocs-calibration-software accessed 10 September 2020.

NEA, 2013. Radiological Characterisation for Decommissioning of Nuclear Installations (No. NEA/RWM/WPDD(2013)2).

Papash, A.I., Alenitsky, YuG., 2008. On beam intensity upgrade in the commercial cyclotrons of negative hydrogen ions. Phys. Part. Nucl. Lett. 5, 469–472. https://doi.org/10.1134/S1547477108050117.

Pelowitz, D.B., 2011. MCNPX Users Manual Version 2.7.0 (No. LA-CP-11-00438).

Sato, T., Iwamoto, Y., Hashimoto, S., Ogawa, T., Furuta, T., Abe, S., Kai, T., Tsai, P.-E., Matsuda, N., Iwase, H., Shigyo, N., Sihver, L., Niita, K., 2018. Features of particle and heavy ion transport code system (PHITS) version 3.02. J. Nucl. Sci. Technol. 55, 684–690. https://doi.org/10.1080/00223131.2017.1419890.

Sunderland, J.J., Erdahl, C.E., Bender, B.R., Sensoy, L., Watkins, G.L., 2012. Considerations, measurements and logistics associated with low-energy cyclotron decommissioning. Presented at the 14TH INTERNATIONAL WORKSHOP on TARGETRY and TARGET CHEMISTRY. Playa del Carmen, Maxico, pp. 16–20. https://doi.org/10.1063/1.4773931.

The Swiss federal council, 2019. ORaP (Ordonnance sur la radioprotection).

Toyoda, A., Yoshida, G., Matsumura, H., Masumoto, K., Nakabayashi, T., Yagishita, T., Sasaki, H., 2018. Evaluation of induced activity in various components of a PET-cyclotron. J. Phys.: Conf. Ser. 1046 https://doi.org/10.1088/1742-6596/1046/1/012017, 012017.

Vincke, H., Theis, C., 2018. ActiWiz 3 – an overview of the latest developments and their application. J. Phys.: Conf. Ser. 1046 https://doi.org/10.1088/1742-6596/1046/1/012007, 012007.

6.2   Activation studies within the bunker of a biomedical cyclotron

Activation studies within the bunker of a biomedical cyclotron

V. Bonvin[a,b,*], F. Bochud[b], J. Damet[b,d], C. Theis[a], H. Vincke[a,c], R. Geyer[a,b]

[a] European Council for Nuclear Research (CERN), Esplanade des Particules, CH-1211 Meyrin, Switzerland
[b] Institute of Radiation Physics, Lausanne University Hospital and University of Lausanne, Rue du Grand-Pré 1, CH-1007 Lausanne, Switzerland
[c] University of Technology, Rechbauerstraße 12, 8010 Graz, Austria
[d] University of Otago, 2 Riccarton Ave, Christchurch, New Zealand

Abstract

Cyclotrons for the production of radiopharmaceuticals have become important tools in modern nuclear medicine. At the end of their lifecycles, such installations have usually to be dismantled. Activated materials have to be treated and declared according to the rules. We have developed a simulation model for the radiological characterization of components inside and around an IBA Cyclone 18/9 cyclotron. These are accelerators frequently used at hospitals. In a first publication, we applied our model to the magnetic coils of one of them and compared the results with measurements. Here, we want to extend our studies to materials situated inside the bunker using the same methods. For validation, the simulation results were compared to measurement results by using activated samples. We will discuss the simulation approach and give an example about the activation, which can be expected for materials around the cyclotron after ten years of operation.

Keywords

Cyclotron
Gamma spectrometry
Monte Carlo Simulation
Positron emission tomography
Neutron spectrum
Bunker
Activation
Decommissioning
Uncertainty estimation

1 Introduction

Positron emission tomography (PET) examinations and consequently also the cyclotrons, which are used for the production of the necessary radionuclides, have become important tools in the field of nuclear medicine during the last two decades in Europe (Eurostat, 2019). In 2019, more than 1,200 cyclotrons for medical applications were registered worldwide by the IAEA (IAEA, 2019). Half of these cyclotrons operated protons in the energy range between 16 MeV and 19 MeV. Besides the obvious medical benefits, the cyclotrons emit ionizing radiation while they are operating and can produce radioactive waste. Radiation protection has to ensure by regulations and good safety practices that workers and the public are protected when particle accelerators are running. At the time of decommissioning of an installation, all materials from the cyclotron and its environment have to be radiologically characterized. The radiological characterization represents the determination of the location and concentration of the artificially produced radionuclides inside the different components. It is evident that a good understanding of the activation processes taking place inside and near the cyclotron is essential for an efficient characterization. This is an essential input for the implementation of the appropriate decommissioning procedures.

In this context, we conducted several studies, where we examined the activation of materials from a type IBA- Cyclone 18/9 cyclotron and its environment. The installation under consideration has been mainly used for the production of the radioisotopes ^{18}F, ^{11}C and ^{13}N in the environment of a hospital since the year 2000.

In a recent publication, we summarized our results on the radiological characterization of the magnet coils of this cyclotron. We gave, for the first time, a complete and seamless picture regarding the distribution of the activation products over the full volume of the magnet coils of a medical cyclotron. We showed that the activation of the coils has been induced by secondary neutrons, which originate from interactions of the beam particles with the different target assemblies or with materials inside the vacuum chamber of the cyclotron. In order to obtain a good understanding of these neutron fields, we implemented a consistent description of all relevant sources of secondary neutrons into a Monte-Carlo model for the cyclotron using FLUKA. Following FLUKA, ActiWiz and RAW were then applied in order to calculate the activation products inside the coils. ActiWiz and RAW, which have been developed at CERN, were helpful tools in order to reduce the required computing time and to automate the analysis.

We now want to apply exactly the same simulation model and methodology for the characterization of materials inside the bunker in order to obtain additional information about the distribution of activation there. The simulation results have been compared with the activities measured by gamma spectrometry inside samples of different materials with well-known composition that have been irradiated inside the bunker for validation. Copper (CuOFE), aluminum (Al-6082), and stainless steel (SS-304 L) were used, which give us access to radionuclides produced by both thermal and fast neutrons. These alloys represent typical materials that can be found, for instance, in the cyclotron itself, the air conditioning system or the vacuum system. These measurements will give new information about the limitations of the model we applied. The development of a consistent description of the activation of the accelerator and its environment by a single simulation model is of general interest. In the following, our approach and the results obtained will be described in detail.

2 Materials & Methods

2.1 Description of the biomedical cyclotron IBA Cyclone 18/9

The activation studies described in this article were performed at a cyclotron of type IBA Cyclone 18/9 that has been in operation for the production of radioisotopes in a hospital unit since 2000. This compact accelerator with a diameter of two meters is operated inside a concrete bunker with shielding walls of two meters of thickness. The cyclotron accelerates protons up to 18 MeV with a maximum beam current of 150 µA (9.36×10^{14} protons/s). Beside protons, the cyclotron can also be operated with deuterons. The second option has been used for a few days only since its initial start-up. The machine is equipped with eight target ports for the production of radioisotopes. So far, mainly ^{18}F, ^{13}N and ^{11}C were produced by using different target materials in liquid and gaseous phase. Figure 1 shows the cyclotron inside the bunker. Figure 2 illustrates the cyclotron and its main components: the deep valley magnet with yoke, poles and coils, the dual ion source, the dees for the acceleration of particles, the vacuum chamber and the targets. The main parameters of the machine and the characteristics of the different targets are summarized in Table 1 and Table 2, respectively.

Figure 1. View of the cyclotron inside its bunker.
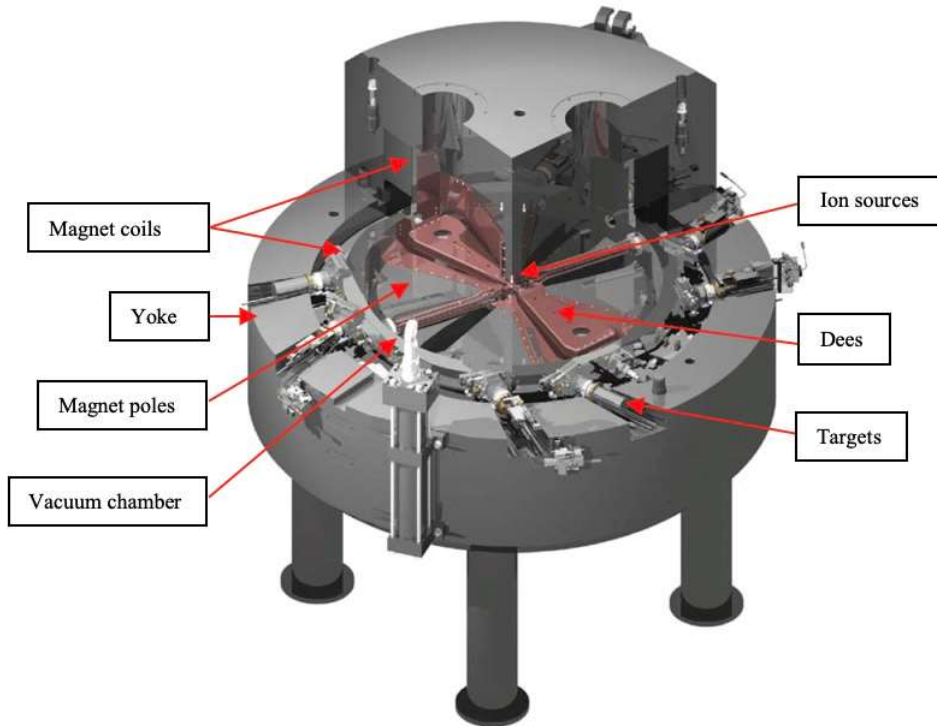
Figure 2. Sketch of the Cyclone 18/9 cyclotron (IBA, 2009).

Table 1. Main characteristics of the Cyclone 18/9 Cyclotron (IBA, 2009).

Energy [MeV]	proton	18
	deuteron	9
Intensity [µA]	proton	150 (9.36×10^{14} p/s)
	deuteron	40 (2.50×10^{14} d/s)
Particles sources	2 separate Penning Ion Gauge ion sources	
Number of target ports	8	
Simultaneous target beams	2	
Mean field [T]	1.35	
Weight [kg]	25000	

Table 2. Characteristics of the different target types (IBA, 2009).

Isotope produced	Chemical form	Target reaction	Target material	Vacuum window	Target window
^{11}C	CO_2	$^{14}N(p,\alpha)^{11}C$	N_2 + 0.5-1% O_2	12 µm Titanium	500 µm Aluminum
^{13}N	NH_3	$^{16}O(p,\alpha)^{13}N$	H_2O (natural) + 5 mMol Ethanol	12 µm Titanium	25 µm Havar®
^{15}O	O_2	$^{14}N(d,n)^{15}O$	N_2 + 0.5% O_2	12 µm Titanium	50 µm Havar®
^{18}F	F^-	$^{18}O(p,n)^{18}F$	$H_2^{18}O$ (98%)	12 µm Titanium	50 µm Havar®

2.2 Estimation of the activation of material inside the bunker by simulation

Because of its low energy (18 MeV), the proton beam is stopped after a few millimeters in matter (e.g. 3.5 mm in water). The target assemblies for the production of isotopes are integrated into the vacuum chamber. This means that beam protons cannot contribute directly to the activation of any elements outside of the vacuum chamber. The activation of materials inside the bunker (outside of the machine) is caused by the secondary neutrons produced by the interactions of the proton beam with components of the accelerator within the vacuum chamber. As detailed in our article about the activation of the magnetic coils of the cyclotron, two mechanisms for the production of secondary neutrons can be distinguished (Bonvin et al., 2020).

The first corresponds to the interactions of the nominal beam with materials on its trajectory, *i.e.* the stripper foils composed of few microns of carbon (Braccini, 2016) and the target ports. Each target port includes the collimator, the vacuum window, the target window and the target material, which is used to produce the radioisotopes of interest.

The second mechanism corresponds to "unwanted" beam losses. The main reason for this is due to the dissociation of H^- ions by the residual gas inside the vacuum chamber (Papash and Alenitsky, 2008). The resulting H atoms are no longer guided by the magnetic field. They continue tangentially from the point of ionization until they hit a material - most likely the vacuum chamber. The losses are in the order of 50 % of the accelerated beam (Papash and Alenitsky, 2008). No other beam loss was taken into account in this study.

In our approach, the calculation of the activities of any material inside the bunker requires a two analysis steps:

1. Estimation of the fluence of the secondary neutrons inside the material of consideration   with the help of the Monte Carlo tool FLUKA 2011.3 (Böhlen et al., 2014; Ferrari et al., 2005).
2. Estimation of the activation products and their activities with the help of the software tools ActiWiz version 3.3.168 (Vincke and Theis, 2018) and RAW version 4.1.2 (Geyer et al., 2019).

In order to calculate the neutron fluence inside the bunker, we want to stick to the same description of the cyclotron in FLUKA as already applied in our first publication about the magnetic coils of the same machine. In this manner, we can verify the correctness and limitations of this approach. Although a detailed description of the Monte-Carlo model has been given already in this previous article (Bonvin et al., 2020), we want to recapitulate some of the main aspects here for a better readability. As already mentioned, two mechanisms for the production of secondary neutrons are responsible for the activation of material inside the bunker: the interaction of the beam with the targets and beam losses inside the machine.

Each of the target ports can be considered as an individual "point-like" source of secondary neutrons. Two types of target assemblies can be distinguished: those using liquid target materials, like for the production of ^{18}F and ^{13}N, and those using gaseous target materials, like for the production of ^{11}C. The related schematics, as modelled in FLUKA, are shown in Figure 3 and Figure 4, respectively. The two target assemblies vary significantly by their geometry and the materials being used. The 18 MeV proton beam was assumed to be pencil like. The interaction of the beam with the collimators was not taken into account because no detailed information on the beam emittance was available at these locations.

The beam losses during acceleration are expected as an additional source for secondary neutrons. A simplified model for the beam loss mechanism was implemented in FLUKA for the calculation of the related neutron fluence. It is assumed here that 50% of the accelerated H^- beam particles are ionized by the residual gas inside the vacuum system. The stripping process in our simulation is uniformly distributed over the region of acceleration. The resulting H-atoms (Ionization of H^-) will tangentially continue their trajectories with a momentum $p = qBr$, where r is the radius of the trajectory at the stripping location, q the elementary charge and B the magnetic field. They will interact with the vacuum chamber, where neutrons are produced.

Although the acceleration and stripping process were not simulated in detail, this simplified model reproduces the correct interaction rate of lost beam particles with the vacuum chamber. However, the real spatial distribution of the ionization processes could be different. Consequently, the energy spectrum of interacting particles may therefore deviate from what is assumed here as a first approximation.

The properties of the target ports T1-T8 as secondary neutron sources are summarized in Table 3. The beam losses (BL) were added also to this list. For each of the nine sources, independent simulations are carried out in FLUKA taking into account the full geometry of the cyclotron.
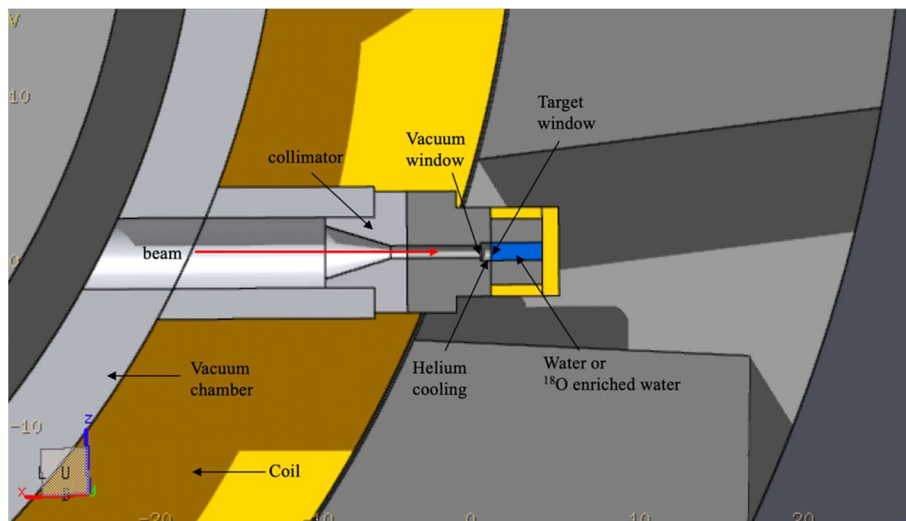
Figure 3. Target assembly for the production of ^{18}F or ^{13}N.
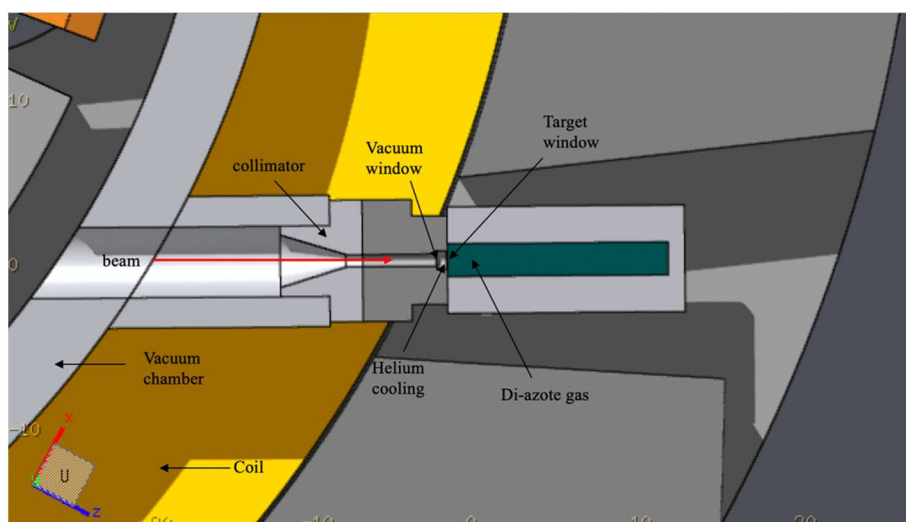
Figure 4. Target assembly for the production of ^{11}C.

Table 3. List of neutron sources taken into account for the simulation. The "isotope produced" column defines the target type (see also Table 2 for additional information).

Source	Isotope produced	Target material used in FLUKA
T1	^{18}F	$H_2^{18}O$
T2	^{18}F	$H_2^{18}O$
T3	Not used	-
T4	^{11}C	N_2 gas at 20 bars
T5	^{18}F	$H_2^{18}O$
T6	^{18}F	$H_2^{18}O$
T7	^{13}N	H_2O
T8	Not used	-
BL	-	Vacuum Chamber

The geometry of the cyclotron inside the bunker as described by our FLUKA model is shown in Figure 5. Special care was taken that the position and the orientation of the machine were correctly implemented. They were validated relative to the bunker by survey measurements with a precision of $\pm$ 5 mm and $\pm$ 0.2°, respectively. An important detail is the chemical composition of the concrete walls, because it may influence the flux of the thermal neutrons inside the bunker. The chemical composition in our model was taken from (IBA, 2009). No information about the real chemical composition of the concrete has been available for this study.
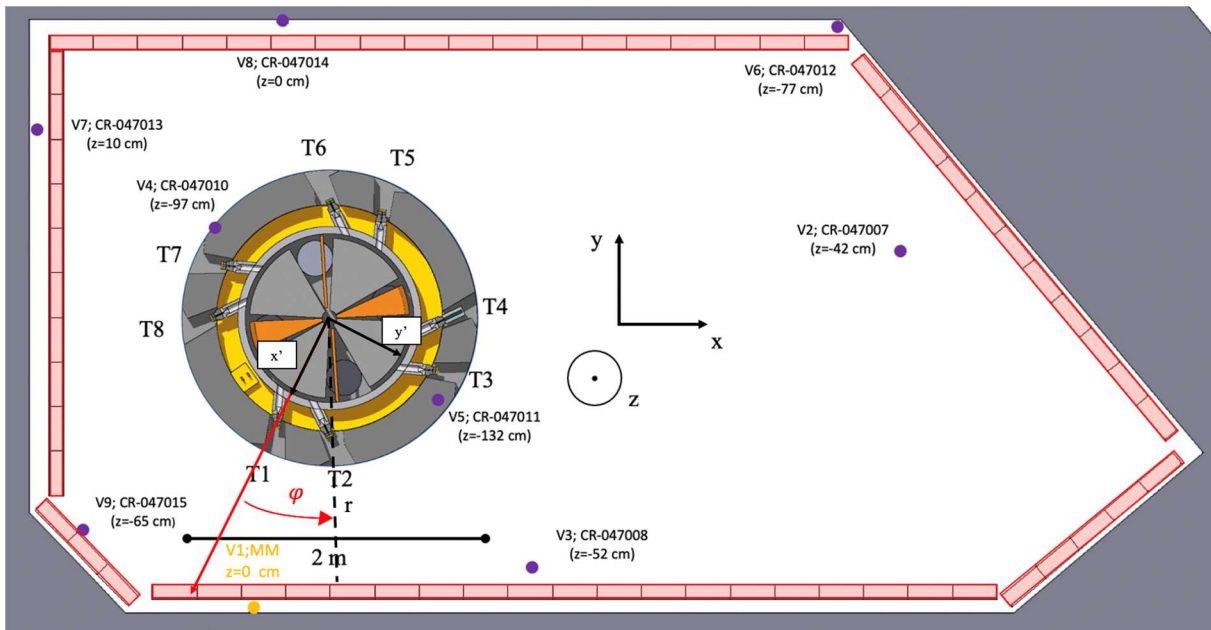
Figure 5. Cyclotron inside the bunker as simulated in FLUKA. The wall thicknesses are about two meters or more.

For the calculation of the activation of a material at a given location with ActiWiz, the neutron fluence must be determined first. As an illustrative example: we placed material samples at nine different locations inside the bunker for the validation of the model. In order to score the corresponding neutron fluences, nine scoring volumes V_i were defined with $i \in [1,\ldots,9]$ at the location of the samples. The locations of these scoring volumes are indicated in Figure 5 by the colored dots (yellow and purple). Then, the FLUKA calculations deliver the

differential fluence of the secondary neutrons $\Phi_i^s(E)$ inside the volumes V_i for each of the neutron sources s listed in Table 3.

For the characterization of material inside the bunker, a more systematic approach for the scoring could be appropriate. Figure 5 also shows an example of scoring volumes distributed all along the walls of the bunker (red color). We introduce here a cylindrical coordinate system (r, φ, z) to study the spatial distribution. Its origin is defined by the center of the cyclotron. The angle $\varphi = 0$ is given with respect to the line (highlighted in red), which connects the center with the middle of the target window of T1. The scoring volumes shown in red have been put to a height $z = 0$.

As in our previous article, the activation products within the volumes V_i of a given material and their associated activities are calculated in a second step using ActiWiz 3.3, a software tool developed at CERN. Again, we want to stick to exactly the same formalism as applied already for the characterization of the magnetic coils of the same cyclotron. Its main features are recapitulated here. ActiWiz 3.3 facilitates the determination of production rates and activities of elementary or composite materials by using radiation fields with complex irradiation patterns. An irradiation pattern is defined here as sequence of consecutive periods of constant beam currents with periods without beam between (if required) and a cooling down period at the end. Thus, realistic irradiation scenarios with production cycles and variable beam currents can be described. For a given volume V_i and a differential neutron fluence $\Phi_i^s(E)$ from the source s, the ActiWiz calculations will return for given material (element or compound) a list of the activated nuclides $\{n_{i,j}^s\}$ with $j\epsilon[1, m_i^s]$ together with the corresponding specific activities $a_{i,j}^s$ and their uncertainties $\Delta a_{i,j}^s$. m_i^s is the number of nuclides produced in the volume V_i by the source s. The result can be grouped together into activation tuples $\boldsymbol{N_i^s}$ containing m_i^s triplets with the information about the produced nuclides, their activities and uncertainties.

$$\boldsymbol{N_i^s} = \left\{\left(n_{i,1}^s a_{i,1}^s, \Delta a_{i,1}^s\right), \dots, \left(n_j^s, a_{i,j}^s, \Delta a_{i,j}^s\right), \dots, \left(n_{m_i^s}^s, a_{i,m_i^s}^s, \Delta a_{i,m_i^s}^s\right)\right\} \qquad (1)$$

ActiWiz estimates the uncertainties $\Delta a_{i,j}^s$ by the propagation of the statistical uncertainties of the fluence spectra $\Phi_i^s(E)$ only. Other sources of uncertainties are not taken into account. The result for the total specific activities of the nuclides inside the volume V_i is obtained by summing over all neutron sources:

$$\boldsymbol{N_i} = \sum_s \boldsymbol{N_i^s} = \left\{\left(n_{i,1}, a_{i,1}, \Delta a_{i,1}\right), \dots, \left(n_{i,k}, a_{i,k}, \Delta a_{i,k}\right), \dots, \left(n_{i,m_i}, a_{i,m_i}, \Delta a_{i,m_i}\right)\right\} \qquad (2)$$

, where $\{n_{i,k}\} = \bigcup_s \{n_{i,j}^s\}$ is the union set of the nuclides produced by the different sources in the volume V_i with $k\epsilon[1, m_i]$ and m_i is the corresponding number of nuclides. The activities and uncertainties simply result from:

$$a_{i,k} = \sum_s a_i^s(n_{i,k}) \qquad (3)$$

$$\Delta a_{i,k} = \sqrt{\sum_s \left(\Delta a_i^s(n_{i,k})\right)^2} \qquad (4)$$

The functions $a_i^s(n_{i,k})$ and $\Delta a_i^s(n_{i,k})$ return the activity and its uncertainty of the nuclide $n_{i,k}$ from $\boldsymbol{N}_i^s$. In order to facilitate the calculations, the software tool RAW was used, which permits to determine $\boldsymbol{N}_i$ in an automated way.

2.3   Activated material samples from the bunker for validation

For the validation of the simulation model, materiel samples have been irradiated inside the bunker of the cyclotron. In a first experiment (called campaign C1), a copper (CuOFE), aluminum (Al-6082) and stainless steel (SS-304L) disc of about 100 gram each have been irradiated downstream of the target T1 next to the wall for one week. As we will see later, these samples will deliver also important information about the uncertainties and limitations of the applied model. The irradiation location is labelled with 'MM' and is shown in Figure 5. The discs are shown at the top of Figure 6. During that week, only one target (T1), was used (for the production of ^{18}F), which corresponds to a relatively simple irradiation scenario. The average beam current on target T1 is given in Figure 7 for each day of that week. This quantity is calculated from the total charge of the beam, which is measured by the control system of the accelerator for this target during a day, divided by 24 h. This is simultaneously the irradiation profile being used for the analysis with ActiWiz.
In a second experiment (called campaign C2), sample bags were placed for irradiation at eight different locations inside the bunker. Each sample bag contained again three discs made from copper (CuOFE), aluminum (Al-6082) and stainless steel (SS-304L). This time, the weight of each sample was about 10 grams. The corresponding irradiation locations are labelled with 'CR-' followed by an identifier. The locations were indicated already in Figure 5. The discs are shown at the bottom of Figure 6. These samples have been irradiated for 11 months. During this period, the targets T1, T2 and T5 were used for the production of ^{18}F while the target T7 was used for the production of ^{13}N. The average beam current on these targets for each day of that period are summarized in Figure 8 (blue curve). The simplified irradiation profiles used for the calculations in ActiWiz are shown in red. The simplified profiles use the average beam current per month and, for the last month before the end of the irradiation, the average beam current per day. This campaign corresponds to a more realistic irradiation scenario for waste considerations compared to the first one, since several targets were used in parallel.
Altogether, 27 samples were irradiated in these two campaigns. The dates of irradiation and measurements are summarized in Table 4.
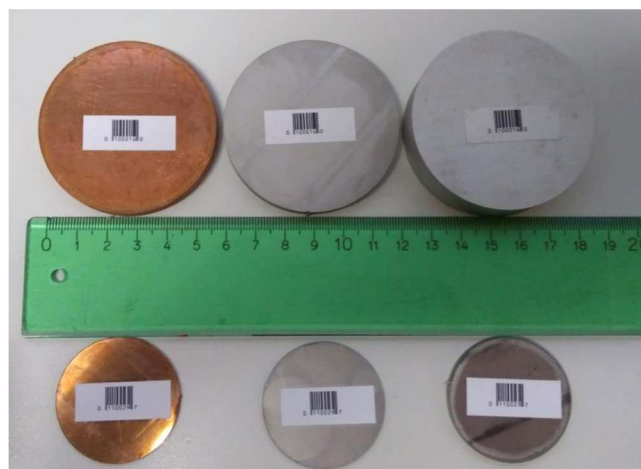
Figure 6. Material samples irradiated at the bunker. Top: 100 grams. Bottom: 10 grams. From left to right: copper (CuOFE), aluminum (Al-6082), stainless steel (SS-304L).

Table 4. Irradiation and measurement dates of both campaigns.

Campaign names	C1	C2
Installation date	May 6, 2019 15:35	June 6, 2016
Removal date	May 13, 2019 11:48	April 24, 2017
Start of the first irradiation	May 7, 2019 02:00	June 7, 2016 01:19
End of the last irradiation	May 9, 2019 04:25	April 23, 2017 10:26
Start of the measurement	May 15, 2019 00:12	April 26, 2017 18:08
End of the measurement	May 15, 2019 03:22	May 2, 2017 18:27

After irradiation, each sample has been measured by a High Purity Germanium (HPGe) detector of type GC9021 from Mirion Technologies (Canberra). The spectra were analyzed with the Genie 2000 application software. The detection efficiencies for all samples were determined with LabSOCS (Mirion, 2017). The exact sample dimensions of the samples used for the efficiency calculations are summarized in Table 5. The samples were measured at relatively small distances of a few mm from the detector in order to get a low MDA (minimum detectable activity) in a reasonable measurement time. Cascade corrections were applied during the analysis.

Table 5. Dimensions of the Samples.

Sample type	Height [mm]	Diameter [mm]	Weight [g]
Copper Large	5	60	126
Copper Small	1	40	11.2
Al-6082 Large	15	60	117
Al-6082 Small	3	40	10.4
SS-304L Large	5	60	112
SS-304L Small	1	40	9.9

For the activation calculations, the chemical composition of the material samples has to be known with good precision. Therefore, the samples were analyzed by a chemical laboratory (Wood Nuclear Limited (now named JACOBS), Warrington, UK). The results are summarized in Table 6, Table 7 and Table 8, respectively.

Table 6. Chemical composition of the copper (CuOFE) samples.

Element	wfr (%)	
	Small	Large
Cu	> 99.99	> 99.99
Ag	0.00142 ± 0.00015	0.00229 ± 0.00024

Table 7. Chemical composition of the aluminum (Al-6082) samples.

Element	wfr (%)	
	Small	Large
Al	96.44 ± 0.4	95.56 ± 0.5
Cr	0.39 ± 0.042	0.32 ± 0.036
Cu	0.11 ± 0.012	0.2 ± 0.02
Fe	0.76 ± 0.22	0.65 ± 0.19
Mg	1.37 ± 0.29	1.7 ± 0.35
Mn	0.73 ± 0.091	1.3 ± 0.17
Si	0.05 ± 0.036	0.07 ± 0.047
Ti	0.05 ± 0.0082	0.04 ± 0.0063
Zn	0.1 ± 0.012	0.16 ± 0.018

Table 8. Chemical composition of the stainless steel (SS-304L) samples.

Element	wfr (%)	
	Small	Large
Cr	21.3 ± 4.4	21.2 ± 4.4
Co	0.29 ± 0.03	0.28 ± 0.029
Fe	61.41 ± 4.2	63.61 ± 4.4
Mn	2.4 ± 0.3	2.2 ± 0.27
Mo	0.53 ± 0.057	0.35 ± 0.038
Ni	13.6 ± 1.5	12 ± 1.3
Ph	0.23 ± 0.048	0.16 ± 0.076
Si	0.03 ± 0.017	0.03 ± 0.007
W	0.09 ± 0.009	0.06 ± 0.006
Va	0.12 ± 0.012	0.11 ± 0.012

As an example, the identified nuclides with their corresponding activities a_i^{meas} and uncertainties Δa_i^{meas} are given in Table 9, Table 10 and Table 11 for the aluminum, copper and stainless steel samples of the campaign C1. The uncertainties include both, the statistical uncertainties and the uncertainties from the efficiency calibration. The radionuclides with half-lives below 5 days (^{24}Na, ^{64}Cu, ^{99}Mo and ^{187}W) will not be considered in the following study because they will rapidly decay. Consequently, they are not of importance for the characterization of waste. The results for the campaign C2 are summarized in Appendix A, Table S1 to S3.

Table 9. Measured activity at the location MM for the aluminum sample

Radionuclide	Half-life	a_i^{meas} (Bq.g^{-1})	$\Delta a_i^{meas}/a_i^{meas}$ (%)
^{51}Cr	27.71 d	2.5×10^{-1}	19.3
^{24}Na	14.9 h	2.4×10^{-1}	13.2
^{65}Zn	243.66	1.2×10^{-2}	22.7
^{54}Mn	312 d	3.9×10^{-3}	28.4

Table 10. Measured activity at the location MM for the copper sample

Radionuclide	Half-life	a_i^{meas} (Bq.g^{-1})	$\Delta a_i^{meas}/a_i^{meas}$ (%)
^{64}Cu	12.7 h	6.2	16.4
^{60}Co	5.27 d	1.2×10^{-2}	17.9

Table 11. Measured activity at the location MM for the stainless steel sample

Radionuclide	Half-life	a_i^{meas} (Bq.g^{-1})	$\Delta a_i^{meas}/a_i^{meas}$ (%)
^{51}Cr	27.71 d	2.3×10^{1}	17.8
^{58}Co	70.86 d	2.0	14.5
^{59}Fe	44.4 d	3.4×10^{-1}	13.2
^{99}Mo	2.74 d	3.3×10^{-1}	16.4
^{54}Mn	312 d	3.0×10^{-1}	15.3
^{187}W	23.72 h	2.7×10^{-1}	14.8
^{60}Co	5.27 y	2.6×10^{-1}	13.1
^{57}Co	271.79 d	3.5×10^{-2}	15.9
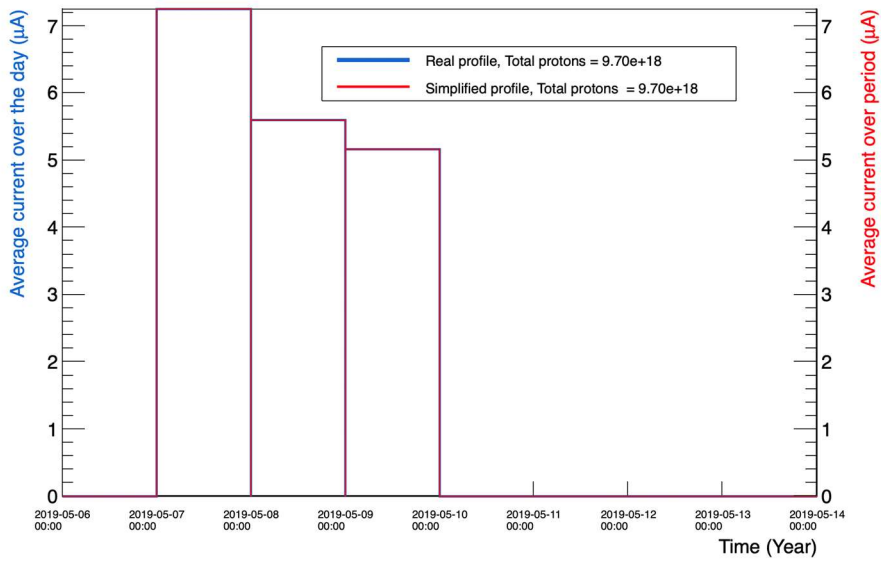
Figure 7. Average beam currents per day for campaign C1 as used for the ActiWiz calculations.
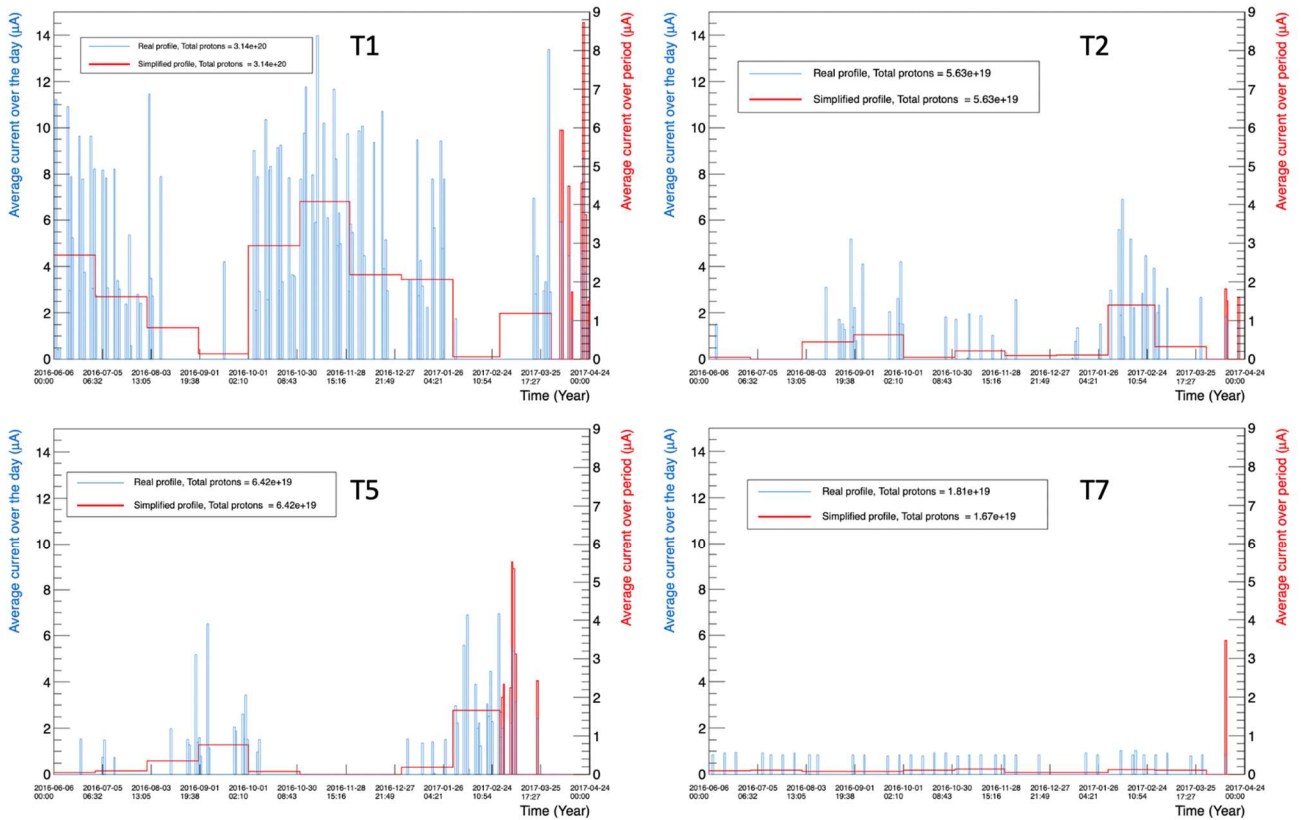
Figure 8. Average beam currents per day for the targets T1, T2, T5 and T7 during campaign C2 (blue color). Simplified irradiation profile used for ActiWiz (red color).

3   Simulation results and comparison with measurements.

The activation of the samples was calculated using the tools as described in section 2.2. The results of the campaigns C1 and C2 will be discussed separately in two subsections.

During the first campaign C1, only one target (T1) was operated during one week. The irradiation location MM of the samples is directly downstream of T1 in front of the wall. The irradiation profile shown in Figure 7 is relatively simple. The simulation results are then compared with those of gamma spectrometry.

The second campaign C2 represents an irradiation scenario over almost one year of daily operation. Four targets have been operated during this period for the production of different radionuclides. The samples were distributed randomly over the full area of the bunker. Here again, the simulation results will be compared with those from measurements.

In both cases, we will discuss the results and the related uncertainties.

3.1   Calculation of the activation of the samples of campaign C1

Three samples were located at the position MM straight in front of the target T1 as shown in Figure 5. This target uses $H_2{}^{18}O$ for the production ^{18}F. We scored the differential neutron fluence at the location of MM as a function of energy with FLUKA for three different processes:

1. Secondary neutrons are produced by the interaction of beam particles with the target and vacuum windows as well as the target material (here the liquid).
2. Secondary neutrons are produced by the interactions of beam particles with the collimator. A loss of 20 % of the beam is assumed here.
3. Secondary neutrons are produced by beam losses. A loss of 50 % of the accelerated beam is assumed.

The simulation results are shown in Figure 9 for the example of the stainless steel sample. The simulation took into account the material and geometry of that sample. The neutron fluence is clearly dominated here by beam interactions inside the target material. Although the beam loss inside the machine is 50 % of the accelerated beam, its contribution to the activation of the samples can be neglected. The neutrons emitted by the collimator contribute likewise with less than 5 % over the full energy range at the sample location.
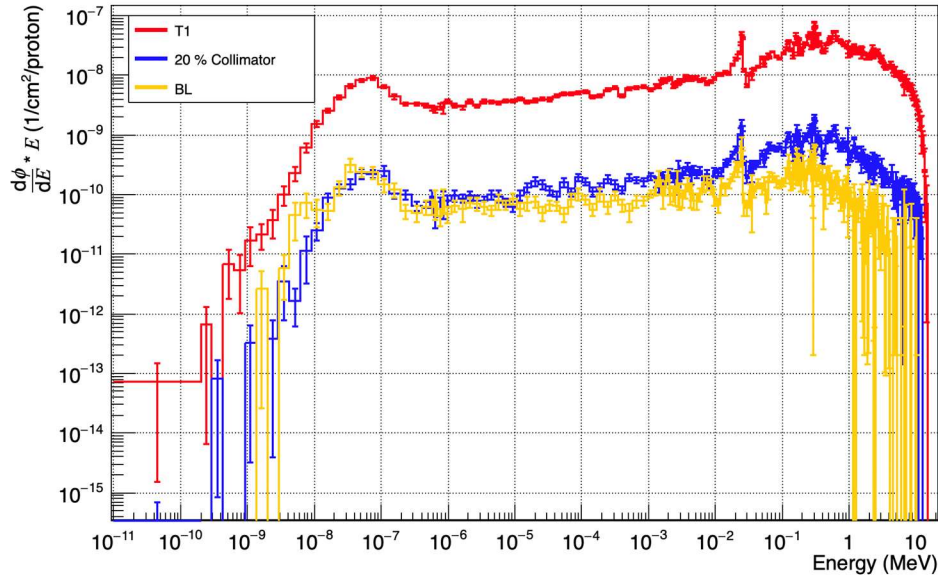
Figure 9. Neutron spectrum inside the stainless steel sample at the position of the MM sample.

The spectrum of the neutrons, as emitted by the proton interactions inside the target liquid, are shown in Figure 10 as a function of the polar angle. The width of the interval for scoring was 6 degrees for each angle. The target liquid corresponds to the strongest source of neutrons and dominates the activation at the location of MM. This spectrum has been generated by an idealistic model, where the 18 MeV protons interact with the two target windows and a small cylinder (6 mm length, 1 mm diameter, no walls) filled with $H_2^{18}O$. The dimensions of the cylinder have been reduced compared to the real one in order to avoid the scoring of scattered neutrons. Its length with 6 mm is long enough to stop all protons of the beam. The neutron fluence was scored by a sphere around the target with a diameter of 15 cm. We also examined qualitatively the correlation between the neutrons emitted by the target with the spectrum observed at the location MM. While the high energetic part (above one MeV) of the spectrum at the sample location is dominated by neutrons, which are emitted by the target under small angles, the low energetic part is related to a wide range of angles up to ninety degrees and more. In the second case, secondary interactions of the neutrons inside the yoke of the cyclotron and the walls of the bunker play an important role.
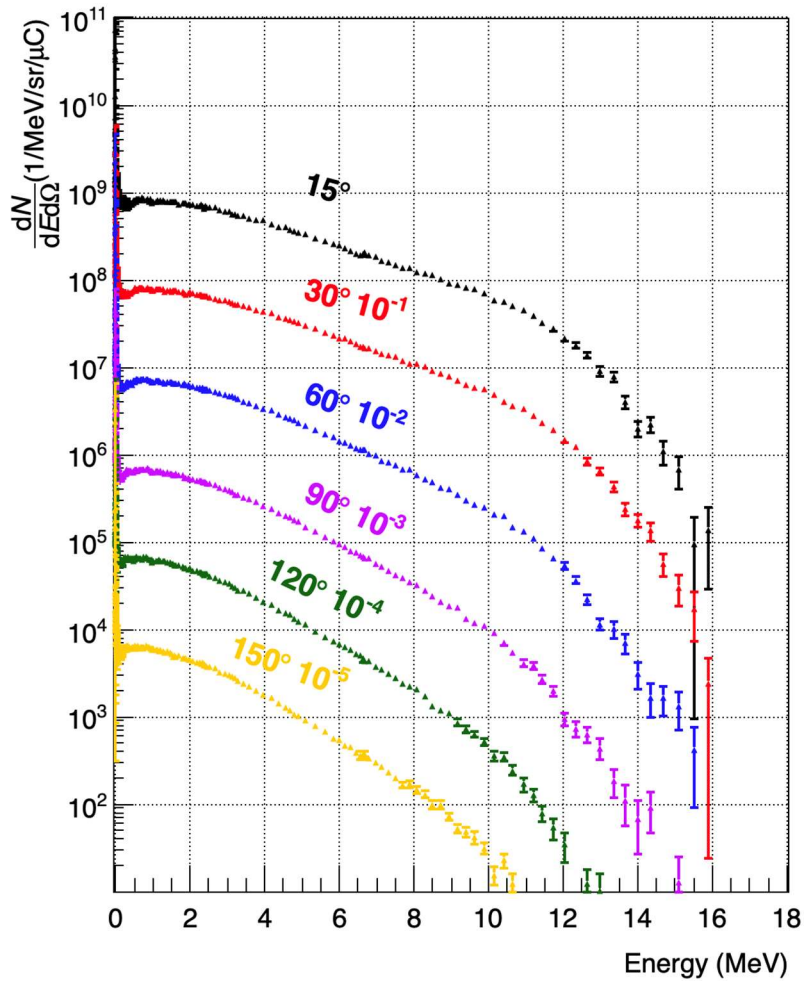
Figure 10. Neutron fluence emitted by the target material for the production of ^{18}F as function of the emission angle.

In a second analysis step, the activation products inside the copper, aluminum and stainless steel samples were calculated by ActiWiz using the spectrum shown in Figure 9. The irradiation profile from Figure 7 was used for the beam current as another input. Realistic cooling times were assumed for each sample before measurement, which were in the order of 5 days. Since the irradiation profile is constructed by the average beam currents per day, the precision for nuclides with short half-lives will be limited. However, this poses no limitation for the characterization of waste where the cooling times are anyhow comparably large. The ActiWiz results for the nuclide content for the three samples are given in the Table 12, Table 13 and Table 14, respectively. These tables include all nuclides with activities larger than 10^{-3} Bq.g^{-1} and with a half-life larger than five days. Radionuclides, which are 'difficult to measure' like beta emitters have been marked in red. The energy intervals of the neutrons, where the major part (>80%) of theses radionuclides are produced, have been added to these tables as well.

Before we discuss any results, we want to first analyze possible sources of uncertainties. Several limitations of the model will contribute to the uncertainties of the activities. Let us consider the situation of a chemical compound made from N different elements e, which contribute with the weight fractions wfr_e. The activity of a radionuclide i is calculated by the formula:

$$a_i^{sim} = \sum_{e=1}^{N} a_{i,e} \cdot wfr_e \qquad (5)$$

The corresponding uncertainty Δa_i^{sim} is obtained by:

$$\Delta a_i^{sim} = \sqrt{\sum_{e=1}^{N} (\Delta a_{i,e} \cdot wfr_e)^2 + \sum_{e=1}^{N} (a_{i,e} \cdot \Delta wfr_e)^2} \qquad (6)$$

The second term $\Delta a_i^{sim,chem} = \sum_{e=1}^{N}(a_{i,e} \cdot \Delta wfr_e)^2$ describes the contributions from the uncertainties of the chemical composition and can be calculated easily using the uncertainties given in the Table 6, Table 7 and Table 8.

In contrast, the first term $\Delta a_i^{sim,mod} = \sum_{e=1}^{N}(\Delta a_{i,e} \cdot wfr_e)^2$, which depends on the uncertainties of the calculated activities $a_{i,e}$ by our model, is relatively complex and requires additional considerations.

A trivial contribution comes from the limited statistics when the fluence spectra are calculated at the location MM with FLUKA. The corresponding relative uncertainties $\Delta a_i^{sim,stat}/a_i^{sim}$ are delivered automatically by ActiWiz as discussed in chapter 2.2. They are listed in Table 12, Table 13 and Table 14 together with $\Delta a_i^{sim,chem}/a_i^{sim}$. Uncertainties from the production cross-sections of the nuclides are not taken into account here.

Table 12. Simulation results for the stainless steel (304L) sample at the position MM.

Radionuclides	Energy range of production (MeV)	LL	Half-life	a_i^{sim} (Bq·g⁻¹)	$\dfrac{\Delta a_i^{sim,chem}}{a_i^{sim}}$	$\dfrac{\Delta a_i^{sim,stat}}{a_i^{sim}}$
^{51}Cr	$[10^{-8};10^{-6}]$	100	27.71 d	6.1×10^1	0.21	0.03
^{58}Co	$[3; 9]$	1	70.86 d	8.4	0.11	0.02
^{55}Fe	$[10^{-8} ; 5 \times 10^{-6}]$	1000	2.74 y	1.2	0.7	0.03
^{60}Co	$[10^{-8}; 10^{-4}]$	0.1	5.27 y	7.7×10^{-1}	0.1	0.03
^{59}Fe	$[10^{-8};10^{-5}]$	1	44.6 d	6.2×10^{-1}	0.07	0.03
^{54}Mn	$[3; 9]$	0.1	312 d	7.3×10^{-1}	0.07	0.02
^{32}P	$[10^{-8};10^{-6}]$	1000	14.27 d	3.3×10^{-1}	0.36	0.03
^{185}W	$[4 \times 10^{-8} ;10^{-2}]$	1000	75,1 d	8.5×10^{-2}	0.1	0.02
^{63}Ni	$[10^{-8}; 8 \times 10^{-7}]$	100	100.1 y	2.2×10^{-2}	0.11	0.03
^{57}Co	$[10; 14]$	1	271.79 d	2.7×10^{-2}	0.11	0.11
^{92m}Nb	$[4;10]$	10	10.15 d	1.6×10^{-2}	0.11	0.05
^{181}W	$[2 \times 10^{-8} ;11]$	10	121.2 d	2.0×10^{-3}	0.10	< 0.01

Table 13. Simulation results for the aluminum (6082) sample at the position MM.

Radionuclides	Energy range of production (MeV)	LL	Half-life	a_i^{sim} (Bq·g⁻¹)	$\dfrac{\Delta a_i^{sim,chem}}{a_i^{sim}}$	$\dfrac{\Delta a_i^{sim,stat}}{a_i^{sim}}$
^{51}Cr	$[10^{-8};10^{-6}]$	100	27.71 d	9.5×10^{-1}	0.11	0.03
^{65}Zn	$[10^{-8}; 5 \times 10^{-2}]$	0.1	243.66 d	6.8×10^{-2}	0.12	0.02
^{55}Fe	$[10^{-8} ; 5 \times 10^{-6}]$	1000	2,74 y	1.2×10^{-2}	0.29	0.03
^{54}Mn	$[3.5; 13.5]$	0.1	312 d	1.3×10^{-2}	0.17	0.05
^{59}Fe	$[10^{-8};10^{-5}]$	1	44.6 d	6.4×10^{-3}	0.29	0.03

Table 14. Simulation results for the copper (CuOFE) sample at the position MM.

Radionuclides	Energy range of production (MeV)	LL	Half-life	a_i^{sim} (Bq.g^{-1})	$\dfrac{\Delta a_i^{sim,chem}}{a_i^{sim}}$	$\dfrac{\Delta a_i^{sim,stat}}{a_i^{sim}}$
^{60}Co	[6;11]	0.1	5.27 y	3.3×10^{-2}	<0.001	0.03
^{63}Ni	[2;8]	100	100.1 y	2.6×10^{-2}	<0.001	0.02
^{110m}Ag	[10^{-8}; 6×10^{-5}]	0.1	249 d	1.9×10^{-3}	0.1	0.02

Important systematic contributions to $\Delta a_i^{sim,mod}$ originate from the calculations of the neutron fluences with FLUKA. Possible reasons are:

- The precision of the geometrical modelling of the facility and samples.
- Description of the beam and beam interactions.
- Cross-sections and material assumptions, which contribute to the production and absorption of secondary neutrons.

These uncertainties cannot be propagated in a simple analytical way. Parameters of the simulation model were varied within uncertainties in order to obtain additional information about their impact on $\Delta a_i^{sim,mod}$. The related results are summarized because of the complexity in separated sub-sections below.

3.1.1 Geometrical description of the facility and the samples

As described before, the position of the cyclotron and its orientation has been surveyed with quite good precision. It has been implemented with the same precision in FLUKA using detailed technical drawings. On the contrary, the exact position of the targets is not indicated by these drawings. They are to some degree adjustable. Similar considerations apply also to the samples at the irradiation location MM. The position of the target T1 were altered in the model by ± 3 cm along the beam axis. In the same way, the positions of the samples were varied by ± 5 cm horizontally on the wall. No significant differences larger than the statistical uncertainties have been observed over the full range of energy of the neutrons in both cases.

As shown in Figure 11, the geometry of the target T1 has been implemented in FLUKA with some simplifications compared to reality. For example, the cooling system and the associated connections were not described in full detail by our modelling. We estimated the error $\Delta a_i^{sim,geotar} = (a_i^{sim,geotar} - a_i^{sim})$ by adding a brass cylinder with a length of two centimeter and a diameter of one centimeter at the end of the target. The impact on the neutron fluence spectrum at the position MM can be seen in Figure 12. The following ratio was plotted:

$$\frac{\phi_{MM}^{geotar}(E)}{\phi_{MM}(E)}$$

The differential neutron fluence $\phi_{MM}^{geotar}(E)$ is the FLUKA result at the location MM for the target including the brass cylinder and the differential neutron fluence $\phi_{MM}(E)$ is the result for the simplified model of the target.

A significant effect has been seen only for neutrons with energies above 2 MeV. The related relative uncertainties $\Delta a_i^{sim,geotar}/a_i^{sim}$ for the radionuclides, which are produced inside the copper, aluminum and stainless steel sample, are summarized in Table 16 of section 3.1.3. As

can be seen, the uncertainties are correlated with the energy range of neutrons, where the nuclides are produced and become largest for ^{57}Co produced in stainless steel.
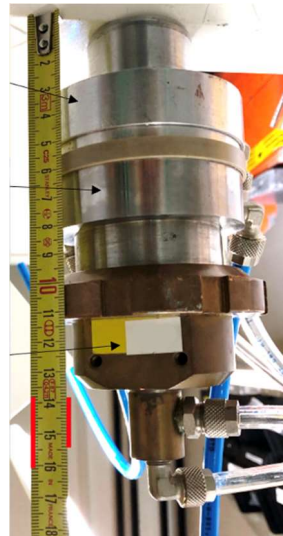
Figure 11. Photo of the target assembly for the production of ^{18}F.
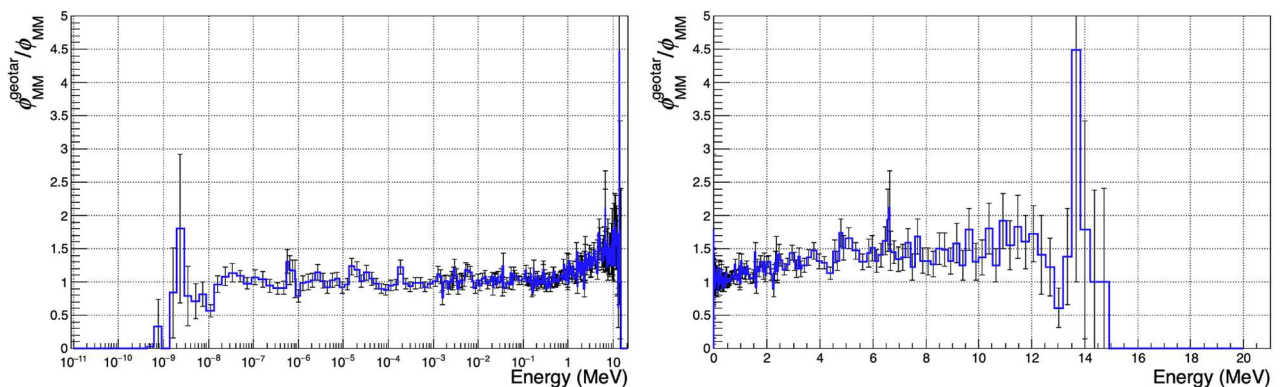
Figure 12. Ratio between the spectrum with and without the brass connector. Left: logarithmic energy axis. Right: linear energy axis.

3.1.2 Description of the beam interactions with the target

As already shown in Figure 9, the impact of beam interactions inside the collimator on the spectrum of neutrons at the location of MM is at maximum 5 % compared to those neutrons, which originate from the target liquid of T1. Therefore, also the production of any radionuclide is not affected by more than this quantity by the collimator. This result was validated by simulations, where the activities of the radionuclides inside the samples were calculated with such collimator events.

In order to test our simulation assumptions, we calculated the amount of ^{18}F produced inside the target T1 for a typical production run of the installation and compared this quantity with the measured activity of ^{18}F after extraction of the liquid. While the simulated value is in good agreement with expectations published by IAEA (IAEA, 2018), the measured saturation yield

is by a factor 0.54 lower compared to the theoretical value. Similar factors have been observed already by several other studies. The values are listed in Table 15.

In our simulation, we assumed naively that the target cell is filled up to 100% by the liquid and the beam is pencil like. We assumed that all protons entering the target cell would be stopped inside the liquid. In fact, the recommended filling level of the target cell is only between 50-60 % (Yilmaz, n.d.). More than 1 kW of power is dissipated by the beam inside the cell within a very small volume, heating up the liquid and pressurizing the cell to roughly 30 bars. Little is known about the phase state of water under such conditions. Under thermal equilibrium, the liquid would have a density of 0.8 g/cm^3 and the vapor around 0.015 g/cm^3. The fact that less ^{18}F is produced than expected suggests that a part of the beam particles traverse the target volume without being stopped by the liquid phase and interacts possibly with the niobium of the containment.

Table 15. Comparison between the IAEA recommended saturation yield and the different studies.

Studies	Cyclotron	Energy (MeV)	Saturation yield (GBq/μA)	IAEA recommended saturation yield (GBq/ μA)	FLUKA Saturation yield (GBq/ μA)	$\dfrac{Studies}{IAEA}$
Our installation	IBA 18/9	18	7.4	13.8	13.9	0.54
(Stokely et al., 2012)	IBA 18/9	18	8.8	13.8	-	0.64
(Leporis et al., n.d.)	IBA 18/9	18	8.5	13.8	-	0.61
(Devillet et al., 2013)	IBA 18/9	18	8.5	13.8	-	0.61

In order to get an estimation on the uncertainties linked to the phase state, we simulated the two extreme cases.

1. The target is filled with 100 % with water with a density of 0.8 g/cm^3.
2. The target is filled with 100 % with vapor with a density of 0.015 g/cm^3.

In the first case, the neutron production is dominated by interactions with $H_2{}^{18}O$. In the second case, the neutron production is dominated by the interactions with niobium, since the vapor density is too small to stop the beam. Nevertheless, both cases result in a very similar neutron spectrum at the location of MM. Figure 13 shows the ratio of the neutron fluences between case 1 and case 2 at the position MM as a function of energy. At energies below 1 MeV both scenarios give similar results within a few percent, while at energies above 2 MeV there are significant differences between a factor 0.5 and 2. The specific activities can be estimated more precisely by taking into account both phases with:

$$a_i^{sim,phase} = \left(f_{phase} \cdot a_i^{sim,case\ 1} + \left(1 - f_{phase}\right) \cdot a_i^{sim,case\ 2}\right) \qquad (7)$$

Here, f_{pha} is the fraction of beam particles, which traverse the liquid and contribute to the production of 18F. The relative differences $\Delta a_i^{sim,phase}/a_i^{sim} = (a_i^{sim,phase} - a_i^{sim})/a_i^{sim}$

for the different radionuclides are summarized again in Table 16. We used for the calculations the value $f_{pha} = 0.54$ from our installation.
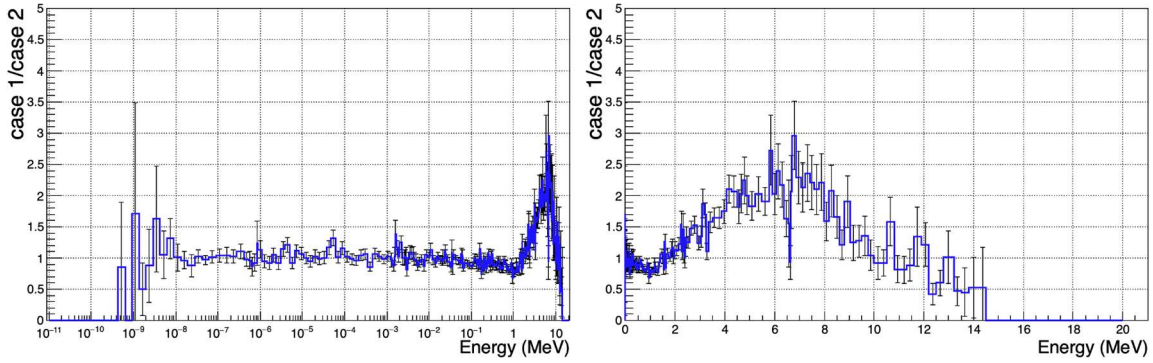
Figure 13. Ratio of the fluence spectra at the location of MM for $H_2^{18}O$ in liquid phase and in vapor phase.

3.1.3 Concrete walls of the bunker

As mentioned above, the concrete walls play an important role in the production of thermal neutrons inside the bunker. Unfortunately, no detailed information has been available about the type of material being used at the installation discussed here. In order to understand the impact of the choice of material on the activation of samples at the location MM, we repeated the simulation for three additional types of concrete, namely Portland, Barite and Magnetite, with densities of 2.3, 3.35 and 3.45 g·cm^{-3}. The chemical compositions were taken from (William et al., 2006). The fluence spectra are shown in Figure 14. Obviously, the impact is largest at thermal energies. At higher energies, the differences vanish. The highest flux of thermal neutrons is observed with Portland, the lowest with Magnetite. The activities of the radionuclides from both simulations were used to estimate uncertainty intervals $\left[\Delta a_{i,low}^{sim,con} = (a_i^{sim} - a_i^{sim,magnetite}), \Delta a_{i,high}^{sim,con} = (a_i^{sim} - a_i^{sim,portland}) \right]$ associated with the composition of the walls. These intervals are given in the Table 16 below.
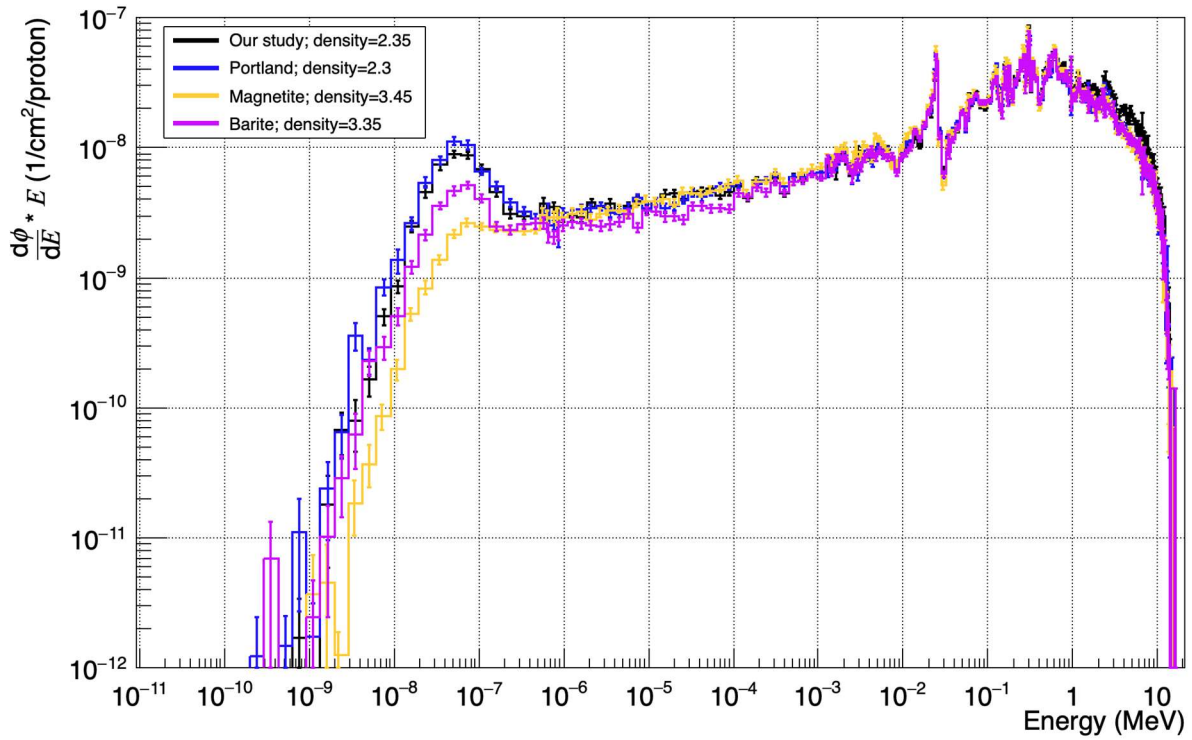
Figure 14. Neutron fluence spectra at the location MM for the different concretes.

Table 16. Table summarizing the different uncertainties for the radionuclides produced inside the samples. They are sorted by production energy. Nuclides produced above 1 MeV are marked in red.

Radionuclides	Energy range of production (MeV)	$\dfrac{\Delta a_i^{sim,geotar}}{a_i^{sim}}$	$\dfrac{\Delta a_i^{sim,phase}}{a_i^{sim}}$	$\left[\dfrac{\Delta a_{i,low}^{sim,con}}{a_i^{sim}}, \dfrac{\Delta a_{i,high}^{sim,con}}{a_i^{sim}}\right]$
^{63}Ni-St	$[10^{-8}; 8 \times 10^{-7}]$			[-0.63 ;0.17]
^{51}Cr-St	$[10^{-8};10^{-6}]$			[-0.63 ;0.17]
^{51}Cr-Al	$[10^{-8};10^{-6}]$			[-0.63 ;0.17]
^{32}P-St	$[10^{-8};10^{-6}]$			[-0.62 ;0.17]
^{55}Fe-St	$[10^{-8} ; 5 \times 10^{-6}]$			[-0.59 ;0.16]
^{55}Fe-Al	$[10^{-8} ; 5 \times 10^{-6}]$			[-0.61 ;0.17]
^{59}Fe-St	$[10^{-8};10^{-5}]$	<0.05	<0.05	[-0.58 ;0.16]
^{59}Fe-Al	$[10^{-8};10^{-5}]$			[-0.59 ;0.16]
^{110m}Ag-Cu	$[10^{-8}; 6 \times 10^{-5}]$			[-0.36 ;0.08]
^{60}Co-St	$[10^{-8}; 10^{-4}]$			[-0.47 ;0.12]
^{65}Zn-Al	$[10^{-8}; 5 \times 10^{-2}]$			[-0.21 ;0.06]
^{185}W-St	$[4 \times 10^{-8} ;10^{-2}]$			<0.05
^{99}Mo-St	$[10^{-5} ; 5 \times 10^{-2}]$			
^{181}W-St	$[2 \times 10^{-8} ;11]$	-0.12		[-0.26 ; 0.1]
^{63}Ni-Cu	[2;8]	-0.28	-0.16	
^{47}Sc-Al	[2;9]	-0.28	-0.16	
^{54}Mn-St	[3; 9]	-0.28	-0.18	
^{58}Co-St	[3; 9]	-0.27	-0.18	
^{92m}Nb-St	[4;10]	-0.30	-0.18	<0.05
^{60}Co-Cu	[6;11]	-0.32	-0.14	
^{54}Mn-Al	[3.5; 13.5]	-0.24	-0.12	
^{57}Co-St	[10; 14]	-0.39	0.11	

3.1.4 Neutron production by protons in $H_2^{18}O$.

In a recent publication (Bakhtiari et al., 2020), measurement results for the neutron fluence emitted by a $H_2^{18}O$ target were compared with the simulation calculations as a function of the sacttering angle and energy of the neutrons. All simulation calculations showed significant differences compared to the measured ones. Already in our first publication we discussed this as an possible reason for the difference between the measured and simulated activities inside the magnet coils of our cyclotron.

The conditions of the experiment were similar to our setup: the energy of the proton beam was 18 MeV, the entrance window made from Havar® had a thickness of 10 μm, the diameter of the target cell was 1.6 cm and its lenght 6 mm (Hagiwara et al., 2011). This experiment measured the neutron fluence at energies between 1.75 MeV and 18 MeV. No data points are available below 1.75 MeV, most likely due to acceptance limitations of this experiment.

In Figure 15, we compare the fluence of neutrons as generated in our simulation by FLUKA (see also Figure 10) with the measurement results of that experiment. As already stated by (Bakhtiari et al., 2020), also our double differential neutron spectra from FLUKA shows important differences when compared to the experimental data. In addition, FLUKA delivers production yields for neutrons below 1.75 MeV, as expected by the phase space from the contributing reaction channels.

As a working hypothesis, we assume that the double differential yield of neutrons by (Hagiwara et al., 2011) reflects the real production cross section of neutrons inside the target for energies above 1.75 MeV. Further, we assume that the energy dependent neutron fluence below 1.75 MeV is well described by FLUKA, when renormalized to the neutron yields of (Hagiwara et al., 2011) at 1.75 MeV. Like this, we try to combine both energies. We have to admit that especially the second assumption is a bit speculative. The main purpose of this exercise is to estimate the impact of (Hagiwara et al., 2011) on the activation of the samples in comparison with FLUKA. The combined curves, (Hagiwara et al., 2011) at energies above 1.75 MeV and rescaled FLUKA yields below, are illustrated also in Figure 15 and are labelled with 'H2O-18'. We implemented an event generator in FLUKA (also called 'H2O-18'), which produces neutrons inside the target with this phase space distribution. For simplicity reasons, the neutron emission is binned into six angular intervals. Within each of these bins, $dN/d\Omega$ is constant. The angles and intervals that have been used are given in Table 17.
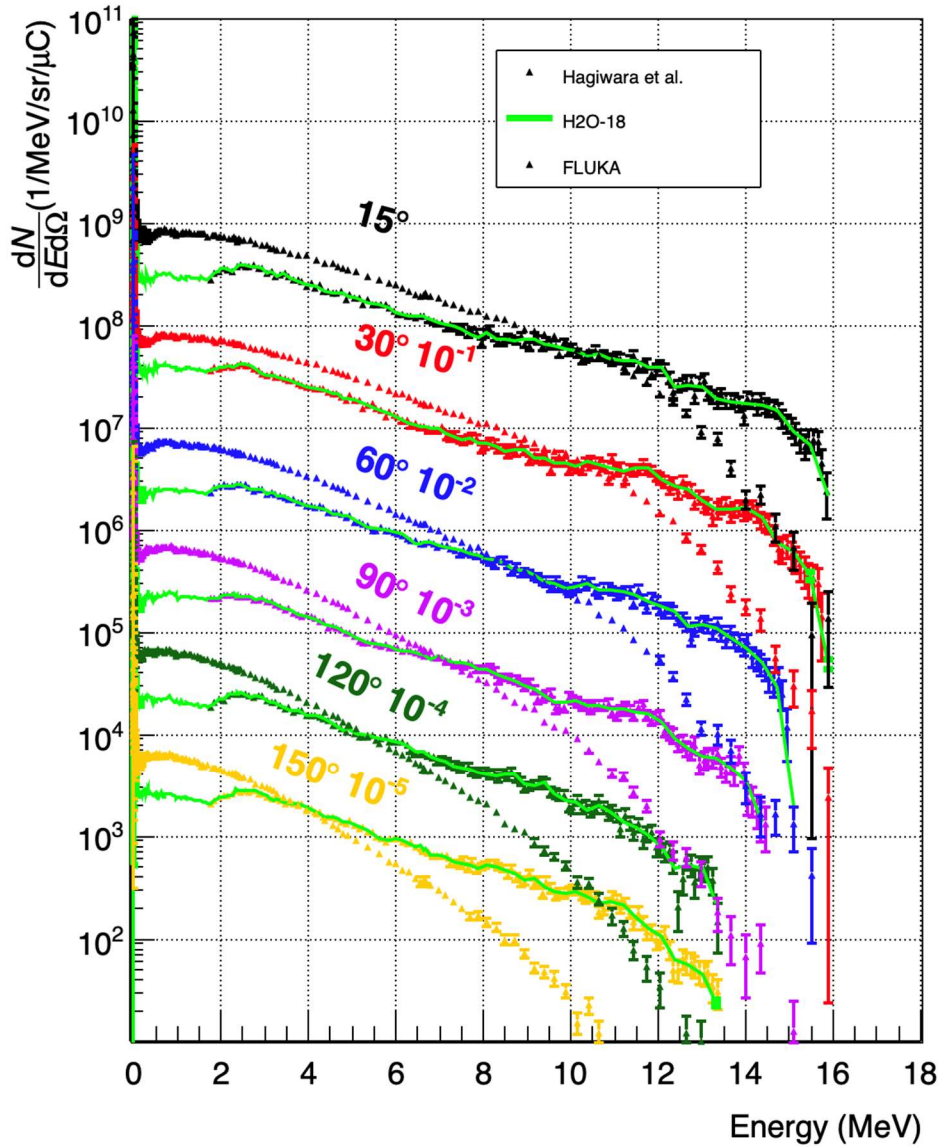
Figure 15. Double differential neutron fluence emitted by the $H_2^{18}O$ target as function of energy and emission angle in the laboratory frame.

Table 17. Azimuth angles and intervals as used in Figure 15.

Hagiwara et al. (°)	Interval FLUKA (°)	Interval 'H20-18' (°)
15	15 ± 3	0-22.5
30	30 ± 3	22.5-45
60	60 ± 3	45-75
90	90 ± 3	75-105
120	120 ± 3	105-135
150	150 ± 3	135-180

We calculated the activities a_i^{H20-1} of the nuclides 'i' inside the samples at the position MM by replacing the proton beam of the simulation with the neutron generator. The ratio:

$$f_i^{H2O-18} = a_i^{sim}/a_i^{H20-18}$$

for each radionuclide is summarized in Table 18. The values vary between 0.4 and 1.8, depending on the energy range of the production. In the next chapter, we will compare the

76

measured activities with both simulations. This may give some indication, if one of the two models is favorable.

Table 18. Ratio f^{H2O-18} for the different radionuclides.

Radionuclides	Energy range of production (MeV)	f^{H2O-18}
^{63}Ni-St	$[10^{-8}; 8 \times 10^{-7}]$	1.8
^{51}Cr-St	$[10^{-8};10^{-6}]$	1.8
^{51}Cr-Al	$[10^{-8};10^{-6}]$	1.8
^{32}P-St	$[10^{-8};10^{-6}]$	1.8
^{55}Fe-St	$[10^{-8} ; 5 \times 10^{-6}]$	1.7
^{55}Fe-Al	$[10^{-8} ; 5 \times 10^{-6}]$	1.7
^{59}Fe-St	$[10^{-8};10^{-5}]$	1.8
^{59}Fe-Al	$[10^{-8};10^{-5}]$	1.8
^{110m}Ag-Cu	$[10^{-8}; 6 \times 10^{-5}]$	1.8
^{60}Co-St	$[10^{-8}; 10^{-4}]$	1.8
^{65}Zn-Al	$[10^{-8}; 5 \times 10^{-2}]$	1.8
^{185}W-St	$[4 \times 10^{-8} ;10^{-2}]$	1.9
^{99}Mo-St	$[10^{-5} ; 5 \times 10^{-2}]$	1.8
^{181}W-St	$[2 \times 10^{-8} ;11]$	1.3
^{63}Ni-Cu	$[2;8]$	1.5
^{47}Sc-Al	$[2;9]$	1.4
^{54}Mn-St	$[3; 9]$	1.4
^{58}Co-St	$[3; 9]$	1.5
^{92m}Nb-St	$[4;10]$	1.4
^{60}Co-Cu	$[6;11]$	1.1
^{57}Co-St	$[10; 14]$	0.4
^{54}Mn-Al	$[3.5; 13.5]$	0.7

3.1.5 Comparison between measurements and simulation

For a more precise comparison between the measurement and the simulation results, we corrected the activities a_i^{sim} by the values of $\Delta a_i^{sim,geotar}$ and $\Delta a_i^{sim,phase}$ from Table 16:

$$a_i^{sim,cor} = a_i^{sim} + \Delta a_i^{sim,geotar} + \Delta a_i^{sim,phase}$$

The uncertainties $\Delta a_i^{sim,cor}$ were calculated using the different contributions listed in Table 12-14 and Table 16 by:

$$\Delta a_i^{sim,cor}\binom{+}{-} = \begin{pmatrix} \Delta a_{i,high}^{sim,con} + a_i^{sim,cor} \sqrt{\left(\frac{\Delta a_i^{sim,geotar}}{a_i^{sim}}\right)^2 + \left(\frac{\Delta a_i^{sim,phase}}{a_i^{sim}}\right)^2 + \left(\frac{\Delta a_i^{sim,chem}}{a_i^{sim}}\right)^2 + \left(\frac{\Delta a_i^{sim,stats}}{a_i^{sim}}\right)^2} \\ \Delta a_{i,low}^{sim,con} - a_i^{sim,cor} \sqrt{\left(\frac{\Delta a_i^{sim,geotar}}{a_i^{sim}}\right)^2 + \left(\frac{\Delta a_i^{sim,phase}}{a_i^{sim}}\right)^2 + \left(\frac{\Delta a_i^{sim,chem}}{a_i^{sim}}\right)^2 + \left(\frac{\Delta a_i^{sim,stats}}{a_i^{sim}}\right)^2} \end{pmatrix}$$

The ratios $r_i = a_i^{meas}/a_i^{sim,cor}$ for all nuclides 'i' of the three materials are shown in Figure 16. In order to avoid ambiguities, we added to the name of the nuclides the first two letters of the material, where it was produced (e.g. "Co-60_St" for ^{60}Co produced in steel). The uncertainties of the ratios were obtained by the simple propagation of the uncertainties of $\Delta a_i^{sim,cor}$ and Δa_i^{meas}.

We also added to this comparison the results of a sample from the magnet coils. The sample was taken from the hotspot of the coils next to T1. Its activation originated mainly from neutrons emitted from that target (Bonvin et al., 2020). In contrast to the samples at MM, which were irradiated at zero degrees in respect to the beam, the copper sample of the coil was situated in the backward hemisphere at an angle around 115 degrees. It is therefore complementary and of interest. Since both simulations (MM and the magnet coils) were done with the same model (only the irradiation profiles were different) all data points should give a consistent picture. The results for the magnet coils are given in Table 19. The corresponding ratios from the coils were also added to Figure 16. They are marked in red.

Table 19. Activities of a copper sample in the backward hemisphere of T1. The statistical uncertainties were below 2 % for the two simulations.

Copper	Energy range of production (MeV)	a_i^{meas}	a_i^{sim}	a_i^{H2O-18}	f_i^{H2O-18}
^{60}Co-coil	[6;11]	106 ± 21	41	81	0.5
^{63}Ni-coil	[2;8]	169 ± 34	163	130	1.3

The ratios of all nuclides of the samples from MM are below one except for ^{57}Co from the stainless steel sample. Here, the ratio was around two. The simulation overestimates significantly the specific activities for all nuclides except for ^{57}Co. The activity of ^{60}Co from the coil at 115 degree was underestimated by a factor 2.5 while the ratio between measured and simulated activity for ^{63}Ni was around one.
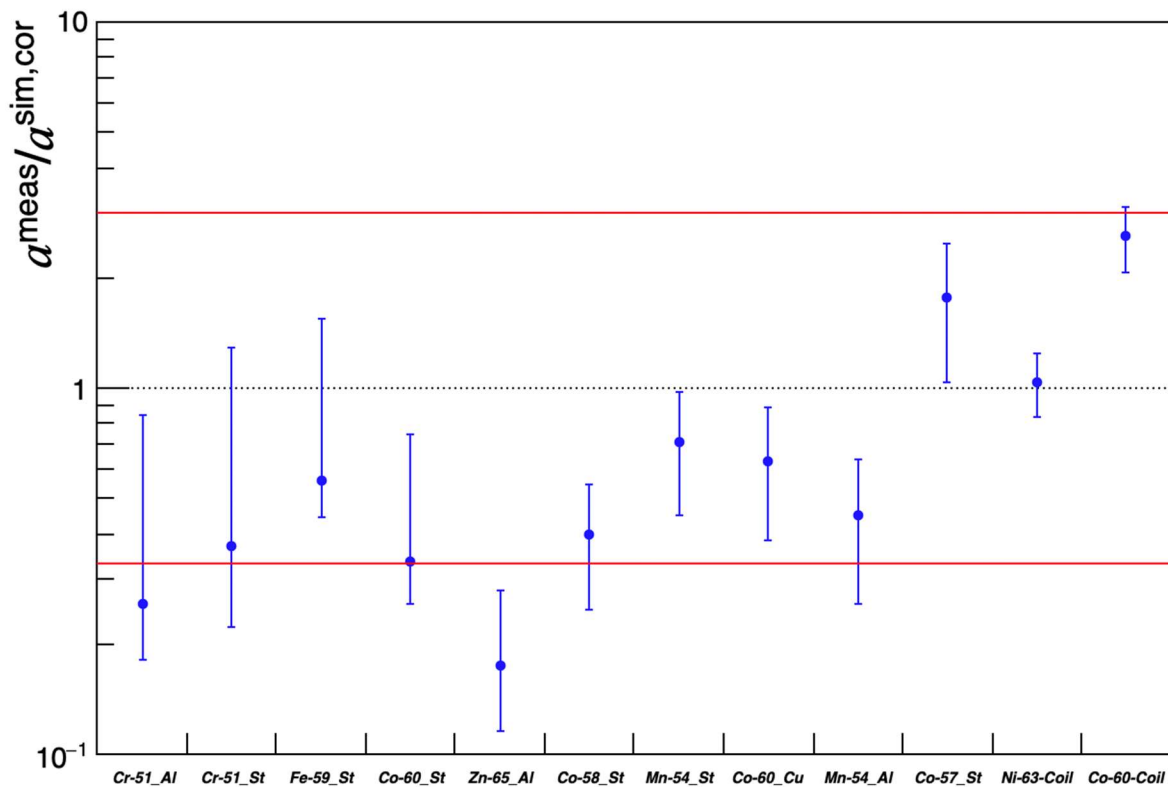
Figure 16. Ratios between the measured and calculated activities for the radionuclides of the samples from MM are shown in blue. The red lines refer to a factor of three.

We tried to estimate the uncertainties thoroughly and in detail. They are not negligible. The result in Figure 16 shows nevertheless that deficiencies are still present in our model, which

78

limits the precision of our simulation calculations. The activities of most of the radionuclides are for example systematically overestimated.

As already discussed before, the simulated fluence of neutrons emitted by the target differs significantly from the measurement results published by (Hagiwara et al., 2011). That is why we implemented the event generator H20-18 based on this publication. Figure 17 shows the ratios a_i^{meas}/a_i^{H20-} using this generator. Most of the data points improve as can be clearly seen by the distribution of the ratios shown in Figure 18.

We do not want to claim, that the precision of our study is sufficient to proof that one or the other approach is right. Our data is in favor of a phase space distribution of the emitted neutrons similar to that one of Hagiwara. Therefore, we would consider this result as a possible uncertainty when we calculate the activities with our FLUKA model.
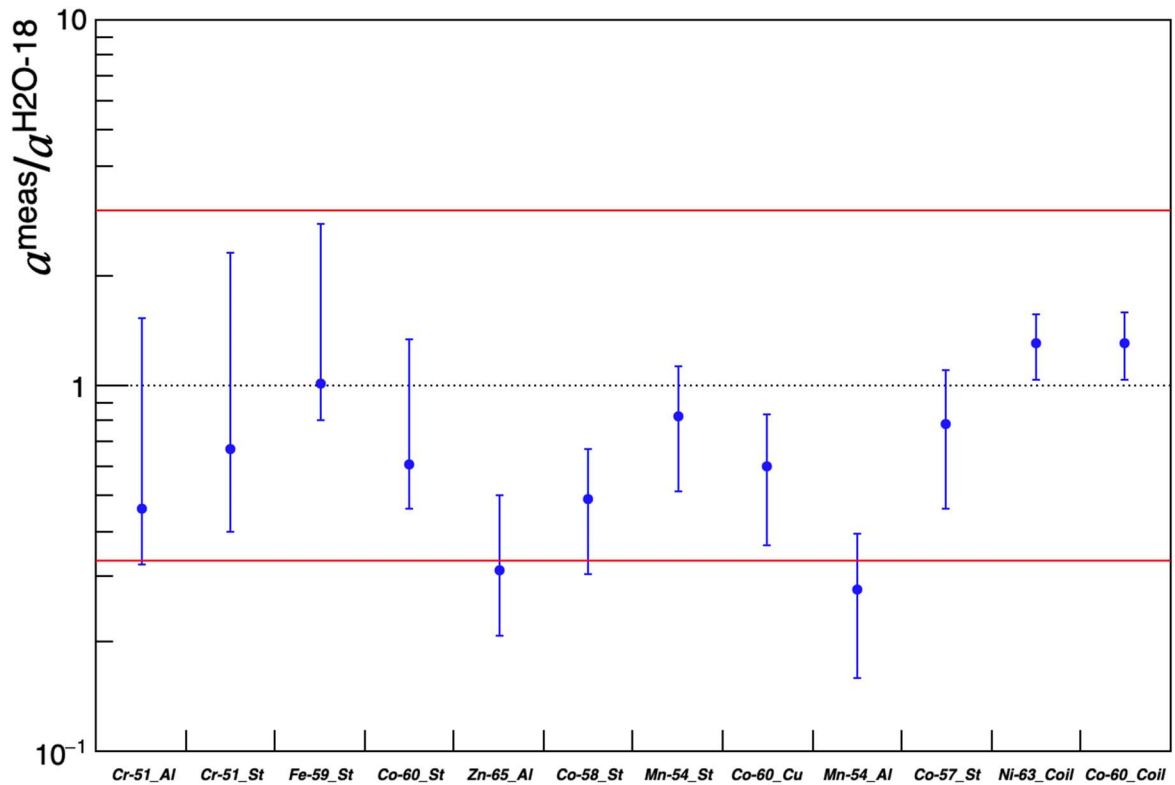
Figure 17. Ratio between the measured and calculated activities. The event generator H2O-18 was used for the simulation. The red lines refer to a factor of three.
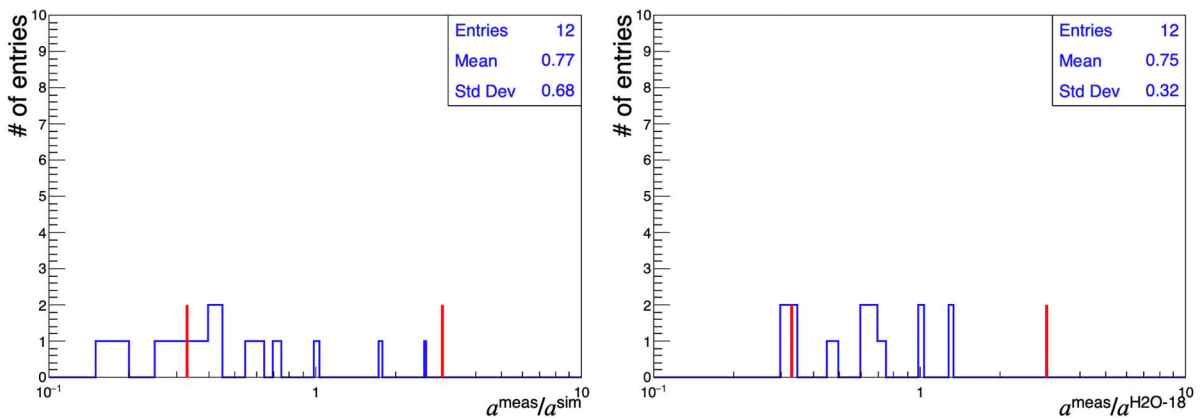
Figure 18. Distribution of the ratios. Left side: a_i^{meas}/a_i^{sim}. Right side: a_i^{meas}/a_i^{H20-18}.

79

The main intention of the campaign C1 was to identify the reasons for systematic uncertainties.

In the following, we want to extend our studies to the realistic operations of the cyclotron over longer periods and to other locations inside the bunker. We will limit our studies to the original FLUKA model without modifications and corrections considering uncertainties in a conservative, empirical way.

3.2 Comparison between measurements and simulation for campaign C2.

The second campaign C2 represents an irradiation scenario over almost one year of daily operation. Four targets (T1, T2, T5 and T7) have been operated during this period for the production of different radionuclides. The irradiation profiles of these targets have been shown already in Figure 8. The characteristics of the different target types as sources of neutrons have been discussed in our article about the activation of the coils of the same cyclotron (Bonvin et al., 2020).
The samples were distributed randomly over the full area of the bunker as shown in Figure 5. The activation of the samples results from the secondary neutrons, which originate either from these four targets or from beam losses inside the machine. All sources of neutrons are taken into account for the calculation of activities as already described in section 2.2.

The simulation and measurement results of these samples are listed in Appendix A, Table S1 to S6. In general, less nuclides have been detected in comparison to the samples from MM. First, the samples of campaign C2 had a weight of 10 grams only, which reduces the minimum detectable activity significantly. Second, the irradiation fields at the locations of the samples of campaign C2 are less intense. It has been validated, that the simulated activity is below the detection limit for cases, where no activity has been detected. Figure 19 shows the ratios a_i^{meas}/a_i^{sim} for the campaign C2 together with those for the campaign C1. Only the uncertainties Δa_i^{che}, $\Delta a_i^{sim,stats}$ and Δa_i^{meas} have been taken into account here. The nuclides are ordered by their production energy. As can been seen, the ratios of the two campaigns are quite similar, even though the locations of the samples are different. From this, one can suppose that systematic effects as discussed for MM affect the irradiation fields at other locations in a similar way. A qualitative study has shown that the thermal neutrons of a target spread widely over the full area of the bunker. That means for example that uncertainties of the target T1, which is the strongest source of neutrons, are observed for nuclides, which are produced at thermal energies, all over the place. High energetic neutrons act more locally. The related activities are highest for samples next to the target and decrease rapidly with increasing distance of the samples from the target port (see also the next section).
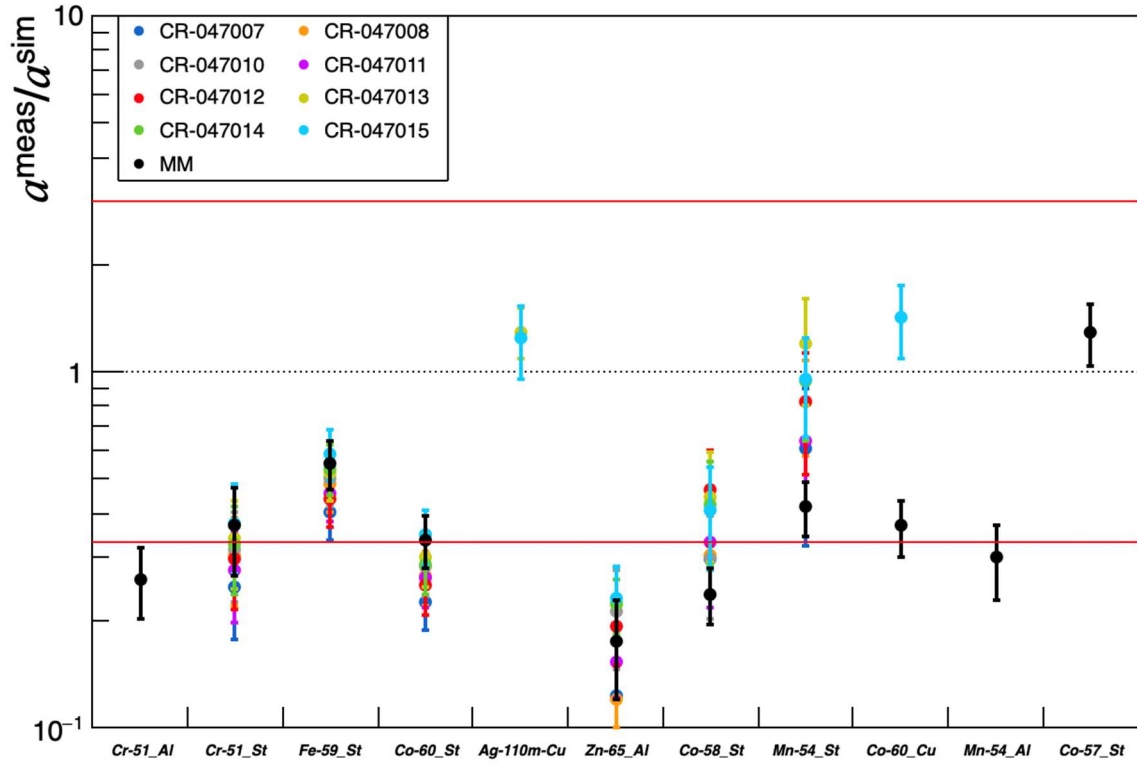
Figure 19. Ratio between the measured and calculated activities as function of the radionuclides for samples during the first campaign.

The average ratios and their standard deviations are summarized for the different reaction channels in Table 20 ordered by their production energy from low to high. Radionuclides produced at energies below 10 keV are marked in yellow. Here, the activities were overestimated by the simulation for all locations by factor two to five, except for ^{110m}Ag in copper where the ratio is around one. It is remarkable that the variation of these ratios by the different locations of the samples are small compared to the mean ratios.
Radionuclides produced at energies above 1 MeV are marked in blue. Here, the activities were again overestimated by the simulation for all locations up to a factor 2.7, except for ^{57}Co in stainless steel where the ratio is around 1.5. ^{57}Co is produced above 10 MeV at the highest energies.

In order to estimate the uncertainties of our simulation independent from the location of irradiation and the energy range of the reaction channels, we plotted the distribution of the ratios a_i^{meas}/a_i^{sim} for all locations and reaction channels in Figure 20. The lowest value comes from ^{65}Zn from the aluminum 6082 samples. The highest comes from ^{57}Co from stainless steel 304L samples. By choosing an interval $\Delta a_i^{sim}/a_i^{sim} \in [0.1, 2]$ for the uncertainties of the simulated activities, we assure that all values of the simulation agree within uncertainties with the measurements. This uncertainty interval (it covers one order of magnitude) is large. However, a simulation result with such an uncertainty is still able to give conclusive results for the characterization of waste, as we will see in the next chapter.

Table 20. Mean ratio a_i^{sim}/a_i^{meas} and standard deviation of the mean ratio as function of the radionuclides.

Radionuclide	Production interval [MeV]	Number of samples	Mean ratio a_i^{meas}/a_i^{sim}	Standard deviation of the ratios
^{51}Cr-St	$[10^{-8};10^{-6}]$	9	0.32	0.040
^{51}Cr-Al	$[10^{-8};10^{-6}]$	1	0.26	-
^{59}Fe-St	$[10^{-8};10^{-5}]$	9	0.50	0.055
^{110m}Ag-Cu	$[10^{-8}; 6 \times 10^{-5}]$	2	1.27	0.030
^{60}Co-St	$[10^{-8}; 10^{-4}]$	9	0.28	0.037
^{65}Zn-Al	$[10^{-8}; 5 \times 10^{-2}]$	9	0.18	0.041
^{54}Mn-St	$[3; 9]$	8	0.80	0.229
^{58}Co-St	$[3; 9]$	9	0.36	0.075
^{54}Mn-Al	$[3.5; 13.5]$	1	0.30	-
^{60}Co-Cu	$[6;11]$	2	0.89	0.527
^{57}Co-St	$[10; 14]$	1	1.29	-
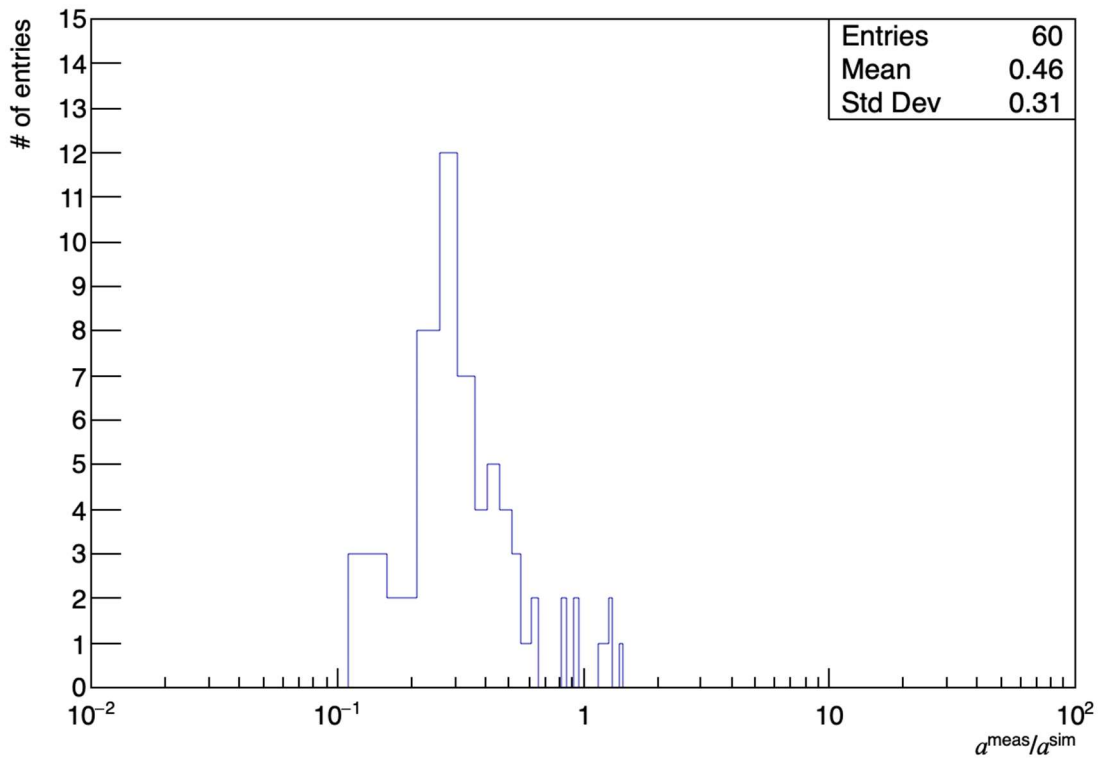
Figure 20. Distribution of a_{meas}/a_{sim} for all the samples and radionuclides for the two campaigns.

4 Characterization of materials along the bunker walls

After we have tested and discussed the uncertainties of our simulation model, we want to estimate systematically the activation of materials along the walls of the cyclotron. In order to determine the spatial distribution, 66 scoring volumes were distributed around the cyclotron as already shown in Figure 5. More details about these volumes can be found in Appendix A, Table S7.

In each of these volumes, the differential neutron fluence was scored with FLUKA. The activities of the radionuclides were then calculated with ActiWiz and RAW. As an example, we will discuss here the results for aluminum, copper and stainless steel after ten years of operation of the cyclotron. We assumed a material composition as described in the Table 6, Table 7 and Table 8. The irradiation profiles were reconstructed from operational data of the cyclotron. An example is shown in Figure 21 for the target T1. The target T2, T4, T5, T6 and T7 have been used during that period as well. The corresponding number of protons hitting these targets during the last ten years are given in the Table 21.
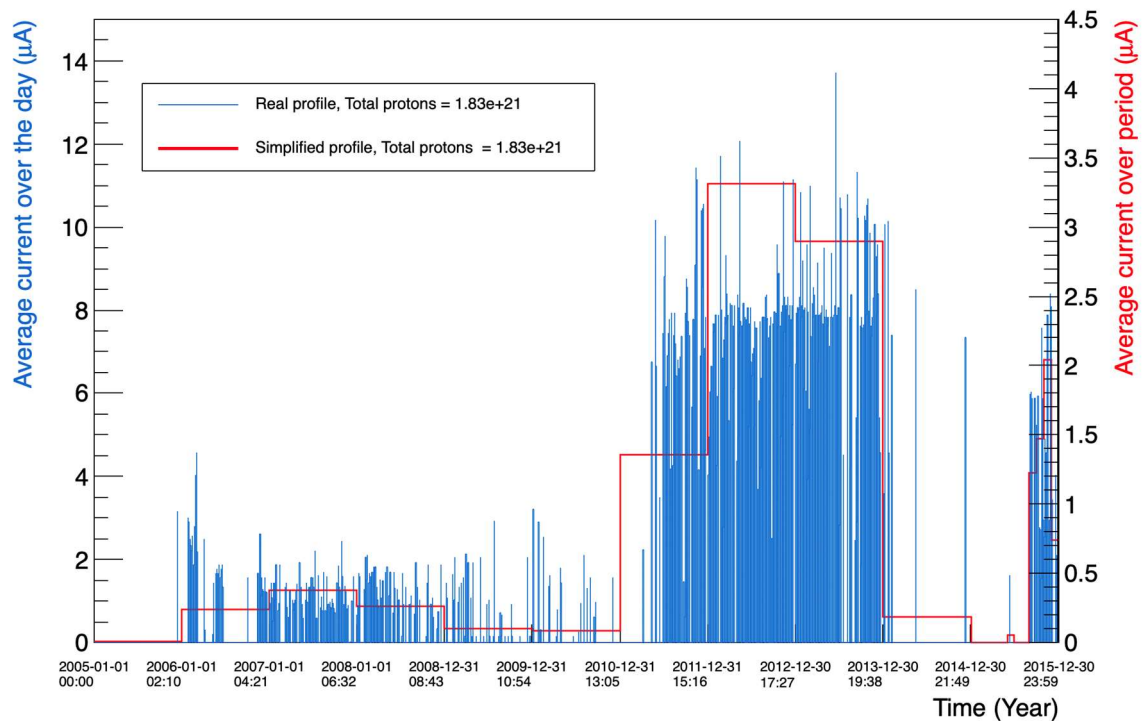
Figure 21. Beam currents on the target T1 during the last 10 years. Blue: mean current per day. Red: Simplified profile.

Table 21 Number of protons for the different sources during the last ten years.

Source	Total protons
T1	1.8×10^{21}
T2	8.3×10^{20}
T3	0
T4	8.1×10^{19}
T5	9.8×10^{19}
T6	8.0×10^{20}
T7	1.2×10^{20}
T8	0
BL	3.8×10^{21}

The spatial distributions of the activities produced in copper are shown in Figure 22 for cooling times of one day and 30 years. The activities of the nuclides were normalized to their clearance limits from Table 12-14. The equivalent plots for stainless steel and aluminum can be found in Appendix A, Figure S1 and S2.

For short cooling times of copper, the nuclides ^{64}Cu, ^{60}Co, ^{110m}Ag and ^{63}Ni were observed. After 30 years, only ^{60}Co and ^{63}Ni survived with significant activities. ^{64}Cu and ^{110m}Ag show a flat distribution. The distributions of ^{60}Co and ^{63}Ni are quite strongly modulated with a variation of activity of about two orders of magnitude. ^{60}Co and ^{63}Ni are produced in copper by neutrons with energies above one MeV. Such energies are mainly found in front of the target ports. In contrast, ^{64}Cu and ^{110m}Ag are produced by neutrons at low energies, which disperse towards the bunker. The variation of the activities here is much smaller and stays within a factor of five.

The spatial distribution of radionuclides depends mainly on the energies of the neutrons, which trigger the corresponding reactions. This is nicely demonstrated also by Figure 23 for a cooling time of one day. Here, the spatial distributions of the activities of radionuclides produced by low-energy neutrons are plotted separately from those produced by high-energy neutrons for all three materials simultaneously.

After 30 years, the situation becomes comparable simple with ^{60}Co and ^{63}Ni being the only radionuclides with relevant activities in respect to the radiological characterization as shown in Figure 24.
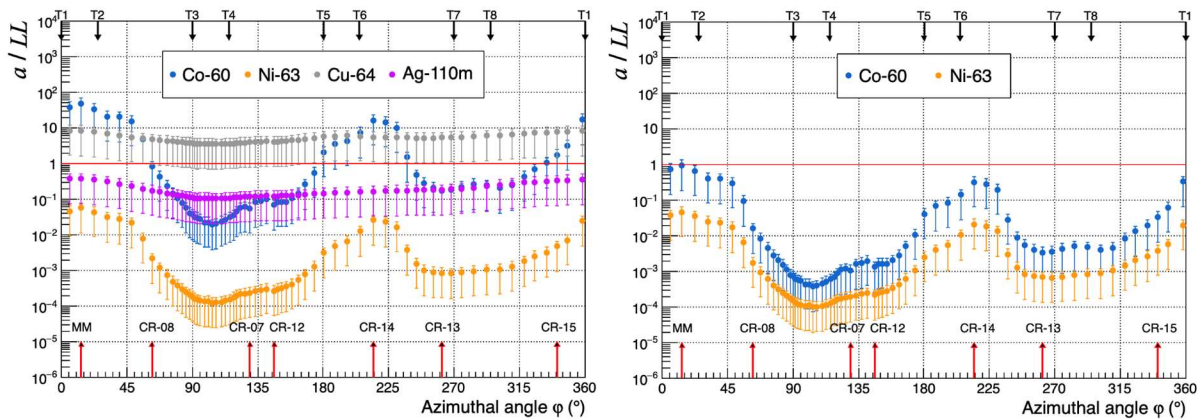
Figure 22 Spatial distribution of the activities in copper. Left: after one day of cooling. Right: after 30 years of cooling.
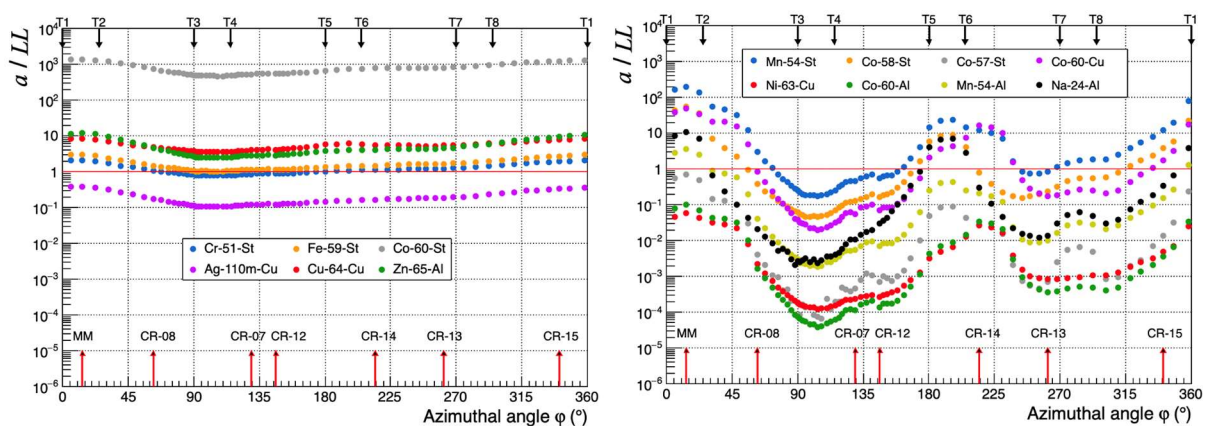
Figure 23 Spatial distribution of the radionuclides of the different reaction channels after one day of cooling. Radionuclides produced by neutrons at low energies (left) and by high energies (right) are shown separately. The error bars have been removed for clarity reasons.
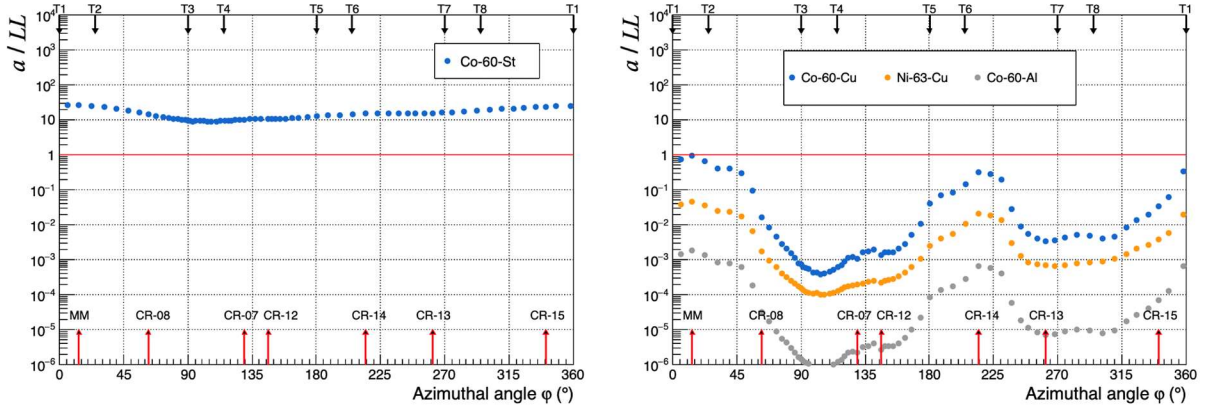
Figure 24 Spatial distribution of the radionuclides of the different reaction channels after 30 years of cooling. Radionuclides produced by neutrons at low energies (left) and by high energies (right) are shown separately. The error bars have been removed for clarity reasons.

In order to determine the hazardousness of the materials after ten years of irradiation, we applied the summation rule (The swiss federal council, 2019) for all scoring volumes and materials:

$$S_{LL,i} = \sum_{l=1}^{m} \frac{a_{l,i}}{LL_l} \tag{10}$$

Here, $a_{l,i}$ denotes the specific activity and $LL_{l,i}$ denotes the clearance limits for each radionuclide l at the locations i.

The spatial distributions of S_{LL} for the stainless steel, aluminum and copper samples are summarized in Figure 25. After one day of cooling all materials are radioactive. After 30 years of cooling, stainless steel is still radioactive all over the bunker. Copper stays radioactive close to the most used targets. On the contrary, aluminum is non-radioactive in all places along the wall of the bunker. The nuclides, which are necessary to explain 90% of S_{LL} at all locations around the walls for the two cooling times are summarized in Table 22.
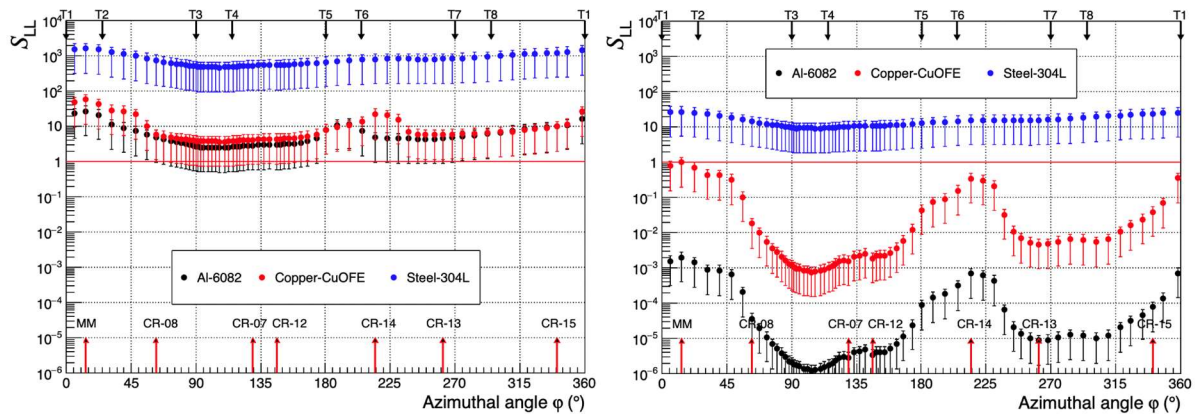
Figure 25 Spatial distribution of S_{LL} for the copper aluminum and stainless steel samples. Left: after one day of cooling. Right: after 30 years of cooling

Table 22. Nuclides, which are necessary to explain at least 90 % of S for the different materials after a cooling time of one day and 30 years.

	1 day	30 years
Stainless steel (304L)	^{60}Co, ^{54}Mn	^{60}Co
Aluminum (6082)	^{65}Zn, ^{54}Mn, ^{24}Na	-
Copper (CuOFE)	^{64}Cu, ^{60}Co, ^{110m}Ag	^{60}Co, ^{63}Ni

5 Conclusion

We applied our simulation model, which is based on FLUKA, ActiWiz and RAW for the radiological characterization of materials inside the bunker of the cyclotron. The same model has been applied successfully already for the characterization of the magnet coils of the same biomedical cyclotron by determining the three-dimensional distribution of activities of all relevant activation products. There were no modifications on the model except the irradiation profiles (beam currents on target), which were adjusted to the new irradiation periods. We tested our simulation by comparing the results to two measurement campaigns with material samples inside the bunker of the cyclotron.

During a first campaign, a copper, stainless steel and aluminum sample were irradiated for one week just next to the bunker wall in front of the target T1, which is used to produce ^{18}F. This target is the strongest source of secondary neutrons of the cyclotron. This irradiation scenario corresponds to a simple one, since only one target was operated during that week. The materials samples were analyzed by gamma spectrometry. The activities of the identified radionuclides were then compared to the corresponding simulation results. The activities of all radionuclides were overestimated by the simulation except for ^{57}Co. The ratios between the activities (measurement/simulation) varied over an order of magnitude between 0.1 and 2. The analysis of the systematic uncertainties of our model gave some first ideas on its shortcomings:

- The geometrical modelling of the target was simplified. Some material of the cooling system was not taken into account.
- The chemical composition and the density of the concrete of the wall takes influence on the flux of thermal neutrons.
- The phase state inside the cell is a mix between liquid and vapor and difficult to model.
- The FLUKA result for the neutron fluence emitted by $H_2^{18}O$ differs from those from experimental measurements.

While the full model of the cyclotron includes 25 tons of material, a few missing grams at certain locations may have already a visible impact. This should be taken into account when the geometry is designed in FLUKA - something that could be improved in our model.
The kind of concrete used for the bunker walls has a significant impact on the fluence of thermal neutrons. A traceability of such information should be guaranteed during the life cycle of an installation until its removal.
It seems that a part of the proton beam does not interact with $H_2^{18}O$ directly, but with the target body instead. It would be helpful, to have some quantitative results available in literature as references.
Possibly, the phase space distribution of the neutrons emitted by the target is not perfectly described by our Monte Carlo tool as it has been reported by (Bakhtiari et al., 2020). We have implemented an event generator for the neutrons emitted by target T1 based on the experimental results of (Hagiwara et al., 2011). Indeed, the agreement between simulation and

measurement improved. This is not only the case for the samples next to the wall downstream of target T1 at zero degrees relative to the beam. In addition, the sample from the magnetic coil next to T1 improved also significantly (backward hemisphere 115 degrees). Our data is in favor of the event generator. However, the situation needs further clarification. First, the precision of our data suffers from several sources of uncertainties. Second, the extrapolation of the experimental data in a "FLUKA like" way to lower energies below 1.75 MeV was purely speculative.

In the second campaign, four different targets have been operated for almost one year, which corresponds to a more complex and realistic irradiation scenario. Several sample bags were distributed randomly all around the bunker. We found also for these very similar systematic discrepancies between FLUKA and the measurements: the simulation overestimates the specific activity for most of the radionuclides. Although, the irradiation scenario was more complex and the irradiation location were spread, the results agreed nevertheless with a precision similar to the first campaign.

By combining the results from both campaigns, we extracted empirically a confidence interval for the uncertainties of the activities by the simulation independent of the locations and the reaction channels. All ratios between measured and simulated activities were within the interval [0.1, 2]. Although this interval is large, it still allows for meaningful simulation results.

We investigated the spatial distribution of the activation of aluminum, stainless steel, and copper along the walls of the cyclotron at the height of the beam for an irradiation period of ten years. At the end of this period all three materials would be radioactive at all these locations in terms of $S_{LL} > 1$. About ten radionuclides have to be taken into account for the radiological characterization of these materials.

The spatial distribution of the activity of a radionuclide depends strongly on the energy range of the neutrons, which dominates its production. Activities produced at low energies have quite small variations all over the bunker. Radionuclides produced by neutrons above 1 MeV are mainly seen in front of the target ports. Their activities vary by at least two orders of magnitudes.

After 30 years of cooling, the picture simplifies considerably. ^{60}Co and ^{63}Ni are the only two radionuclides, which are still of radiological relevance. Stainless steel would be still radioactive at all locations along the walls with ^{60}Co, the only relevant nuclide, produced here at low energies.

Copper exceeds the clearance limits only in front of the target ports for ^{18}F production. ^{60}Co and ^{63}Ni are produced in copper at energies larger 1 MeV. Their activities drop off quite rapidly with increasing distance.

Aluminum (Al-6082) is non-radioactive at all locations along the walls after 30 years of cooling.

Although the uncertainties of the simulation are quite significant, clear conclusions can be drawn nevertheless for the radiological characterization of materials inside the bunker. In cases, where results are not conclusive, the simulations should ideally be complemented by direct measurements with material samples.

Acknowledgements

Reference

Bakhtiari, M., Mokhtari Oranj, L., Jung, N.-S., Lee, A., Lee, H.-S., 2020. Estimation of neutron production yields from H218O as the 18F-production target bombarded by 18-MeV protons. Radiation Physics and Chemistry 177, 109120. https://doi.org/10.1016/j.radphyschem.2020.109120

Böhlen, T.T., Cerutti, F., Chin, M.P.W., Fassò, A., Ferrari, A., Ortega, P.G., Mairani, A., Sala, P.R., Smirnov, G., Vlachoudis, V., 2014. The FLUKA Code: Developments and Challenges for High Energy and Medical Applications. Nuclear Data Sheets 120, 211–214. https://doi.org/10.1016/j.nds.2014.07.049

Bonvin, V., Bochud, F., Damet, J., Geyer, R., Theis, C., Vincke, H., 2020. Detailed study of the distribution of activation inside the magnet coils of a compact PET cyclotron. Applied Radiation and Isotopes 109446. https://doi.org/10.1016/j.apradiso.2020.109446

Braccini, S., 2016. COMPACT MEDICAL CYCLOTRONS AND THEIR USE FOR RADIOISOTOPE PRODUCTION AND MULTI-DISCIPLINARY RESEARCH, in: Proceedings of Cyclotron2016. Zurich, Switzerland, p. 232.

Devillet, F., Geets, J.-M., Ghyoot, M., Kral, E., Michaux, O., Nactergal, B., Nuttens, V., 2013. PERFORMANCE OF IBA NEW CONICAL SHAPED NIOBIUM [18O] WATER TARGETS. Presented at the Proceedings of Cyclotrons2013, Vancouver, BC, Canada.

Eurostat, 2019. Healthcare resource statistics - technical ressources and medical technology. Statistics Explained.

Ferrari, A., Sala, P.R., Fasso, A., Ranft, J., 2005. FLUKA: A Multi-Particle Transport Code (No. SLAC-R-773, 877507). https://doi.org/10.2172/877507

Geyer, R., Damet, J., Theis, C., Vincke, H., Sotiropoulou, M., Bonvin, V., 2019. Radiological characterization of activated material at accelerators. Presented at the IRPA 2018, The Hague, Netherlands, pp. 6–13.

Hagiwara, M., Sanami, T., Masumoto, K., Iwamoto, Y., Matsuda, N., Sakamoto, Y., Nakane, Y., Nakashima, H., Uwamino, Y., 2011. Spectrum Measurement of Neutrons and Gamma-Rays from Thick H182O Target Bombarded with 18 MeV Protons. J. Korean Phy. Soc. 59, 2035–2038. https://doi.org/10.3938/jkps.59.2035

IAEA, 2019. Cyclotrons used for Radionuclide Production [WWW Document]. URL https://nucleus.iaea.org/sites/accelerators/Pages/Cyclotron.aspx#InplviewHashd5afe56 6-18ad-4ac0-8aeb-ccf833dbc282= (accessed 1.31.20).

IAEA, 2018. Charged-particle cross section database for medical radioisotopes production [WWW Document]. URL https://www-nds.iaea.org/medical/positron_emitters.html (accessed 1.31.20).

IBA, 2009. Decommissioning of an IBA Cyclone® 18 PET cyclotron facility.

Leporis, M., Rajec, P., Reich, M., Stefecka, M., Szollos, O., Kovac, P., n.d. 18F- saturation yield in Large Volume cylindrical IBA target.

Papash, A.I., Alenitsky, Yu.G., 2008. On beam intensity upgrade in the commercial cyclotrons of negative hydrogen ions. Phys. Part. Nuclei Lett. 5, 469–472. https://doi.org/10.1134/S1547477108050117

Stokely, M.H., Peeples, J.L., Poorman, M.C., Magerl, M., Siemer, T., Brisard, P., Wieland, B.W., 2012. 150 μA 18F− target and beam port upgrade for the IBA 18/9 cyclotron. Presented at the 14TH INTERNATIONAL WORKSHOP ON TARGETRY AND TARGET CHEMISTRY, Playa del Carmen, Maxico, pp. 71–75. https://doi.org/10.1063/1.4773943

The swiss federal council, 2019. ORaP (Ordonance sur la radioprotection).

Vincke, H., Theis, C., 2018. ActiWiz 3 – an overview of the latest developments and their application. J. Phys.: Conf. Ser. 1046, 012007. https://doi.org/10.1088/1742-6596/1046/1/012007

William, R.G., Gesh, C.J., Pagh, R.T., 2006. Compendium of Material Composition Data for Radiation Transport Modeling.

Yilmaz, J., n.d. Targets.

Appendix A. Supplementary data

This document presents the supplementary material to: "Activation studies within the bunker of a biomedical cyclotron" (Applied Radiation and Isotopes) by V. Bonvin, F. Bochud, J. Damet, C. Theis, H. Vincke and R. Geyer.

Spectrometry results for campaign C2

The following tables present the spectrometry results of the campaign C2 for the aluminum, copper and stainless steel samples.

Table S1. Spectrometry results for the stainless steel (SS-304L) samples of campaign C2.

	CR-047007		CR-047008		CR-047010	
Radionuclide	a_i^{meas} (Bq/g)	$\Delta a_i^{meas}/a_i^{meas}$ (%)	a_i^{meas} (Bq/g)	$\Delta a_i^{meas}/a_i^{meas}$ (%)	a_i^{meas} (Bq/g)	$\Delta a_i^{meas}/a_i^{meas}$ (%)
^{57}Co	$< 2.1 \times 10^{-2}$	/	$< 2.8 \times 10^{-2}$	/	$< 2.6 \times 10^{-2}$	/
^{58}Co	9.0×10^{-2}	13	4.7×10^{-1}	7	1.1×10^{-1}	14
^{60}Co	2.3	13	3.8	13	4	13
^{51}Cr	2.7×10^{1}	18	4.9×10^{1}	18	4.6×10^{1}	18
^{59}Fe	7.0×10^{-1}	14	1.2	14	1.1	14
^{54}Mn	2.8×10^{-2}	38	1.8×10^{-1}	13	$< 5.0 \times 10^{-2}$	/
^{99}Mo	$< 3.4 \times 10^{-1}$	/	$< 4.1 \times 10^{-1}$	/	$< 4.2 \times 10^{-1}$	/
^{187}W	$< 1.2 \times 10^{-1}$	/	$< 1.5 \times 10^{-1}$	/	$< 1.5 \times 10^{-1}$	/
	CR-047011		CR-047012		CR-047013	
Radionuclide	a_i^{meas} (Bq/g)	$\Delta a_i^{meas}/a_i^{meas}$ (%)	a_i^{meas} (Bq/g)	$\Delta a_i^{meas}/a_i^{meas}$ (%)	a_i^{meas} (Bq/g)	$\Delta a_i^{meas}/a_i^{meas}$ (%)
^{57}Co	$< 2.6 \times 10^{-2}$	/	$< 2.4 \times 10^{-2}$	/	$< 2.8 \times 10^{-2}$	/
^{58}Co	2.3×10^{-1}	18	1.7×10^{-1}	10	2.1×10^{-1}	19
^{60}Co	3.8	13	2.7	13	4.6	13
^{51}Cr	4.1×10^{1}	18	3.8×10^{1}	18	5.6×10^{1}	18
^{59}Fe	1.0	14	8.5×10^{-1}	14	1.3	14
^{54}Mn	6.6×10^{-2}	18	4.10×10^{-2}	25	8.7×10^{-2}	18
^{99}Mo	$< 4.1 \times 10^{-1}$	/	$< 3.5 \times 10^{-1}$	/	$< 4.3 \times 10^{-1}$	/
^{187}W	$< 1.4 \times 10^{-1}$	/	$< 1.3 \times 10^{-1}$	/	$< 1.4 \times 10^{-1}$	/
	CR-047014		CR-047015			
Radionuclide	a_i^{meas} (Bq/g)	$\Delta a_i^{meas}/a_i^{meas}$ (%)	a_i^{meas} (Bq/g)	$\Delta a_i^{meas}/a_i^{meas}$ (%)		
^{57}Co	$< 2.8 \times 10^{-2}$	/	$< 3.8 \times 10^{-2}$	/		
^{58}Co	7.90×10^{-1}	16	1.8	16		
^{60}Co	3.9	13	8.3	13		
^{51}Cr	4.60×10^{1}	18	9.0×10^{1}	18		
^{59}Fe	1.2	14	2.2	13		
^{54}Mn	2.5×10^{-1}	18	7.2×10^{-1}	16		
^{99}Mo	$< 4.2 \times 10^{-1}$	/	$< 5.6 \times 10^{-1}$	/		
^{187}W	$< 1.4 \times 10^{-1}$	/	$< 2.0 \times 10^{-1}$	/		

Table S2. Spectrometry results for the aluminum (Al-6082) samples of campaign C2.

	CR-047007		CR-047008		CR-047010	
Radionuclide	a_i^{meas} (Bq/g)	$\Delta a_i^{meas}/a_i^{meas}$ (%)	a_i^{meas} (Bq/g)	$\Delta a_i^{meas}/a_i^{meas}$ (%)	a_i^{meas} (Bq/g)	$\Delta a_i^{meas}/a_i^{meas}$ (%)
^{51}Cr	$< 1.2 \times 10^{-1}$	/	-	/	$< 1.6 \times 10^{-1}$	/
^{54}Mn	$< 2.0 \times 10^{-2}$	/	-	/	$< 2.5 \times 10^{-2}$	/
^{24}Na	$< 1.2 \times 10^{-2}$	/	-	/	$< 1.4 \times 10^{-2}$	/
^{65}Zn	3.0×10^{-2}	37	4.8×10^{-2}	19	8.1×10^{-2}	28

	CR-047011		CR-047012		CR-047013	
Radionuclide	a_i^{meas} (Bq/g)	$\Delta a_i^{meas}/a_i^{meas}$ (%)	a_i^{meas} (Bq/g)	$\Delta a_i^{meas}/a_i^{meas}$ (%)	a_i^{meas} (Bq/g)	$\Delta a_i^{meas}/a_i^{meas}$ (%)
^{51}Cr	$< 1.5 \times 10^{-1}$	/	$< 8.3 \times 10^{-2}$	/	$< 1.4 \times 10^{-1}$	/
^{54}Mn	$< 2.4 \times 10^{-2}$	/	$< 1.4 \times 10^{-2}$	/	$< 2.4 \times 10^{-2}$	/
^{24}Na	$< 1.5 \times 10^{-2}$	/	$< 9.4 \times 10^{-3}$	/	$< 9.6 \times 10^{-3}$	/
^{65}Zn	6.5×10^{-2}	16	5.0×10^{-2}	18	8.7×10^{-2}	12

	CR-047014		CR-047015			
Radionuclide	a_i^{meas} (Bq/g)	$\Delta a_i^{meas}/a_i^{meas}$ (%)	a_i^{meas} (Bq/g)	$\Delta a_i^{meas}/a_i^{meas}$ (%)		
^{51}Cr	$< 1.5 \times 10^{-1}$	/	$< 1.5 \times 10^{-1}$	/		
^{54}Mn	$< 2.4 \times 10^{-2}$	/	$< 2.6 \times 10^{-2}$	/		
^{24}Na	$< 1.5 \times 10^{-2}$	/	$< 2.0 \times 10^{-2}$	/		
^{65}Zn	8.2×10^{-2}	13	1.6×10^{-1}	19		

Table S3. Spectrometry results for the copper (CuOFE) samples of campaign C2.

	CR-047007		CR-047008		CR-047010	
Radionuclide	a_i^{meas} (Bq/g)	$\Delta a_i^{meas}/a_i^{meas}$ (%)	a_i^{meas} (Bq/g)	$\Delta a_i^{meas}/a_i^{meas}$ (%)	a_i^{meas} (Bq/g)	$\Delta a_i^{meas}/a_i^{meas}$ (%)
^{110m}Ag	$< 1.1 \times 10^{-2}$	/	$< 3.9 \times 10^{-2}$	/	$< 3.7 \times 10^{-2}$	/
^{60}Co	$< 7.2 \times 10^{-3}$	/	$< 2.6 \times 10^{-2}$	/	$< 2.5 \times 10^{-2}$	/
^{64}Cu	< 1.2	/	< 5.2	/	< 4.6	/

	CR-047011		CR-047012		CR-047013	
Radionuclide	a_i^{meas} (Bq/g)	$\Delta a_i^{meas}/a_i^{meas}$ (%)	a_i^{meas} (Bq/g)	$\Delta a_i^{meas}/a_i^{meas}$ (%)	a_i^{meas} (Bq/g)	$\Delta a_i^{meas}/a_i^{meas}$ (%)
^{110m}Ag	$< 3.8 \times 10^{-2}$	/	$< 1.1 \times 10^{-2}$	/	2.0×10^{-2}	11
^{60}Co	$< 2.5 \times 10^{-2}$	/	$< 7.3 \times 10^{-3}$	/	$< 7.4 \times 10^{-3}$	/
^{64}Cu	< 4.5	/	1.4	25	< 1.2	/

	CR-047014		CR-047015			
Radionuclide	a_i^{meas} (Bq/g)	$\Delta a_i^{meas}/a_i^{meas}$ (%)	a_i^{meas} (Bq/g)	$\Delta a_i^{meas}/a_i^{meas}$ (%)		
^{110m}Ag	$< 3.7 \times 10^{-2}$	/	3.0×10^{-2}	19		
^{60}Co	$< 2.7 \times 10^{-2}$	/	3.5×10^{-2}	18		
^{64}Cu	< 4.6	/	9.3×10^{-1}	38		

Simulation results for campaign C2

The following tables present the simulation results of the campaign C2 for the aluminum, copper and stainless steel samples.

Table S4. Simulation results for the stainless steel (SS-304L) samples of campaign C2.

CR-047007				CR-047008			
Radionuclide	a_i^{sim} (Bq.g⁻¹)	$\dfrac{\Delta a_i^{sim,stat}}{\Delta a_i}$	$\dfrac{\Delta a_i^{sim,chem}}{\Delta a_i}$	Radionuclide	a_i^{sim} (Bq.g⁻¹)	$\dfrac{\Delta a_i^{sim,stat}}{\Delta a_i}$	$\dfrac{\Delta a_i^{sim,chem}}{\Delta a_i}$
Cr-51	109.8	0.02	0.21	Cr-51	162.5	0.02	0.21
Fe-55	15.2	0.02	0.07	Fe-55	20.2	0.02	0.07
Co-60	10.3	0.02	0.1	Co-60	14.3	0.02	0.1
Fe-59	1.73	0.02	0.07	Fe-59	2.5	0.02	0.07
Ni-63	0.41	0.02	0.11	Co-58	1.5	0.03	0.11
P-32	0.38	0.02	0.36	Mo-99	0.74	0.03	0.11
Co-58	0.30	0.08	0.11	W-187	0.72	0.04	0.1
W-185	0.27	0.02	0.1	Tc-99m	0.72	0.03	0.11
Mo-99	0.093	0.04	0.11	P-32	0.65	0.02	0.36
Tc-99m	0.090	0.04	0.11	Ni-63	0.54	0.02	0.11
Mn-54	0.045	0.09	0.07	W-185	0.49	0.02	0.1
W-187	0.014	0.04	0.1	Mn-54	0.22	0.04	0.07
W-181	0.011	0.02	0.1	W-181	0.016	0.02	0.1
Ni-59	0.0031	0.02	0.11	Co-57	0.0063	0.27	0.11
Co-57	0.00018	0.70	0.11	Ni-59	0.0041	0.02	0.11

CR-047010				CR-047011			
Radionuclide	a_i^{sim} (Bq.g⁻¹)	$\dfrac{\Delta a_i^{sim,chem}}{\Delta a_i}$	$\dfrac{\Delta a_i^{sim,stat}}{\Delta a_i}$	Radionuclide	$\dfrac{\Delta a_i^{sim,chem}}{\Delta a_i}$	$\dfrac{\Delta a_i^{sim,stat}}{\Delta a_i}$	a_i^{sim} (Bq.g⁻¹)
Cr-51	147.3	0.02	0.21	Cr-51	148.1	0.02	0.21
Fe-55	19.5	0.02	0.07	Fe-55	19.6	0.02	0.07
Co-60	14.2	0.02	0.1	Co-60	14.4	0.02	0.1
Fe-59	2.3	0.02	0.07	Fe-59	2.3	0.02	0.07
P-32	0.56	0.02	0.36	Co-58	0.69	0.06	0.11
Ni-63	0.53	0.02	0.11	P-32	0.57	0.02	0.36
W-185	0.48	0.02	0.1	Mo-99	0.57	0.02	0.11
Mo-99	0.43	0.03	0.11	Tc-99m	0.55	0.02	0.11
Tc-99m	0.42	0.03	0.11	W-185	0.55	0.02	0.1
Co-58	0.37	0.07	0.11	Ni-63	0.53	0.02	0.11
W-187	0.18	0.03	0.1	W-187	0.20	0.03	0.1
Mn-54	0.052	0.09	0.07	Mn-54	0.10	0.08	0.07
W-181	0.016	0.02	0.1	W-181	0.017	0.02	0.1
Ni-59	0.0040	0.02	0.11	Ni-59	0.0040	0.02	0.11

CR-047012				CR-047013			
Radionuclide	a_i^{sim} (Bq.g⁻¹)	$\dfrac{\Delta a_i^{sim,stat}}{\Delta a_i}$	$\dfrac{\Delta a_i^{sim,chem}}{\Delta a_i}$	Radionuclide	a_i^{sim} (Bq.g⁻¹)	$\dfrac{\Delta a_i^{sim,stat}}{\Delta a_i}$	$\dfrac{\Delta a_i^{sim,chem}}{\Delta a_i}$
Cr-51	126.9	0.03	0.21	Cr-51	164.2	0.02	0.21
Fe-55	15.8	0.03	0.07	Fe-55	21.7	0.02	0.07
Co-60	10.7	0.03	0.1	Co-60	15.3	0.02	0.1
Fe-59	1.9	0.03	0.07	Fe-59	2.5	0.02	0.07
P-32	0.48	0.03	0.36	P-32	0.63	0.02	0.36
Ni-63	0.43	0.03	0.11	Ni-63	0.59	0.02	0.11
Co-58	0.36	0.07	0.11	Co-58	0.43	0.08	0.11
W-185	0.29	0.03	0.1	W-185	0.45	0.02	0.1
Mo-99	0.25	0.04	0.11	Mo-99	0.42	0.03	0.11
Tc-99m	0.25	0.04	0.11	Tc-99m	0.41	0.03	0.11
W-187	0.21	0.04	0.1	W-187	0.20	0.03	0.1
Mn-54	0.050	0.08	0.07	Mn-54	0.072	0.10	0.07
W-181	0.012	0.02	0.1	W-181	0.017	0.02	0.1
Ni-59	0.0032	0.03	0.11	Ni-59	0.0045	0.02	0.11
Co-57	0.00018	0.50	0.11	Co-57	0.00062	0.35	0.11

CR-047014				CR-047015			
Radionuclide	a_i^{sim} (Bq.g⁻¹)	$\dfrac{\Delta a_i^{sim,stat}}{\Delta a_i}$	$\dfrac{\Delta a_i^{sim,chem}}{\Delta a_i}$	Radionuclide	a_i^{sim} (Bq.g⁻¹)	$\dfrac{\Delta a_i^{sim,stat}}{\Delta a_i}$	$\dfrac{\Delta a_i^{sim,chem}}{\Delta a_i}$
Cr-51	139.8	0.02	0.21	Cr-51	240.2	0.02	0.21
Fe-55	19.5	0.02	0.07	Fe-55	32.4	0.02	0.07
Co-60	13.8	0.02	0.1	Co-60	23.9	0.01	0.1
Fe-59	2.2	0.02	0.07	Co-58	4.4	0.03	0.11
Co-58	1.9	0.03	0.11	Fe-59	3.7	0.02	0.07

Radionuclide	a_i^{sim}	$\dfrac{\Delta a_i^{sim,stat}}{\Delta a_i}$	$\dfrac{\Delta a_i^{sim,chem}}{\Delta a_i}$	Radionuclide	a_i^{sim}	$\dfrac{\Delta a_i^{sim,stat}}{\Delta a_i}$	$\dfrac{\Delta a_i^{sim,chem}}{\Delta a_i}$
Ni-63	0.52	0.02	0.11	Mo-99	1.4	0.02	0.11
P-32	0.47	0.02	0.36	Tc-99m	1.3	0.02	0.11
W-185	0.46	0.02	0.1	P-32	0.99	0.02	0.36
Mn-54	0.27	0.04	0.07	W-185	0.87	0.02	0.1
Mo-99	0.15	0.03	0.11	Ni-63	0.87	0.02	0.11
Tc-99m	0.14	0.03	0.11	Mn-54	0.76	0.03	0.07
W-187	0.018	0.03	0.1	W-187	0.74	0.02	0.1
W-181	0.016	0.01	0.1	W-181	0.028	0.01	0.1
Ni-59	0.0040	0.02	0.11	Ni-59	0.0066	0.02	0.11
Co-57	0.0040	0.27	0.11	Co-57	0.0050	0.50	0.11
				Nb-92m	0.0016	0.04	0.11
				Co-58m	0.0012	0.03	0.11

Table S5. Simulation results for the aluminum (Al-6082) samples of campaign C2.

CR-047007				CR-047008			
Radionuclide	a_i^{sim} (Bq.g⁻¹)	$\dfrac{\Delta a_i^{sim,stat}}{\Delta a_i}$	$\dfrac{\Delta a_i^{sim,chem}}{\Delta a_i}$	Radionuclide	a_i^{sim} (Bq.g⁻¹)	$\dfrac{\Delta a_i^{sim,stat}}{\Delta a_i}$	$\dfrac{\Delta a_i^{sim,chem}}{\Delta a_i}$
Cr-51	2.0	0.02	0.11	Cr-51	3.0	0.02	0.11
Zn-65	0.25	0.02	0.12	Zn-65	0.40	0.02	0.12
Fe-55	0.19	0.02	0.29	Fe-55	0.25	0.02	0.29
Fe-59	0.022	0.02	0.29	Cu-64	0.045	0.03	0.1
Mn-54	0.00058	0.09	0.17	Fe-59	0.031	0.02	0.29
				Na-24	0.0064	0.30	0.2
				Mn-54	0.0034	0.06	0.17
CR-047010				**CR-047011**			
Radionuclide	a_i^{sim} (Bq.g⁻¹)	$\dfrac{\Delta a_i^{sim,stat}}{\Delta a_i}$	$\dfrac{\Delta a_i^{sim,chem}}{\Delta a_i}$	Radionuclide	a_i^{sim} (Bq.g⁻¹)	$\dfrac{\Delta a_i^{sim,stat}}{\Delta a_i}$	$\dfrac{\Delta a_i^{sim,chem}}{\Delta a_i}$
Cr-51	2.7	0.02	0.11	Cr-51	2.7	0.02	0.11
Zn-65	0.38	0.02	0.12	Zn-65	0.43	0.02	0.12
Fe-55	0.24	0.02	0.29	Fe-55	0.24	0.02	0.29
Fe-59	0.028	0.02	0.29	Fe-59	0.029	0.02	0.29
Cu-64	0.0033	0.03	0.1	Cu-64	0.0034	0.02	0.1
Mn-54	0.00065	0.09	0.17	Mn-54	0.0013	0.08	0.17
CR-047012				**CR-047013**			
Radionuclide	a_i^{sim} (Bq.g⁻¹)	$\dfrac{\Delta a_i^{sim,stat}}{\Delta a_i}$	$\dfrac{\Delta a_i^{sim,chem}}{\Delta a_i}$	Radionuclide	a_i^{sim} (Bq.g⁻¹)	$\dfrac{\Delta a_i^{sim,stat}}{\Delta a_i}$	$\dfrac{\Delta a_i^{sim,chem}}{\Delta a_i}$
Cr-51	2.4	0.03	0.11	Cr-51	3.0	0.02	0.11
Zn-65	0.26	0.03	0.12	Zn-65	0.40	0.02	0.12
Fe-55	0.20	0.03	0.29	Fe-55	0.27	0.02	0.29
Cu-64	0.032	0.04	0.1	Fe-59	0.031	0.02	0.29
Fe-59	0.024	0.03	0.29	Cu-64	0.0036	0.03	0.1
Mn-54	0.00063	0.08	0.17	Mn-54	0.00094	0.09	0.17
CR-047014				**CR-047015**			
Radionuclide	a_i^{sim} (Bq.g⁻¹)	$\dfrac{\Delta a_i^{sim,stat}}{\Delta a_i}$	$\dfrac{\Delta a_i^{sim,chem}}{\Delta a_i}$	Radionuclide	a_i^{sim} (Bq.g⁻¹)	$\dfrac{\Delta a_i^{sim,stat}}{\Delta a_i}$	$\dfrac{\Delta a_i^{sim,chem}}{\Delta a_i}$
Cr-51	2.6	0.02	0.11	Cr-51	4.4	0.02	0.11
Zn-65	0.37	0.02	0.12	Zn-65	0.71	0.01	0.12
Fe-55	0.24	0.02	0.29	Fe-55	0.40	0.02	0.29
Fe-59	0.028	0.02	0.29	Fe-59	0.046	0.02	0.29
Mn-54	0.0036	0.05	0.17	Cu-64	0.023	0.02	0.1
				Na-24	0.012	0.13	0.2
				Mn-54	0.0099	0.04	0.17

Table S6. Simulation results for the copper (CuOFE) samples of campaign C2.

CR-047007				CR-047008			
Radionuclide	a_i^{sim} (Bq.g⁻¹)	$\dfrac{\Delta a_i^{sim,stat}}{\Delta a_i}$	$\dfrac{\Delta a_i^{sim,chem}}{\Delta a_i}$	Radionuclide	a_i^{sim} (Bq.g⁻¹)	$\dfrac{\Delta a_i^{sim,stat}}{\Delta a_i}$	$\dfrac{\Delta a_i^{sim,chem}}{\Delta a_i}$
Cu-64	0.15	0.03	<0.001	Cu-64	150.7	0.03	<0.001
Ag-110m	0.0099	0.02	0.1	Ag-110m	0.015	0.02	0.1
Ni-63	0.0032	0.07	<0.001	Ni-63	0.014	0.03	<0.001
Co-60	0.0012	0.22	<0.001	Co-60	0.0083	0.11	<0.001
CR-047010				**CR-047011**			
Radionuclide	a_i^{sim} (Bq.g⁻¹)	$\dfrac{\Delta a_i^{sim,stat}}{\Delta a_i}$	$\dfrac{\Delta a_i^{sim,chem}}{\Delta a_i}$	Radionuclide	a_i^{sim} (Bq.g⁻¹)	$\dfrac{\Delta a_i^{sim,stat}}{\Delta a_i}$	$\dfrac{\Delta a_i^{sim,chem}}{\Delta a_i}$

Radionuclide	a_i^{sim} (Bq.g^{-1})	$\dfrac{\Delta a_i^{sim,stat}}{\Delta a_i}$	$\dfrac{\Delta a_i^{sim,chem}}{\Delta a_i}$	Radionuclide	a_i^{sim} (Bq.g^{-1})	$\dfrac{\Delta a_i^{sim,stat}}{\Delta a_i}$	$\dfrac{\Delta a_i^{sim,chem}}{\Delta a_i}$
Cu-64	3.0	0.03	<0.001	Cu-64	11.2	0.02	<0.001
Ag-110m	0.015	0.02	0.1	Ag-110m	0.015	0.01	0.1
Ni-63	0.0043	0.07	<0.001	Ni-63	0.0082	0.05	<0.001
Co-60	0.00084	0.27	<0.001	Co-60	0.0013	0.19	<0.001
CR-047012				**CR-047013**			
Radionuclide	a_i^{sim} (Bq.g^{-1})	$\dfrac{\Delta a_i^{sim,stat}}{\Delta a_i}$	$\dfrac{\Delta a_i^{sim,chem}}{\Delta a_i}$	Radionuclide	a_i^{sim} (Bq.g^{-1})	$\dfrac{\Delta a_i^{sim,stat}}{\Delta a_i}$	$\dfrac{\Delta a_i^{sim,chem}}{\Delta a_i}$
Cu-64	29.2	0.04	<0.001	Cu-64	3.3	0.02	<0.001
Ag-110m	0.010	0.02	0.1	Ag-110m	0.015	0.02	0.1
Ni-63	0.0035	0.06	<0.001	Ni-63	0.0056	0.07	<0.001
Co-60	0.0011	0.19	<0.001	Co-60	0.0017	0.21	<0.001
CR-047014				**CR-047015**			
Radionuclide	a_i^{sim} (Bq.g^{-1})	$\dfrac{\Delta a_i^{sim,stat}}{\Delta a_i}$	$\dfrac{\Delta a_i^{sim,chem}}{\Delta a_i}$	Radionuclide	a_i^{sim} (Bq.g^{-1})	$\dfrac{\Delta a_i^{sim,stat}}{\Delta a_i}$	$\dfrac{\Delta a_i^{sim,chem}}{\Delta a_i}$
Cu-64	0.052	0.03	<0.001	Cu-64	20.6	0.02	<0.001
Ni-63	0.016	0.03	<0.001	Ni-63	0.05	0.02	<0.001
Ag-110m	0.014	0.01	0.1	Co-60	0.025	0.09	<0.001
Co-60	0.0098	0.08	<0.001	Ag-110m	0.025	0.01	0.1

Volume names and coordinates used for the characterization

The following table presents the volume names and coordinates used for the characterization. Each volume (filled with air) has the same dimension 30 cm * 30 cm * 10 cm.

Table S7. Volume names and their corresponding φ_{mean} and r_{mean}.

Volume name	φ_{mean}	r_{mean}	Volume name	φ_{mean}	r_{mean}
V1	13.6	195.8	V34	146.4	385.2
V2	5.4	204.7	V35	141.0	404.6
V3	178.0	217.5	V36	137.0	413.8
V4	348.2	235.9	V37	133.2	424.9
V5	340.9	233.9	V38	129.6	437.8
V6	333.6	235.8	V39	126.2	452.3
V7	325.6	217.5	V40	123.1	468.3
V8	318.3	204.7	V41	120.1	485.6
V9	310.1	195.8	V42	118.1	504.1
V10	301.3	191.2	V43	115.6	523.6
V11	292.3	191.2	V44	112.5	544.2
V12	283.6	195.8	V45	110.3	565.5
V13	275.4	204.7	V46	105.9	573.8
V14	268.0	217.5	V47	103.5	555.4
V15	261.5	233.4	V48	101.0	538.0
V16	255.9	251.9	V49	98.2	521.8

V17	249.4	258.5	V50	95.3	506.8
V18	244.1	239.3	V51	93.2	474.7
V19	237.9	222.5	V52	91.7	447.4
V20	230.8	208.6	V53	89.9	420.4
V21	222.9	198.3	V54	87.9	393.9
V22	214.3	192.2	V55	85.7	367.9
V23	205.3	190.7	V56	83.1	342.6
V24	196.4	193.8	V57	80.1	318.1
V25	188.0	201.3	V58	76.6	294.7
V26	180.4	212.9	V59	72.5	272.5
V27	173.6	227.8	V60	67.7	251.9
V28	167.7	245.5	V61	62.1	233.4
V29	162.7	265.4	V62	55.6	217.5
V30	158.4	287.1	V63	48.3	204.7
V31	154.7	310.2	V64	40.1	195.8
V32	151.5	334.4	V65	31.3	191.2
V33	148.8	359.4	V66	22.3	191.2

Results of radiological characterization

The following figures present the results of characterization for the aluminum and stainless steel samples after one day and 30 years of cooling.
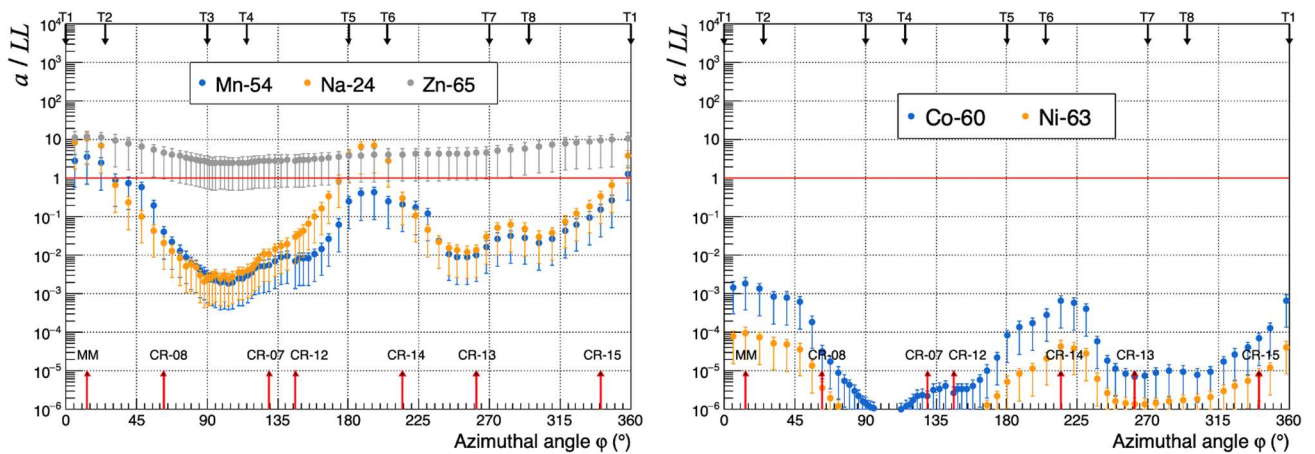

Figure S1. Spatial distribution of the activities in aluminum 6082. Left: after one day of cooling. Right: after 30 years of cooling.
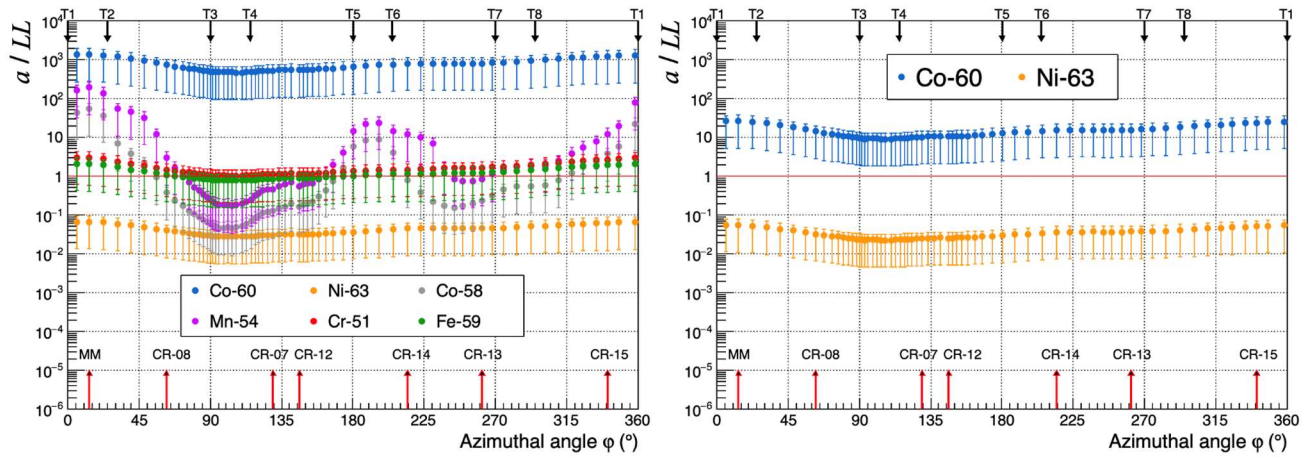
Figure S2. Spatial distribution of the activities in stainless steel 304L. Left: after one day of cooling. Right: after 30 years of cooling.